



Non–commutativity in Hayward spacetime

N. Heidari  *

*Center for Theoretical Physics, Khazar University,
41 Mehseti Street, Baku, AZ-1096, Azerbaijan. and
School of Physics, Damghan University, Damghan, 3671641167, Iran.*

A. A. Araújo Filho  †

*Departamento de Física, Universidade Federal da Paraíba,
Caixa Postal 5008, 58051-970, João Pessoa, Paraíba, Brazil*

Iarley P. Lobo  ‡

*Department of Chemistry and Physics, Federal University of Paraíba,
Rodovia BR 079 - km 12, 58397-000 Areia-PB, Brazil*

Abstract

In this work, we propose a new black hole solution, namely, a Hayward-like metric incorporating corrections due to non-commutativity. We begin by deriving this solution using the non-commutative gauge theory framework. The general properties of the metric are then analyzed, including the event horizon structure and the Kretschmann scalar. Analogous to the standard Hayward solution, the modified black hole remains regular, provided that additional conditions must be satisfied, specifically $\theta \in \mathbb{R} \setminus \{\frac{\pi}{2} + n\pi \mid n \in \mathbb{Z}\}$. Next, we examine the thermodynamic properties, computing the Hawking temperature, entropy, and heat capacity. The temperature profile suggests the existence of a remnant mass when $T^{(\Theta, l)} \rightarrow 0$. Quantum radiation is analyzed by considering both bosonic and fermionic particle modes, with an estimation of the particle creation density provided for each case. The effective potential is evaluated perturbatively to accomplish the analysis of quasinormal modes and the time-domain response for scalar perturbations. The study of null geodesics is explored to enable the characterization of the photon sphere and black hole shadows. Additionally, constraints on the shadows are estimated based on EHT (Event Horizon Telescope) data. Furthermore, the Gaussian curvature is determined to assess the stability of critical orbits, followed by an analysis of gravitational lensing using the Gauss-Bonnet theorem. Finally, the constraints (bounds) on the parameters Θ (non-commutativity) and l (“Hayward parameter”) are derived based on solar system tests, including the perihelion precession of Mercury, light deflection, and the Shapiro time delay effect.

*Electronic address: heidari.n@gmail.com

†Electronic address: dilto@fisica.ufc.br (The corresponding author)

‡Electronic address: lobofisica@gmail.com

Contents

I. Introduction	4
II. The new non–commutative black hole	6
III. Thermodynamics	14
A. Hawking temperature	15
B. Entropy	16
C. Heat capacity	17
IV. Quantum radiation	17
A. Bosonic particle modes	18
B. Fermionic particle modes	19
V. The scalar perturbation	24
VI. Quasinormal modes	32
VII. Time–domain solution	34
VIII. Null Geodesics	37
A. Photonic radius and shadows	38
B. Lensing observables by EHT	44
IX. Gravitational lensing	45
A. Stability of the photon sphere	45
B. The weak deflection limit in the Gauss–Bonnet framework	47
X. Estimation of bounds based on the solar system tests	48
A. Perihelion precession of Mercury	50
B. Deflection of light	52
C. Time delay of light	54
XI. Conclusion	56
Acknowledgments	57

I. INTRODUCTION

The formulation of gravity within general relativity inherently involves a geometric description of spacetime, where nonlinear effects make solving the Einstein field equations highly challenging. Even under imposed symmetries or constraints, finding exact solutions remains a difficult task [1, 2]. To overcome these difficulties, a weak-field approximation is frequently applied, transforming the equations into a more manageable form. This method allows for the study of gravitational waves, which arise as perturbations in spacetime. These oscillations play a significant role in black hole physics, influencing their stability, the emission of Hawking radiation, and interactions with their surrounding environment.

The principles of general relativity do not inherently impose a fundamental constraint on the precision of spatial measurements. Nonetheless, various theoretical perspectives propose that a minimal length scale, frequently linked to the Planck length, may serve as a natural limit. To account for this, alternative spacetime models incorporating non-commutative properties have been formulated, drawing inspiration from string theory [3–5]. Such models have also been widely examined within the framework of supersymmetric Yang–Mills theories [6–8]. Within gravitational scenarios, the implementation of non-commutativity is often achieved via the Seiberg–Witten map, which enables modifications to the underlying symmetry structure [9].

The application of non-commutative geometry has played a crucial role in advancing black hole research [10–23]. In particular, studies have focused on its implications for black hole evaporation [24, 25] and modifications to thermodynamic behavior [20, 26–29]. Moreover, the thermal characteristics of field theories have been explored in various contexts [30, 31].

Fundamentally, the idea of non-commutative spacetime arises from modifying the algebra of coordinates, expressed through the commutator relation $[x^\mu, x^\nu] = i\Theta^{\mu\nu}$, where $\Theta^{\mu\nu}$ is an anti-symmetric tensor characterizing non-commutativity. This departure from conventional spacetime geometry has prompted diverse strategies for incorporating such effects into gravitational frameworks. One approach involves altering gauge symmetries by extending the de Sitter group $SO(4,1)$ and merging it with the Poincaré group $ISO(3,1)$ through the Seiberg–Witten map. Within this framework, Chaichian et al. [32] proposed a modified

version of the Schwarzschild metric that integrates non-commutative corrections.

Nicolini et al. [33] proposed a different way to incorporate non-commutativity into general relativity by modifying the matter distribution instead of altering the Einstein tensor. Rather than treating mass as a point-like source, this approach introduces a continuous mass distribution. Two distinct profiles describe this modification: a Gaussian density function, $\rho_{\Theta} = M(4\pi\Theta)^{-\frac{3}{2}}e^{-\frac{r^2}{4\Theta}}$, and a Lorentzian profile, $\rho_{\Theta} = M\sqrt{\Theta}\pi^{-\frac{3}{2}}(r^2 + \pi\Theta)^{-2}$. Furthermore, Ref. [34] recently outlined a general framework for black hole construction in non-commutative gravity, expanding the earlier established methodologies encountered in the literature [32, 35].

The observation of gravitational waves by LIGO and Virgo [36–38] has provided new directions for investigating gravitational effects, including lensing phenomena in the weak-field regime [39, 40]. Earlier studies on gravitational lensing primarily addressed light deflection over vast cosmological scales, frequently employing the Schwarzschild metric as a reference model [41]. Subsequent research broadened this scope to incorporate more general static and spherically symmetric backgrounds [42]. Nevertheless, in regions where gravitational fields are extremely strong, such as near black holes, light deflection becomes more pronounced, requiring refined analytical (or numerical) techniques to describe these deviations accurately.

The successful direct imaging of a supermassive black hole by the Event Horizon Telescope has driven further exploration of gravitational lensing phenomena [43–49]. In earlier studies, Virbhadra and Ellis introduced a simplified lensing equation to examine black holes within asymptotically flat spacetimes [50, 51]. Their analysis showed that intense gravitational fields could generate multiple images, emphasizing the significance of developing accurate theoretical models for these scenarios.

Further theoretical advancements by Frittelli et al. [52], Bozza et al. [53, 54], and Tsukamoto [55] have enhanced the study of gravitational lensing in strong-field regimes. These refinements have been applied across various spacetime configurations, including Schwarzschild black holes [56–75], axisymmetric black holes [76–84], and wormholes [85–90]. Lensing studies have also been extended to modified gravity frameworks [91–93] and charged Reissner–Nordström backgrounds [94–98]. Moreover, investigations into gravitational distortions have examined the influence of extreme fields on light trajectories [99, 100].

Hawking’s contributions established a direct relationship between black hole thermodynamics and quantum field theory [101–103]. His findings indicated that black holes emit

thermal radiation, which gradually depletes their mass — a phenomenon now referred to as Hawking radiation [104–109]. This breakthrough significantly advanced the study of quantum effects in curved spacetime [110–119]. Building on this, Kraus and Wilczek [120], along with Parikh and Wilczek [121–123], later reinterpreted this radiation as a consequence of quantum tunneling. Their semi-classical perspective has since been applied to numerous black hole models, further refining the theoretical understanding of energy emission in strong gravitational fields [124–138].

Furthermore, the gravitational waves offer a fundamental tool to investigate astrophysical and cosmological events, such as binary mergers and stellar oscillations [139–145]. Their spectral features are shaped by the nature of their sources, with perturbed black holes generating gravitational radiation at distinct frequencies, commonly referred to as quasinormal modes [114, 146–164].

In general lines, this work presents a new black hole solution that integrates non-commutative effects within a Hayward-like metric. The analysis encompasses its geometric structure, thermodynamic behavior, quasinormal spectra, and observational features. Model parameters are constrained through solar system tests, considering perihelion precession, light bending, and Shapiro time delay.

II. THE NEW NON-COMMUTATIVE BLACK HOLE

This part establishes the foundational approach for analyzing gravity within a non-commutative gauge theory framework. The gauge group under consideration, as mentioned earlier, corresponds to the de Sitter group, $SO(4, 1)$. To begin, attention is directed toward the construction of the $SO(4, 1)$ gauge theory in a commutative $(3 + 1)$ -dimensional Minkowski spacetime. In this context, the metric, when expressed in spherical coordinates, is given by

$$ds^2 = dr^2 + r^2 d\Omega_2^2 - c^2 dt^2. \quad (1)$$

The angular component of the metric is represented as $d\Omega_2^2 = d\theta^2 + \sin^2 \theta d\varphi^2$. The symmetry group under consideration, $SO(4, 1)$, is generated by a set of ten elements, denoted $\mathfrak{M}_{\mathfrak{A}\mathfrak{B}}$, which adhere to the antisymmetric property $\mathfrak{M}_{\mathfrak{A}\mathfrak{B}} = -\mathfrak{M}_{\mathfrak{B}\mathfrak{A}}$. In addition, the indices $\mathfrak{A}, \mathfrak{B}$ take values in $\{a, 5\}$, where a, b run from 0 to 3. It is worth mentioning that these generators naturally split into two groups: the set $\mathfrak{M}_{ab} = -\mathfrak{M}_{ba}$, which governs rotational

transformations, and the set $\mathfrak{P}_a = \mathfrak{M}_{a5}$, which encodes translational operations.

The gauge potentials in their undeformed configuration, represented by $\tilde{\omega}_\mu^{\mathfrak{A}\mathfrak{B}}(x)$, satisfy the antisymmetric relation $\tilde{\omega}_\mu^{\mathfrak{A}\mathfrak{B}}(x) = -\tilde{\omega}_\mu^{\mathfrak{B}\mathfrak{A}}(x)$. Unlike the spin connection, which adheres to $\tilde{\omega}_\mu^{ab}(x) = -\tilde{\omega}_\mu^{ba}(x)$, and the tetrad fields, denoted as $\mathbf{e}_\mu^a(x)$, these gauge potentials play a distinct role. The components $\hat{\omega}_\mu^{a5}(x)$ establish a connection to the tetrads through the proportionality $\hat{\omega}_\mu^{a5}(x) = \mathfrak{K} \hat{\mathbf{e}}_\mu^a(x)$, where \mathfrak{K} acts as a contraction parameter. Furthermore, an extra gauge field, expressed as $\hat{\omega}_\mu^{55}(x) = \mathfrak{K} \hat{\phi}_\mu(x, \Theta)$, emerges, with the function $\hat{\phi}_\mu(x, \Theta)$ vanishing when $\mathfrak{K} \rightarrow 0$. Taking this limit effectively collapses the gauge structure to that of the Poincaré group, $\text{ISO}(3, 1)$ [14, 18]. The associated field strength tensor for the gauge potential $\omega_\mu^{\mathfrak{A}\mathfrak{B}}(x)$ reads

$$F_\mu^{\mathfrak{A}\mathfrak{B}} = \partial_\mu \omega_\nu^{\mathfrak{A}\mathfrak{B}} - \partial_\nu \omega_\mu^{\mathfrak{A}\mathfrak{B}} + (\tilde{\omega}_\mu^{\mathfrak{A}\mathfrak{C}} \tilde{\omega}_\nu^{\mathfrak{D}\mathfrak{B}} - \tilde{\omega}_\nu^{\mathfrak{A}\mathfrak{C}} \tilde{\omega}_\mu^{\mathfrak{D}\mathfrak{B}}) \mathbf{n}_{\mathfrak{C}\mathfrak{D}}, \quad (2)$$

in which the spacetime indices range over $\mu, \nu = 0, 1, 2, 3$, and the metric tensor is given by $\mathbf{n}_{\mathfrak{A}\mathfrak{B}} = \text{diag}(+, +, +, -, +)$. This formulation can also be rewritten in an equivalent form, leading to an alternative expression

$$F_{\mu\nu}^{a5} = \mathfrak{K} [\partial_\mu \mathbf{e}_\nu^a - \partial_\nu \mathbf{e}_\mu^a + (\tilde{\omega}_\mu^{ab} \mathbf{e}_\nu^a - \tilde{\omega}_\nu^{ab} \mathbf{e}_\mu^a) \mathbf{n}_{bc}] = \mathfrak{K} T_{\mu\nu}^a, \quad (3a)$$

$$F_{\mu\nu}^{ab} = \partial_\mu \tilde{\omega}_\nu^{ab} - \partial_\nu \tilde{\omega}_\mu^{ab} + (\tilde{\omega}_\mu^{ac} \tilde{\omega}_\nu^{db} - \tilde{\omega}_\nu^{ac} \tilde{\omega}_\mu^{db}) \mathbf{n}_{cd} + \mathfrak{K} (\mathbf{e}_\mu^a \mathbf{e}_\nu^b - \mathbf{e}_\nu^a \mathbf{e}_\mu^b) = R_{\mu\nu}^{ab}, \quad (3b)$$

with the metric components are given by $\mathbf{n}_{ab} = \text{diag}(+, +, +, -)$. Notably, the Poincaré gauge group under consideration is directly associated with the geometric framework of Riemann–Cartan spacetime, which accommodates both curvature and torsion effects [14, 165]. The torsion tensor is introduced as $T_{\mu\nu}^a \equiv F_{\mu\nu}^{a5}/\mathfrak{K}$, while the curvature tensor is defined as $R_{\mu\nu}^{ab} \equiv F_{\mu\nu}^{ab}$. Both quantities are formulated in terms of the tetrad fields $\mathbf{e}_\mu^a(x)$ and the spin connection $\tilde{\omega}_\mu^{ab}(x)$. In the particular case where the torsion field vanishes, as expressed in Eq. (3a), the spin connection can entirely be addressed by the tetrad fields alone.

The focus now shifts to examining a possible structure for gauge fields exhibiting spherical symmetry within the framework of the $\text{SO}(4, 1)$ group [14, 165]

$$\mathbf{e}_\mu^1 = \left(\frac{1}{\tilde{\mathcal{A}}}, 0, 0, 0 \right), \quad \mathbf{e}_\mu^2 = (0, r, 0, 0), \quad \mathbf{e}_\mu^3 = (0, 0, r \sin\theta, 0), \quad \mathbf{e}_\mu^0 = \left(0, 0, 0, 0, \tilde{\mathcal{A}} \right), \quad (4)$$

and

$$\begin{aligned} \tilde{\omega}_\mu^{12} &= (0, \tilde{\mathcal{W}}, 0, 0), & \tilde{\omega}_\mu^{13} &= (0, 0, \tilde{\mathcal{Z}} \sin\theta, 0), & \tilde{\omega}_\mu^{10} &= (0, 0, 0, \tilde{\mathcal{U}}), \\ \tilde{\omega}_\mu^{23} &= (0, 0, -\cos\theta, \tilde{\mathcal{V}}), & \tilde{\omega}_\mu^{20} &= \tilde{\omega}_\mu^{30} = (0, 0, 0, 0), \end{aligned} \quad (5)$$

where the quantities $\tilde{\mathcal{A}}$, $\tilde{\mathcal{U}}$, $\tilde{\mathcal{V}}$, $\tilde{\mathcal{W}}$, and $\tilde{\mathcal{Z}}$ are functions that depend only on the radial coordinate in three-dimensional space. In addition, the torsion tensor features nonvanishing components, which can be represented as [18]

$$\begin{aligned} T_{01}^0 &= -\frac{\tilde{\mathcal{A}}\tilde{\mathcal{A}}' + \tilde{\mathcal{U}}}{\mathcal{A}}, & T_{03}^2 &= r \tilde{\mathcal{V}} \sin \theta T_{12}^2 = \frac{\tilde{\mathcal{A}} + \tilde{\mathcal{W}}}{\tilde{\mathcal{A}}}, \\ T_{02}^3 &= -r \tilde{\mathcal{V}}, & T_{13}^3 &= \frac{(\tilde{\mathcal{A}} + \tilde{\mathcal{Z}}) \sin \theta}{\tilde{\mathcal{A}}}. \end{aligned} \quad (6)$$

Consequently, the curvature tensor is expressed as [18]

$$\begin{aligned} R_{01}^{01} &= \tilde{\mathcal{U}}', & R_{01}^{23} &= -\tilde{\mathcal{V}}', & R_{23}^{13} &= (\tilde{\mathcal{Z}} - \tilde{\mathcal{W}}) \cos \theta, & R_{01}^{01} &= -\tilde{\mathcal{U}}\tilde{\mathcal{W}}, & R_{01}^{13} &= -\tilde{\mathcal{V}}\tilde{\mathcal{W}}, \\ R_{03}^{03} &= -\tilde{\mathcal{U}}\tilde{\mathcal{Z}} \sin \theta, & R_{03}^{12} &= \tilde{\mathcal{V}}\tilde{\mathcal{Z}} \sin \theta R_{12}^{12} = \tilde{\mathcal{W}}', & R_{23}^{23} &= (1 - \tilde{\mathcal{Z}}\tilde{\mathcal{W}}) \sin \theta, & R_{13}^{13} &= \tilde{\mathcal{Z}}' \sin \theta. \end{aligned} \quad (7)$$

The notation $\tilde{\mathcal{A}}'$, $\tilde{\mathcal{U}}'$, $\tilde{\mathcal{V}}'$, $\tilde{\mathcal{W}}'$, and $\tilde{\mathcal{Z}}'$ represents derivatives with respect to the radial coordinate. In order to eliminate the torsion field, as specified in Eq. (6), the following constraints must be satisfied

$$\tilde{\mathcal{V}} = 0, \quad \tilde{\mathcal{U}} = -\tilde{\mathcal{A}}\tilde{\mathcal{A}}', \quad \tilde{\mathcal{W}} = -\tilde{\mathcal{A}} = \tilde{\mathcal{Z}}. \quad (8)$$

Here, by considering the corresponding field equation, the following relations must be imposed

$$R_{\mu}^{\alpha} - \frac{1}{2}R \mathbf{e}_{\mu}^{\alpha} = 0, \quad (9)$$

formulated in terms of the tetrad fields $\mathbf{e}_{\mu}^{\alpha}(x)$, with the curvature components defined as $R_{\mu}^{\alpha} = R_{\mu\nu}^{ab} \mathbf{e}_{\nu}^b$ and the scalar curvature given by $R = R_{\mu\nu}^{ab} \mathbf{e}_{\mu}^{\mu} \mathbf{e}_{\nu}^{\nu}$, the obtained solution reads

$$\tilde{\mathcal{A}}(r) = \sqrt{1 - \frac{2Mr^2}{r^3 + 2Ml^2}}. \quad (10)$$

In this context, M denotes the black hole mass, while l corresponds to ‘‘Hayward parameter’’. The formulation of the modified metric, expressed as $ds^2 = \hat{g}_{\mu\nu}^{(\Theta, l)}(x, \Theta) dx^{\mu} dx^{\nu}$, requires working in spherical coordinates, where $x^{\mu} = (t, r, \theta, \varphi)$ defines the coordinate system for a $(3 + 1)$ -dimensional non-commutative Schwarzschild spacetime. To achieve this, the deformed tetrad fields $\hat{\mathbf{e}}_{\mu}^{\alpha}(x, \Theta)$ must be determined. These tetrads emerge through the contraction of the non-commutative gauge group $\text{SO}(4, 1)$ with the Poincaré group $\text{ISO}(3, 1)$, employing the Seiberg–Witten map framework [3, 166, 167]. The nature of the resulting non-commutative spacetime is then characterized by the following conditions:

$$[x^{\mu}, x^{\nu}] = i\Theta^{\mu\nu}. \quad (11)$$

The parameters $\Theta^{\mu\nu}$ are taken to be real and obey the antisymmetry condition $\Theta^{\mu\nu} = -\Theta^{\nu\mu}$. Consequently, the gravitational sector in a non-commutative framework, particularly the deformed tetrad fields $\hat{\mathbf{e}}_\mu^a(x, \Theta)$ and the gauge connection $\hat{\tilde{\omega}}_\mu^{\mathfrak{A}\mathfrak{B}}(x, \Theta)$, can be systematically expanded in terms of the non-commutativity parameter Θ as a power series [3, 14, 18, 166]

$$\begin{aligned}\hat{\mathbf{e}}_\mu^a(x, \Theta) &= \mathbf{e}_\mu^a(x) - i\Theta^{\nu\rho}\mathbf{e}_{\mu\nu\rho}^a(x) + \Theta^{\nu\rho}\Theta^{\lambda\tau}e_{\mu\nu\rho\lambda\tau}^a(x)\dots, \\ \hat{\tilde{\omega}}_\mu^{\mathfrak{A}\mathfrak{B}}(x, \Theta) &= \tilde{\omega}_\mu^{\mathfrak{A}\mathfrak{B}}(x) - i\Theta^{\nu\rho}\tilde{\omega}_{\mu\nu\rho}^{\mathfrak{A}\mathfrak{B}}(x) + \Theta^{\nu\rho}\Theta^{\lambda\tau}\tilde{\omega}_{\mu\nu\rho\lambda\tau}^{\mathfrak{A}\mathfrak{B}}(x)\dots\end{aligned}\quad (12)$$

The deformed tetrad fields $\hat{\mathbf{e}}_\mu^a(x, \Theta)$ emerge as a consequence of introducing non-commutative corrections to the gauge connection $\hat{\tilde{\omega}}_\mu^{\mathfrak{A}\mathfrak{B}}(x, \Theta)$. Their expansion follows from the formulation provided in Eq. (12) truncated to second-order terms in the parameter Θ

$$\omega_{\mu\nu\rho}^{\mathfrak{A}\mathfrak{B}}(x) = \frac{1}{4} \{ \tilde{\omega}_\nu, \partial_\rho \tilde{\omega}_\mu + R_{\rho\mu} \}^{\mathfrak{A}\mathfrak{B}}, \quad (13a)$$

$$\begin{aligned}\tilde{\omega}_{\mu\nu\rho\lambda\tau}^{\mathfrak{A}\mathfrak{B}}(x) &= \frac{1}{32} \left(- \{ \tilde{\omega}_\lambda, \partial_\tau \{ \tilde{\omega}_\nu, \partial_\rho \tilde{\omega}_\mu + R_{\rho\mu} \} \} + 2 \{ \tilde{\omega}_\lambda, \{ R_{\tau\nu}, R_{\mu\rho} \} \} \right. \\ &\quad \left. - \{ \tilde{\omega}_\lambda, \{ \tilde{\omega}_\nu, D_\rho R_{\tau\mu} + \partial_\rho R_{\tau\mu} \} \} - \{ \{ \tilde{\omega}_\nu, \partial_\rho \tilde{\omega}_\lambda + R_{\rho\lambda} \}, (\partial_\tau \tilde{\omega}_\mu + R_{\tau\mu}) \} \right. \\ &\quad \left. + 2 [\partial_\nu \tilde{\omega}_\lambda, \partial_\rho (\partial_\tau \tilde{\omega}_\mu + R_{\tau\mu})] \right)^{\mathfrak{A}\mathfrak{B}}.\end{aligned}\quad (13b)$$

Derived using the Seiberg–Witten map, Eqs. (13a) and (13b) must satisfy

$$[\alpha, \beta]^{\mathfrak{A}\mathfrak{B}} = \alpha^{\mathfrak{A}\mathfrak{C}}\beta_{\mathfrak{C}}^{\mathfrak{B}} - \beta^{\mathfrak{A}\mathfrak{C}}\alpha_{\mathfrak{C}}^{\mathfrak{B}}, \quad \{ \alpha, \beta \}^{\mathfrak{A}\mathfrak{B}} = \alpha^{\mathfrak{A}\mathfrak{C}}\beta_{\mathfrak{C}}^{\mathfrak{B}} + \beta^{\mathfrak{A}\mathfrak{C}}\alpha_{\mathfrak{C}}^{\mathfrak{B}}, \quad (14)$$

and

$$D_\mu R_{\rho\sigma}^{\mathfrak{A}\mathfrak{B}} = \partial_\mu R_{\rho\sigma}^{\mathfrak{A}\mathfrak{B}} + (\tilde{\omega}_\mu^{\mathfrak{A}\mathfrak{C}} R_{\rho\sigma}^{\mathfrak{B}\mathfrak{C}} + \tilde{\omega}_\mu^{\mathfrak{B}\mathfrak{C}} R_{\rho\sigma}^{\mathfrak{A}\mathfrak{C}}) \mathbf{n}_{\mathfrak{C}\mathfrak{D}}. \quad (15)$$

Certain restrictions must be highlighted regarding the gauge connection $\hat{\tilde{\omega}}_\mu^{\mathfrak{A}\mathfrak{B}}(x, \Theta)$, which adhere to the following constraints

$$\hat{\tilde{\omega}}_\mu^{\mathfrak{A}\mathfrak{B}*}(x, \Theta) = -\hat{\tilde{\omega}}_\mu^{\mathfrak{A}\mathfrak{B}}(x, \Theta), \quad \hat{\tilde{\omega}}_\mu^{\mathfrak{A}\mathfrak{B}}(x, \Theta)^r \equiv \hat{\tilde{\omega}}_\mu^{\mathfrak{A}\mathfrak{B}}(x, -\Theta) = -\hat{\tilde{\omega}}_\mu^{\mathfrak{B}\mathfrak{A}}(x, \Theta). \quad (16)$$

It is important to mention that the notation $*$ represents the complex conjugate operation. Furthermore, the non-commutative modifications derived from the conditions imposed in Eq. (16) can be expressed as

$$\tilde{\omega}_\mu^{\mathfrak{A}\mathfrak{B}}(x) = -\tilde{\omega}_\mu^{\mathfrak{B}\mathfrak{A}}(x), \quad \tilde{\omega}_{\mu\nu\rho}^{\mathfrak{A}\mathfrak{B}}(x) = \tilde{\omega}_{\mu\nu\rho}^{\mathfrak{B}\mathfrak{A}}(x), \quad \tilde{\omega}_{\mu\nu\rho\lambda\tau}^{\mathfrak{A}\mathfrak{B}}(x) = -\tilde{\omega}_{\mu\nu\rho\lambda\tau}^{\mathfrak{B}\mathfrak{A}}(x). \quad (17)$$

The above expressions follow from the application of Eqs. (13a) and (13b), considering the constraints of a vanishing torsion field $T_{\mu\nu}^a$ and taking the limit $\mathfrak{K} \rightarrow 0$. Under these conditions, we have

$$\hat{\mathbf{e}}_{\mu}^{a*}(x, \Theta) = \mathbf{e}_{\mu}^a(x) + i\Theta^{\nu\rho}\mathbf{e}_{\mu\nu\rho}^a(x) + \Theta^{\nu\rho}\Theta^{\lambda\tau}\mathbf{e}_{\mu\nu\rho\lambda\tau}^a(x) \dots, \quad (18)$$

where

$$\mathbf{e}_{\mu\nu\rho}^a = \frac{1}{4} [\tilde{\omega}_{\nu}^{ac}\partial_{\rho}\mathbf{e}_{\mu}^d + (\partial_{\rho}\tilde{\omega}_{\mu}^{ac} + R_{\rho\mu}^{ac})\mathbf{e}_{\nu}^d] \mathbf{n}_{ad}, \quad (19)$$

and

$$\begin{aligned} \mathbf{e}_{\mu\nu\rho\lambda\tau}^a(x) = & \frac{1}{32} \left[2\{R_{\tau\nu}, R_{\mu\rho}\}^{ab}\mathbf{e}_{\lambda}^c - \tilde{\omega}_{\lambda}^{ab}(D_{\rho} + \partial_{\rho})R_{\tau\mu}^{cd}\mathbf{e}_{\nu}^m \mathbf{n}_{dm} \right. \\ & - \{\tilde{\omega}_{\nu}, (D_{\rho} + \partial_{\rho})R_{\tau\mu}\}^{ab}\mathbf{e}_{\lambda}^c - \partial_{\tau}\{\tilde{\omega}_{\nu}, (\partial_{\rho}\tilde{\omega}_{\mu} + R_{\rho\mu})\}^{ab}\mathbf{e}_{\lambda}^c \\ & - \tilde{\omega}_{\lambda}^{ab}\partial_{\tau}(\tilde{\omega}_{\nu}^{cd}\partial_{\rho}\mathbf{e}_{\mu}^m + (\partial_{\rho}\tilde{\omega}_{\mu}^{cd} + R_{\rho\mu}^{cd})\mathbf{e}_{\nu}^m) \mathbf{n}_{dm} + 2\partial_{\nu}\tilde{\omega}_{\lambda}^{ab}\partial_{\rho}\partial_{\tau}\mathbf{e}_{\mu}^c \\ & - 2\partial_{\rho}(\partial_{\tau}\tilde{\omega}_{\mu}^{ab} + R_{\tau\mu}^{ab})\partial_{\nu}\mathbf{e}_{\lambda}^c - \{\tilde{\omega}_{\nu}, (\partial_{\rho}\tilde{\omega}_{\lambda} + R_{\rho\lambda})\}^{ab}\partial_{\tau}\mathbf{e}_{\mu}^c \\ & \left. - (\partial_{\tau}\tilde{\omega}_{\mu}^{ab} + R_{\tau\mu}^{ab})(\tilde{\omega}_{\nu}^{cd}\partial_{\rho}\mathbf{e}_{\lambda}^m + (\partial_{\rho}\tilde{\omega}_{\lambda}^{cd} + R_{\rho\lambda}^{cd})\mathbf{e}_{\nu}^m \mathbf{n}_{dm}) \right] \mathbf{n}_{bc}. \end{aligned} \quad (20)$$

As a result, the modified metric tensor takes the form

$$g_{\mu\nu}^{(\Theta)}(x, \Theta) = \frac{1}{2}\mathbf{n}_{ab}(\hat{\mathbf{e}}_{\mu}^a(x, \Theta) * \hat{\mathbf{e}}_{\nu}^{b*}(x, \Theta) + \hat{\mathbf{e}}_{\mu}^b(x, \Theta) * \hat{\mathbf{e}}_{\nu}^{a*}(x, \Theta)), \quad (21)$$

with the symbol $*$ denotes the standard star product. For the subsequent calculations, natural units will be employed, fixing $\hbar = c = G = 1$. Under this convention, the following

expression holds

$$\begin{aligned}
g_{tt}^{(\Theta, l)} &= \frac{2Mr^2}{2l^2M+r^3} - 1 - \frac{1}{4} \left\{ \frac{1}{2} \left(\frac{6Mr^4}{(2l^2M+r^3)^2} - \frac{4Mr}{2l^2M+r^3} \right)^2 \right. \\
&+ \frac{r \left(\frac{6Mr^4}{(2l^2M+r^3)^2} - \frac{4Mr}{2l^2M+r^3} \right)^3}{4 \left(1 - \frac{2Mr^2}{2l^2M+r^3} \right)} + r \left(1 - \frac{2Mr^2}{2l^2M+r^3} \right)^{3/2} \\
&\times \left[\frac{3 \left(\frac{6Mr^4}{(2l^2M+r^3)^2} - \frac{4Mr}{2l^2M+r^3} \right)^3}{8 \left(1 - \frac{2Mr^2}{2l^2M+r^3} \right)^{5/2}} + \frac{\frac{324Mr^8}{(2l^2M+r^3)^4} - \frac{432Mr^5}{(2l^2M+r^3)^3} + \frac{120Mr^2}{(2l^2M+r^3)^2}}{2\sqrt{1 - \frac{2Mr^2}{2l^2M+r^3}}} \right. \\
&\left. - \frac{3 \left(\frac{36Mr^3}{(2l^2M+r^3)^2} - \frac{4M}{2l^2M+r^3} - \frac{36Mr^6}{(2l^2M+r^3)^3} \right) \left(\frac{6Mr^4}{(2l^2M+r^3)^2} - \frac{4Mr}{2l^2M+r^3} \right)}{4 \left(1 - \frac{2Mr^2}{2l^2M+r^3} \right)^{3/2}} \right] \\
&+ \frac{5}{2} r \left(\frac{6Mr^4}{(2l^2M+r^3)^2} - \frac{4Mr}{2l^2M+r^3} \right) \sqrt{1 - \frac{2Mr^2}{2l^2M+r^3}} \\
&\times \left[\frac{\frac{36Mr^3}{(2l^2M+r^3)^2} - \frac{4M}{2l^2M+r^3} - \frac{36Mr^6}{(2l^2M+r^3)^3} - \left(\frac{6Mr^4}{(2l^2M+r^3)^2} - \frac{4Mr}{2l^2M+r^3} \right)^2}{2\sqrt{1 - \frac{2Mr^2}{2l^2M+r^3}}} - \frac{\left(\frac{6Mr^4}{(2l^2M+r^3)^2} - \frac{4Mr}{2l^2M+r^3} \right)^2}{4 \left(1 - \frac{2Mr^2}{2l^2M+r^3} \right)^{3/2}} \right] \\
&+ \left(1 - \frac{2Mr^2}{2l^2M+r^3} \right)^{3/2} \times \left[\frac{\frac{36Mr^3}{(2l^2M+r^3)^2} - \frac{4M}{2l^2M+r^3} - \frac{36Mr^6}{(2l^2M+r^3)^3}}{2\sqrt{1 - \frac{2Mr^2}{2l^2M+r^3}}} \right. \\
&\left. - \frac{\left(\frac{6Mr^4}{(2l^2M+r^3)^2} - \frac{4Mr}{2l^2M+r^3} \right)^2}{4 \left(1 - \frac{2Mr^2}{2l^2M+r^3} \right)^{3/2}} \right] \left. \right\} \Theta^2, \tag{22}
\end{aligned}$$

$$g_{rr}^{(\Theta, l)} = \frac{1}{1 - \frac{2Mr^2}{2l^2M+r^3}} + \frac{\left(\frac{\frac{36Mr^3}{(2l^2M+r^3)^2} - \frac{4M}{2l^2M+r^3} - \frac{36Mr^6}{(2l^2M+r^3)^3} - \left(\frac{6Mr^4}{(2l^2M+r^3)^2} - \frac{4Mr}{2l^2M+r^3} \right)^2}{2\sqrt{1 - \frac{2Mr^2}{2l^2M+r^3}}} - \frac{\left(\frac{6Mr^4}{(2l^2M+r^3)^2} - \frac{4Mr}{2l^2M+r^3} \right)^2}{4 \left(1 - \frac{2Mr^2}{2l^2M+r^3} \right)^{3/2}} \right) \Theta^2}{4\sqrt{1 - \frac{2Mr^2}{2l^2M+r^3}}}, \tag{23}$$

$$\begin{aligned}
g_{\theta\theta}^{(\Theta, l)} &= r^2 + \frac{1}{16} \left\{ \frac{11}{2} r \left(\frac{6Mr^4}{(2l^2M+r^3)^2} - \frac{4Mr}{2l^2M+r^3} \right) - \frac{2Mr^2}{2l^2M+r^3} + 1 \right. \\
&+ \frac{4r^2 \left(\frac{6Mr^4}{(2l^2M+r^3)^2} - \frac{4Mr}{2l^2M+r^3} \right)^2}{1 - \frac{2Mr^2}{2l^2M+r^3}} + 12r^2 \sqrt{1 - \frac{2Mr^2}{2l^2M+r^3}} \\
&\times \left[\frac{\frac{36Mr^3}{(2l^2M+r^3)^2} - \frac{4M}{2l^2M+r^3} - \frac{36Mr^6}{(2l^2M+r^3)^3} - \left(\frac{6Mr^4}{(2l^2M+r^3)^2} - \frac{4Mr}{2l^2M+r^3} \right)^2}{2\sqrt{1 - \frac{2Mr^2}{2l^2M+r^3}}} - \frac{\left(\frac{6Mr^4}{(2l^2M+r^3)^2} - \frac{4Mr}{2l^2M+r^3} \right)^2}{4 \left(1 - \frac{2Mr^2}{2l^2M+r^3} \right)^{3/2}} \right] \left. \right\} \Theta^2 \tag{24}
\end{aligned}$$

$$\begin{aligned}
g_{\varphi\varphi}^{(\Theta,l)} = & r^2 \sin^2 \theta + \frac{1}{16} \left\{ \cos^2 \theta + 4 \left[r \left(\frac{6Mr^4}{(2l^2M+r^3)^2} - \frac{4Mr}{2l^2M+r^3} \right) \right. \right. \\
& - \frac{r \left(\frac{6Mr^4}{(2l^2M+r^3)^2} - \frac{4Mr}{2l^2M+r^3} \right)}{2 \left(1 - \frac{2Mr^2}{2l^2M+r^3} \right)} + \frac{r^2 \left(\frac{6Mr^4}{(2l^2M+r^3)^2} - \frac{4Mr}{2l^2M+r^3} \right)^2}{2 \left(1 - \frac{2Mr^2}{2l^2M+r^3} \right)} \\
& + r^2 \sqrt{1 - \frac{2Mr^2}{2l^2M+r^3}} \\
& \left. \times \left(\frac{\frac{36Mr^3}{(2l^2M+r^3)^2} - \frac{4M}{2l^2M+r^3} - \frac{36Mr^6}{(2l^2M+r^3)^3} - \frac{\left(\frac{6Mr^4}{(2l^2M+r^3)^2} - \frac{4Mr}{2l^2M+r^3} \right)^2}{4 \left(1 - \frac{2Mr^2}{2l^2M+r^3} \right)^{3/2}} \right) \right] \sin^2 \theta \right\} \Theta^2.
\end{aligned} \tag{25}$$

In order to obtain the event horizon r_h , we expand $1/g_{rr}^\Theta = 0$ up to the second order. It is important to mention that the explicit form for r_h (which is obtained analytically) will be omitted here since its very huge length. In Tab. I, we display quantitatively the horizon values in terms of Θ , l and M . It is worth commenting that the Kretschmann scalar contains 370.812 terms, and its expression will be omitted for obvious reasons. In the limit $r \rightarrow 0$, it becomes

$$\begin{aligned}
\tilde{\mathcal{K}}_{r \rightarrow 0} = & \frac{1024}{(\Theta^3 - 4l^2\Theta)^4} \left\{ 3(256l^8 - 512l^6\Theta^2 + 427l^4\Theta^4 - 134l^2\Theta^6 + 14\Theta^8) \right. \\
& \left. - 4(8l^4 - 6l^2\Theta^2 + \Theta^4)^2 \cos(2\theta) \sec^4(\theta) \right\}.
\end{aligned} \tag{26}$$

In other words, the black hole may remain regular under the enhancement of non-commutativity introduced via the non-commutative gauge theory. Moreover, an unusual dependence on the angle θ emerges, in contrast to the standard Hayward solution without non-commutativity, where $\tilde{\mathcal{K}}_{r \rightarrow 0}^{Hay} = 24/l^4$. Also, even in the implementation of non-commutativity through the non-commutative gauge theory applied to the Schwarzschild black hole, which yielded a regular solution $\tilde{\mathcal{K}}_{r \rightarrow 0}^{Schw(\Theta)} = \frac{6208}{3\Theta^4}$ [32], no dependence on θ was found. In addition, notice that this angular dependence implies that the expression for $\tilde{\mathcal{K}}_{r \rightarrow 0}$ must be evaluated within an appropriate domain to ensure regularity. In Fig. 1, the behavior of $\tilde{\mathcal{K}}_{r \rightarrow 0}$ is shown as a function of θ for a fixed value of $l = 0.1$. The plot indicates divergences when θ takes specific values, namely $\theta = \frac{\pi}{2} + n\pi$ (with $n \in \mathbb{Z}$).

Therefore, we conclude that our proposed solution remains regular if and only if the following condition is satisfied:

$$\theta \in \mathbb{R} \setminus \left\{ \frac{\pi}{2} + n\pi \mid n \in \mathbb{Z} \right\}, \tag{27}$$

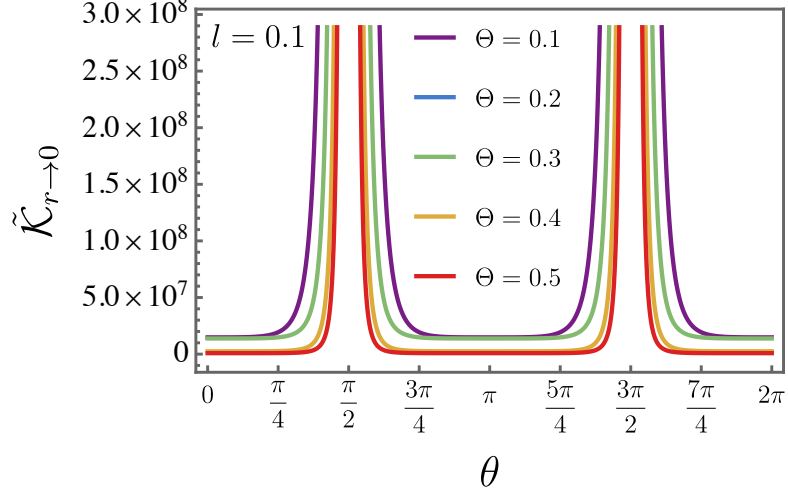


FIG. 1: The behavior of $\tilde{\mathcal{K}}_{r \rightarrow 0}$ as a function of θ for a fixed value of $l = 0.1$.

so that

$$\text{dom}(\tilde{\mathcal{K}}_{r \rightarrow 0}) = \{\theta \in \mathbb{R} \mid \cos(\theta) \neq 0\}. \quad (28)$$

M	l	Θ	r_h	M	l	Θ	r_h	M	l	Θ	r_h
1.0	0.01	0.1	1.99964	1.0	0.01	0.1	1.99964	1.0	0.01	0.00	——
1.1	0.01	0.1	2.19967	1.0	0.02	0.1	1.99949	1.0	0.01	0.10	1.99964
1.2	0.01	0.1	2.39970	1.0	0.03	0.1	1.99924	1.0	0.01	0.20	1.99870
1.3	0.01	0.1	2.59972	1.0	0.04	0.1	1.99889	1.0	0.01	0.30	1.99714
1.4	0.01	0.1	2.79974	1.0	0.05	0.1	1.99844	1.0	0.01	0.40	1.99496
1.5	0.01	0.1	2.99976	1.0	0.06	0.1	1.99788	1.0	0.01	0.50	1.99217
1.6	0.01	0.1	3.19977	1.0	0.07	0.1	1.99723	1.0	0.01	0.60	1.98877
1.7	0.01	0.1	3.39979	1.0	0.08	0.1	1.99648	1.0	0.01	0.70	1.98476
1.8	0.01	0.1	3.59980	1.0	0.09	0.1	1.99562	1.0	0.01	0.80	1.98016
1.9	0.01	0.1	3.79981	1.0	0.10	0.1	1.99466	1.0	0.01	0.90	1.97498
2.0	0.01	0.1	3.99982	1.0	0.11	0.1	1.99360	1.0	0.01	0.99	1.96983

TABLE I: The table presents a quantitative analysis of the event horizon r_h for various values of M , l , and Θ .

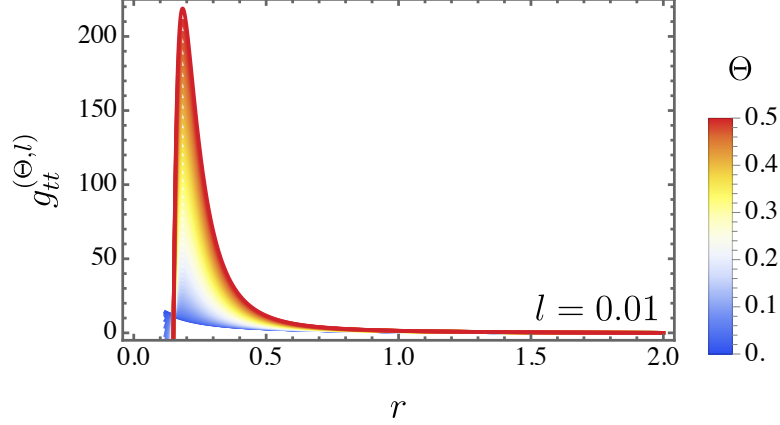


FIG. 2: The metric component $g_{tt}^{(\Theta, l)}$ as a function of r for different values of the non-commutative parameter Θ , with l fixed at 0.01.

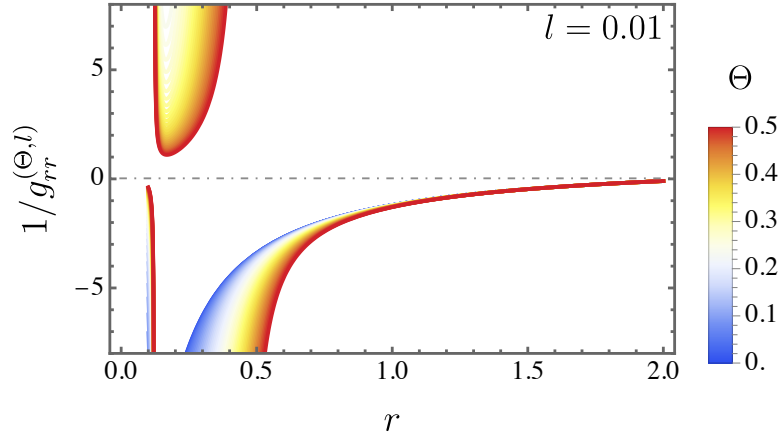


FIG. 3: The metric component $1/g_{rr}^{(\Theta, l)}$ as a function of r for different values of the non-commutative parameter Θ , with l fixed at 0.01.

III. THERMODYNAMICS

This section examines the thermodynamic properties of the system, beginning with the Hawking temperature, $T^{(\Theta, l)}$, derived from the surface gravity. The analysis then extends to the entropy, $S^{(\Theta, l)}$, and heat capacity, $C_V^{(\Theta, l)}$. Due to their extensive length, the explicit expressions for these quantities, apart from the Hawking temperature, will be omitted.

Furthermore, all thermodynamic state quantities will be plotted as functions of the mass M . As will be shown, the behavior of $T^{(\Theta, l)}$ suggests the existence of a remnant mass, characterized by the condition $T^{(\Theta, l)} \rightarrow 0$.

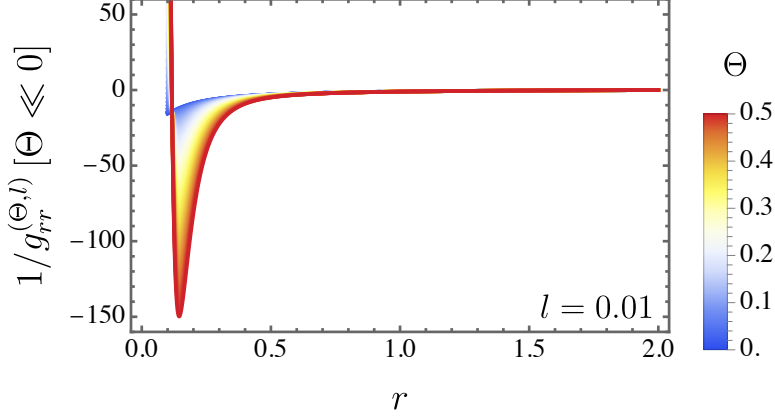


FIG. 4: The metric component $1/g_{rr}^{(\Theta, l)}$, in the regime of small Θ , as a function of r for different values of the non-commutative parameter Θ , with l fixed at 0.01.

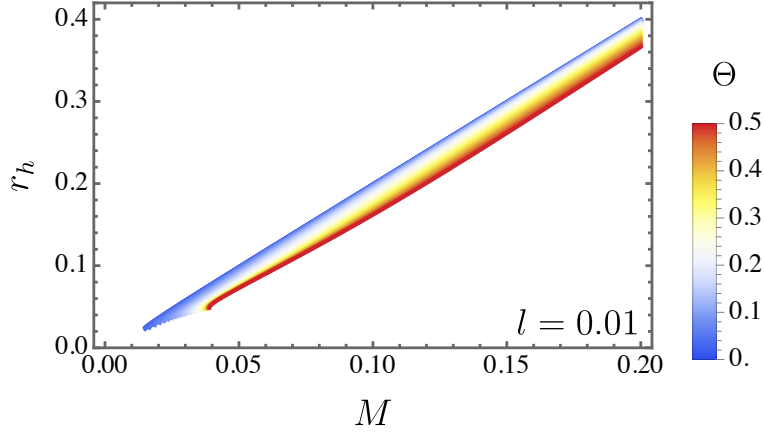


FIG. 5: The event horizon r_h as a function of M for different values of the parameter Θ , with a fixed case at $l = 0.01$.

A. Hawking temperature

By using the surface gravity approach, the Hawking temperature reads

$$\begin{aligned}
 T^{(\Theta, l)} &= \frac{1}{4\pi \sqrt{g_{tt}^\Theta g_{rr}^\Theta}} \left. \frac{dg_{tt}^\Theta}{dr} \right|_{r=r_h} = \frac{1}{\varrho} \times \left\{ Mr_h \left[-2(4l^2 M - r_h^3)(2l^2 M + r_h^3)^4 \right. \right. \\
 &+ (64l^8 M^4(2M + 15r_h) + 12l^4 M^2 r_h^6(304M - 51r_h) + r_h^{12}(11M - 3r_h) \\
 &\left. \left. + 4l^2 M r_h^9(66r_h - 191M) - 8l^6 M^3 r_h^3(307M + 228r_h) \right) \Theta^2 \right] \right\}, \quad (29)
 \end{aligned}$$

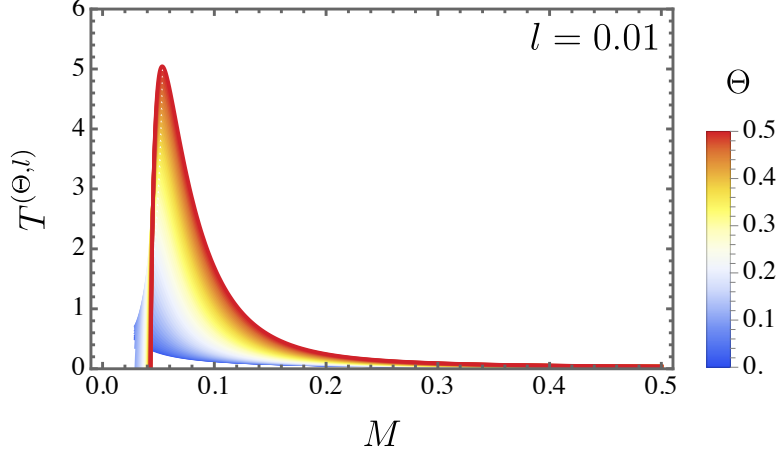


FIG. 6: The Hawking temperature $T^{(\Theta, l)}$ is plotted as a function of mass M for different values of Θ , with l fixed at 0.01.

where

$$\begin{aligned}
\varrho = \pi (2l^2 M + r_h^3)^6 & \left\{ \frac{1}{(2l^2 M + r_h^3)^7 (2l^2 M + r_h^2(r_h - 2M))^2} \right. \\
& \times \left[4 (2l^2 M + r_h^3)^3 (2l^2 M + r_h^2(r_h - 2M)) \right. \\
& + \Theta^2 M (-16l^6 M^3 + 48l^4 M^2 r_h^3 + 24l^2 M r_h^5 (r_h - 2M) + r_h^8 (3M - 2r_h)) \left. \right] \\
& \times \left[4 (2l^2 M + r_h^3)^4 (2l^2 M + r_h^2(r_h - 2M)) \right. \\
& + M (-32l^8 M^4 - 48l^4 M^2 r_h^5 (17M + r_h) + 2l^2 M r_h^8 (201M - 80r_h) \\
& \left. \left. + 16l^6 M^3 r_h^2 (8M + 35r_h) + r_h^{11} (4r_h - 11M)) \Theta^2 \right] \right\}^{1/2}. \quad (30)
\end{aligned}$$

In Fig. 6, we present the behavior of $T^{(\Theta, l)}$ as a function of mass M . In general, as Θ increases (with l fixed at 0.01), the magnitude of $T^{(\Theta, l)}$ also increases. Notably, the Hawking temperature vanishes at specific values of M for a given Θ , indicating the presence of remnant masses. The explicit expression for these masses will be omitted due to its considerable length.

B. Entropy

Subsequently, let us address the entropy, which is defined as

$$S^{(\Theta, l)} = \pi r_h^2. \quad (31)$$

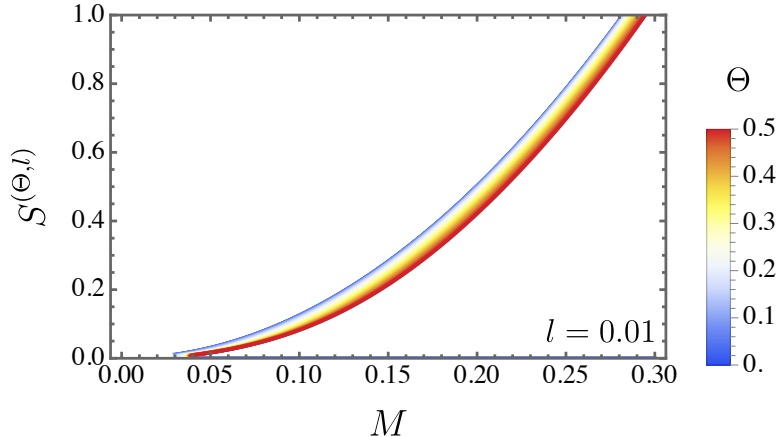


FIG. 7: The entropy $S^{(\Theta, l)}$ as a function of mass M for different values of Θ , with l fixed at 0.01.

As previously stated at the beginning of this section, the full expression for $S^{(\Theta, l)}$ is omitted due to its extensive length. However, to illustrate its behavior, we present Fig. 7. For a fixed mass M , the entropy decreases as Θ increases.

C. Heat capacity

Finally, for finishing the thermodynamic behavior analysis in this study, we present the heat capacity, which is given by

$$C_V^{(\Theta, l)} = T \frac{\partial S}{\partial T} = \frac{\partial S}{\frac{\partial T}{\partial M}}. \quad (32)$$

In Fig. 8, we illustrate the behavior of the heat capacity, highlighting the modifications introduced by the non-commutative parameter Θ . Indeed, the heat capacity exhibits two distinct regions, characterized by the presence of both positive and negative values.

IV. QUANTUM RADIATION

In this section, building on the previous analysis, where we verified that the black hole under consideration emits thermal radiation through the Hawking temperature calculation, we now examine this quantum radiation — the Hawking radiation. Specifically, we consider both particle modes: fermions and bosons. The particle creation densities for each case are computed, followed by a comparison to determine which mode exhibits a higher particle

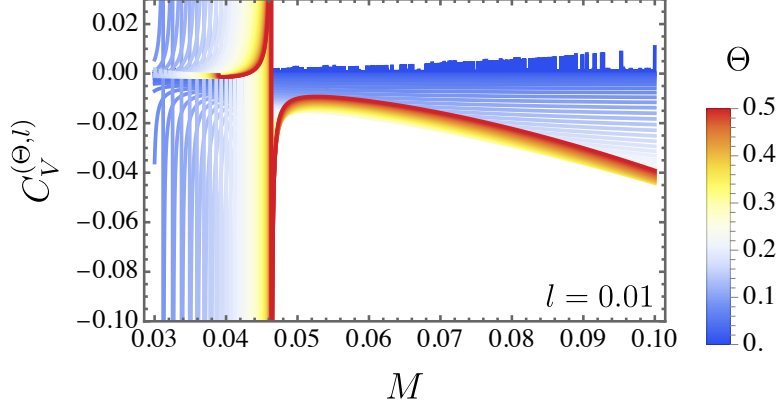


FIG. 8: The heat capacity plotted as a function of mass M for different values of Θ , with l fixed at 0.01.

creation rate. As we shall see, for a given frequency ω , bosons are emitted more abundantly than fermions.

A. Bosonic particle modes

To accomplish our analysis, let us consider following configuration to the metric tensor

$$ds^2 = g_{tt}^{(\Theta, l)}(r)dt^2 + g_{rr}^{(\Theta, l)}(r)dr^2 + g_{\theta\theta}^{(\Theta, l)}(r, \theta)d\theta^2 + g_{\varphi\varphi}^{(\Theta, l)}(r, \theta)d\varphi^2. \quad (33)$$

Within the Hamilton–Jacobi framework, the equation describing radial motion for a massless particle is given by [135, 168, 169].

$$\frac{1}{g_{tt}^{(\Theta, l)}(r)}(\partial_t I)^2 + \frac{1}{g_{rr}^{(\Theta, l)}(r)}(\partial_r I)^2 = 0. \quad (34)$$

As it can be seen below, the classical action can be written with the plus and minus signs representing outgoing and ingoing particles, respectively

$$I_{\pm} = -\omega t \pm \int \omega \frac{dr}{\sqrt{\frac{|g_{tt}^{(\Theta, l)}(r)|}{g_{rr}^{(\Theta, l)}(r)}}}, \quad (35)$$

where $\omega = -\partial_t I$ denotes the Killing energy. Taking into account the near–horizon expansion, we have

$$g_{tt}^{(\Theta, l)}(r) = \frac{d}{dr} \left(g_{tt}^{(\Theta, l)}(r) \right) \Big|_{r=r_h} (r - r_h) + \dots, \quad \frac{1}{g_{rr}^{(\Theta, l)}(r)} = \frac{d}{dr} \left(\frac{1}{g_{rr}^{(\Theta, l)}(r)} \right) \Big|_{r=r_h} (r - r_h) + \dots, \quad (36)$$

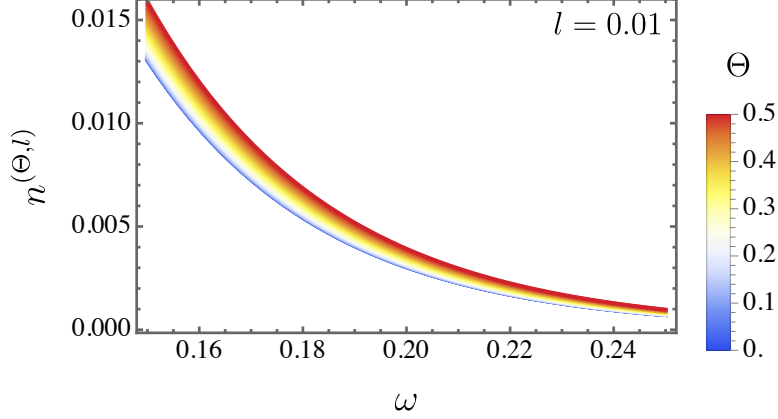


FIG. 9: The particle creation density n is presented as a function of the frequency ω for a fixed value of $l = 0.01$ and different values of Θ .

and applying Feynman's method, we directly obtain

$$\text{Im} \int dI_+ - \text{Im} \int dI_- = \frac{\pi\omega}{\kappa}, \quad (37)$$

with

$$\kappa = \frac{1}{2} \sqrt{\left. \frac{d}{dr} \left(g_{tt}^{(\Theta, l)}(r) \right) \right|_{r=r_h} \left. \frac{d}{dr} \left(\frac{1}{g_{rr}^{(\Theta, l)}(r)} \right) \right|_{r=r_h}}, \quad (38)$$

is, therefore, the so-called surface gravity. By defining

$$\Gamma = e^{-\frac{2\pi\omega}{\kappa}}, \quad (39)$$

we directly obtain the particle creation density n for fermions, which can be determined as

$$n = \frac{\Gamma}{1 - \Gamma}. \quad (40)$$

Fig. 9 illustrates the particle creation for bosonic modes, represented by n . Overall, the non-commutative parameter enhances the magnitude of n for a fixed value of $l = 0.01$.

B. Fermionic particle modes

In this section, it is crucial to note that the upcoming calculations disregard backreaction effects. Within the quantum tunneling framework, particles can escape a black hole by passing through the event horizon. The probability associated with this process can be derived using the methods described in Refs. [170–172] (and the references therein).

Black hole radiation, akin to black body radiation, emerges due to their intrinsic temperature. However, this emission spectrum is influenced by greybody factors, which modify the outgoing radiation. The spectrum is expected to include particles of different spins, such as fermions. Studies initiated by Kerner and Mann [173], followed by further research [174–179], indicate that massless bosons and fermions radiate at the same temperature. Moreover, analyses of spin-1 bosons suggest that the Hawking temperature remains unchanged even when higher-order quantum corrections in \hbar beyond the semiclassical regime are considered [180, 181].

The behavior of fermions is often described through the phase of their spinor wave function, which follows the Hamilton–Jacobi equation. An alternative expression for the action, as presented in [135, 182, 183], is given by

$$\mathcal{S}^{(\Psi)} = S^{(0)} + \psi^{(\uparrow\downarrow)}, \quad (41)$$

where S_0 corresponds to the classical action for scalar particles and $\psi^{(\uparrow\downarrow)}$ accounts for the spin corrections. The additional spin-dependent terms account for the interaction between the particle’s spin and the background spin connection, ensuring no singularities arise at the event horizon. Since these corrections primarily influence spin precession and remain small, they are not considered in this study. Furthermore, the spin of the emitted particles has an insignificant effect on the black hole’s angular momentum, especially in the case of non-rotating black holes with masses far exceeding the Planck scale [135]. On average, particles with opposite spins are emitted in a balanced manner, maintaining the black hole’s total angular momentum effectively unchanged.

This analysis focuses on the tunneling of fermionic particles as they cross the event horizon of a particular black hole solution. Alternative methods employing generalized Painlevé–Gullstrand or Kruskal–Szekeres coordinates are discussed in the foundational work [173]. The investigation begins with a general spacetime metric, as expressed in Eq. (33). In curved spacetime, fermionic dynamics are dictated by the Dirac equation, which is formulated as:

$$(\tilde{\gamma}^\mu \nabla_\mu + m) \Psi(x) = 0 \quad (42)$$

with

$$\nabla_\mu = \partial_\mu + \frac{i}{2} \Gamma_\mu^{\alpha\beta} \tilde{\Sigma}_{\alpha\beta} \quad (43)$$

and

$$\tilde{\Sigma}_{\alpha\beta} = \frac{\mathfrak{i}}{4}[\tilde{\gamma}_\alpha, \tilde{\gamma}_\beta]. \quad (44)$$

It is important to note that the coordinates are denoted as $x \equiv t, r, \theta, \varphi$. The matrices $\tilde{\gamma}^\mu$ accounts for the fundamental properties of the Clifford algebra, which are expressed through the relation:

$$\{\tilde{\gamma}_\alpha, \tilde{\gamma}_\beta\} = 2g_{\alpha\beta}\mathbb{1}, \quad (45)$$

with $\mathbb{1}$ denotes the 4×4 identity matrix. Within this formulation, the $\tilde{\gamma}$ matrices are specified as given below:

$$\begin{aligned} \tilde{\gamma}^t &= \frac{\mathfrak{i}}{\sqrt{|g_{tt}^{(\Theta,l)}|}} \begin{pmatrix} \mathbf{1} & \mathbf{0} \\ \mathbf{0} & -\mathbf{1} \end{pmatrix}, \quad \tilde{\gamma}^r = \sqrt{\frac{1}{g_{rr}^{(\Theta,l)}}} \begin{pmatrix} \mathbf{0} & \tilde{\sigma}_3 \\ \tilde{\sigma}_3 & \mathbf{0} \end{pmatrix}, \\ \tilde{\gamma}^\theta &= \frac{1}{r} \begin{pmatrix} \mathbf{0} & \tilde{\sigma}_1 \\ \tilde{\sigma}_1 & \mathbf{0} \end{pmatrix}, \quad \tilde{\gamma}^\varphi = \frac{1}{r \sin \theta} \begin{pmatrix} \mathbf{0} & \tilde{\sigma}_2 \\ \tilde{\sigma}_2 & \mathbf{0} \end{pmatrix}. \end{aligned}$$

In this context, $\tilde{\sigma}$ corresponds to the Pauli matrices, which obey the conventional commutation relation: $\tilde{\sigma}_i \tilde{\sigma}_j = \mathbf{1} \delta_{ij} + \mathfrak{i} \varepsilon_{ijk} \tilde{\sigma}_k$, where $i, j, k = 1, 2, 3$. Additionally, the matrix associated with $\tilde{\gamma}^5$ can be equivalent to

$$\tilde{\gamma}^5 = \mathfrak{i} \tilde{\gamma}^t \tilde{\gamma}^r \tilde{\gamma}^\theta \tilde{\gamma}^\varphi = \mathfrak{i} \sqrt{\frac{1}{g_{tt}^{(\Theta,l)}(r) g_{rr}^{(\Theta,l)}(r)}} \frac{1}{r^2 \sin \theta} \begin{pmatrix} \mathbf{0} & -\mathbf{1} \\ \mathbf{1} & \mathbf{0} \end{pmatrix}.$$

In order to describe a Dirac field with its spin aligned upward along the positive r -axis, the adopted ansatz is given by [184]:

$$\Psi^{(+)}(x) = \begin{pmatrix} \tilde{H}(x) \\ 0 \\ \tilde{Y}(x) \\ 0 \end{pmatrix} \exp [\mathfrak{i} \psi^{(+)}(x)]. \quad (46)$$

This study focuses on the spin-up (+) configuration, while the spin-down (−) case, oriented along the negative r -axis, follows a similar treatment. Substituting the ansatz (46)

into the Dirac equation leads to

$$\begin{aligned}
& - \left(\frac{\mathfrak{i} \tilde{H}(x)}{\sqrt{g_{tt}^{(\Theta,l)}(r)}} \partial_t \psi^{(+)} + \tilde{Y}(x) \sqrt{\frac{1}{g_{rr}^{(\Theta,l)}(r)}} \partial_r \psi^{(+)} \right) + \tilde{H}(x) m = 0, \\
& - \frac{\tilde{Y}(r)}{r} \left(\partial_\theta \psi^{(+)} + \frac{\mathfrak{i}}{\sin \theta} \partial_\varphi \psi^{(+)} \right) = 0, \\
& \left(\frac{\mathfrak{i} \tilde{Y}(x)}{\sqrt{g_{tt}^{(\Theta,l)}(r)}} \partial_t \psi^{(+)} - \tilde{H}(x) \sqrt{\frac{1}{g_{rr}^{(\Theta,l)}(r)}} \partial_r \psi^{(+)} \right) + \tilde{Y}(x) m = 0, \\
& - \frac{\tilde{H}(x)}{r} \left(\partial_\theta \psi^{(+)} + \frac{\mathfrak{i}}{\sin \theta} \partial_\varphi \psi^{(+)} \right) = 0,
\end{aligned} \tag{47}$$

and considering the action expressed as

$$\psi^{(+)} = -\omega t + \tilde{\chi}(r) + L(\theta, \varphi) \tag{48}$$

which leads to [135]

$$\left(\frac{\mathfrak{i} \omega \tilde{H}(x)}{\sqrt{g_{tt}^{(\Theta,l)}(r)}} - \tilde{Y}(x) \sqrt{\frac{1}{g_{rr}^{(\Theta,l)}(r)}} \tilde{\chi}'(r) \right) + m \tilde{H}(x) = 0, \tag{49}$$

$$-\frac{\tilde{H}(x)}{r} \left(L_\theta + \frac{\mathfrak{i}}{\sin \theta} L_\varphi \right) = 0, \tag{50}$$

$$-\left(\frac{\mathfrak{i} \omega \tilde{Y}(x)}{\sqrt{g_{tt}^{(\Theta,l)}(r)}} + \tilde{H}(x) \sqrt{\frac{1}{g_{rr}^{(\Theta,l)}(r)}} \tilde{\chi}'(r) \right) + \tilde{Y}(x) m = 0, \tag{51}$$

$$-\frac{\tilde{H}(x)}{r} \left(L_\theta + \frac{\mathfrak{i}}{\sin \theta} L_\varphi \right) = 0. \tag{52}$$

The specific forms of $\tilde{H}(x)$ and $\tilde{Y}(x)$ do not affect the conclusion that Eqs. (50) and (52) impose the constraint $L_\theta + \mathfrak{i}(\sin \theta)^{-1} L_\varphi = 0$, implying that $L(\theta, \varphi)$ must be a complex function. This condition holds for both outgoing and ingoing scenarios. Consequently, when computing the ratio of outgoing to ingoing probabilities, the terms involving L cancel out, allowing it to be omitted from further analysis. In the case of massless particles, Eqs. (49) and (51) lead to two independent solutions:

$$\tilde{H}(x) = -\mathfrak{i} \tilde{Y}, \quad \tilde{\chi}'(r) = \tilde{\chi}'_{\text{out}} = \frac{\omega}{\sqrt{\frac{g_{tt}^{(\Theta,l)}(r)}{g_{rr}^{(\Theta,l)}(r)}}}, \tag{53}$$

$$\tilde{H}(x) = \mathfrak{i} \tilde{Y}(x), \quad \tilde{\chi}'(r) = \tilde{\chi}'_{\text{in}} = -\frac{\omega}{\sqrt{\frac{g_{tt}^{(\Theta,l)}(r)}{g_{rr}^{(\Theta,l)}(r)}}}. \tag{54}$$

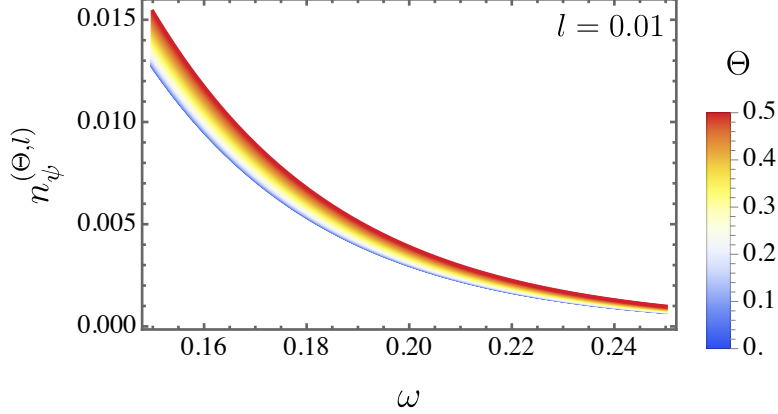


FIG. 10: The particle creation density n_ψ is presented as a function of the frequency ω for different values of the non-commutative parameter Θ , with a fixed value of $l = 0.01$.

In this context, $\tilde{\chi}_{\text{out}}$ and $\tilde{\chi}_{\text{in}}$ represent the solutions associated with outgoing and incoming particles, respectively [135]. Consequently, the overall tunneling probability takes the form $\tilde{\Gamma}_\psi \sim e^{-2\text{Im}(\tilde{\chi}_{\text{out}} - \tilde{\chi}_{\text{in}})}$. Therefore,

$$\tilde{\chi}_{\text{out}}(r) = -\tilde{\chi}_{\text{in}}(r) = \int dr \frac{\omega}{\sqrt{\frac{g_{tt}^{(\Theta,l)}(r)}{g_{rr}^{(\Theta,l)}(r)}}}. \quad (55)$$

A key aspect is that the dominant energy condition, together with Einstein's field equations, guarantees that $g_{tt}^{(\Theta,l)}(r)$ and $1/g_{rr}^{(\Theta,l)}(r)$ share the same zeros. Near $r = r_h$, these metric components exhibit a linear behavior, revealing the presence of a simple pole with a well-defined coefficient. By employing Feynman's approach, the following expression is obtained:

$$2\text{Im}(\tilde{\chi}_{\text{out}} - \tilde{\chi}_{\text{in}}) = \text{Im} \int dr \frac{4\omega}{\sqrt{\frac{g_{tt}^{(\Theta,l)}(r)}{g_{rr}^{(\Theta,l)}(r)}}} = \frac{2\pi\omega}{\kappa}. \quad (56)$$

In this setting, the particle density n_ψ corresponding to the given black hole solution follows the relation $\tilde{\Gamma}_\psi \sim e^{-\frac{2\pi\omega}{\kappa}}$

$$n_\psi = \frac{1}{e^{\frac{2\pi\omega}{\kappa}} + 1}. \quad (57)$$

Fig. 10 illustrates the particle creation density for fermions, n_ψ . Similar to the bosonic scenario, the non-commutative parameter Θ contributes to an increase in the magnitude of the particle creation density. Additionally, Fig. 11 presents a comparison of the particle creation densities for bosons and fermions. Overall, the bosonic case exhibits a greater magnitude at lower frequencies compared to the fermionic case.

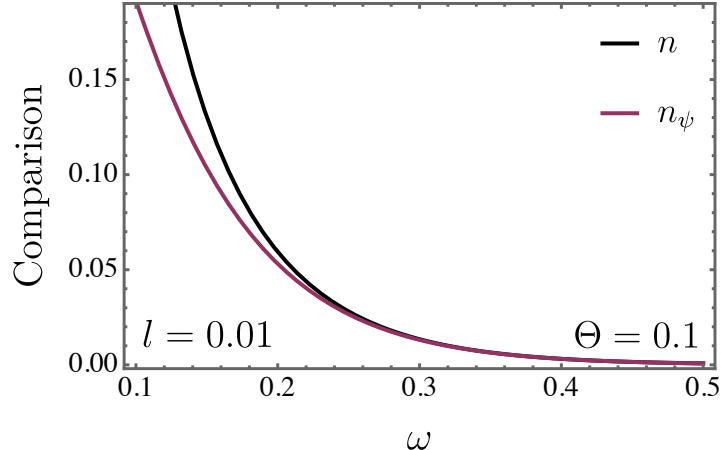


FIG. 11: The particle creation density n_ψ is depicted as a function of the frequency ω for different values of the non-commutative parameter Θ , while keeping $l = 0.01$ fixed.

V. THE SCALAR PERTURBATION

In this section, we examine the evolution of a massless scalar field. To achieve this, first, we explore the non-commutative modifications to the Hayward black hole spacetime by incorporating correction terms arising from the non-commutative geometry framework expressed in Eq. (22–25). The modified metric accounting for these corrections can be expressed as $g_{ij}^{NC} = g_{ij} + \Theta^2 \mathcal{G}_{ij}^{NC}$, where g_{ij} represents the original Hayward black hole metric, while \mathcal{G}_{ij}^{NC} contains the coefficients associated with the non-commutative corrections, as discussed in Refs. [9, 32, 185].

We follow the method introduced in Ref. [186]. In this intriguing approach, a deformed metric remains both stationary and axisymmetric in the modified approach. This deformation is governed by a small dimensionless parameter ϵ , leading to an alternative description of the black hole geometry. Applying this approach, the initial metric represented in Eq. (22–25) are reformed in a cos series as

$$g_{tt}^{(\Theta,l)} = -f(r)(1 + \epsilon A_j \cos^j \theta), \quad (58)$$

$$g_{rr}^{(\Theta,l)} = f(r)^{-1}(1 + \epsilon B_j \cos^j \theta), \quad (59)$$

$$g_{\theta\theta}^{(\Theta,l)} = r^2(1 + \epsilon C_j \cos^j \theta), \quad (60)$$

$$g_{\phi\phi}^{(\Theta,l)} = r^2 \sin^2 \theta (1 + \epsilon D_j \cos^j \theta), \quad (61)$$

$$g_{t\theta}^{(\Theta,l)} = \epsilon a_j(r) \cos^j \theta, \quad g_{r\theta}^{(\Theta,l)} = \epsilon c_j(r) \cos^j \theta, \quad g_{\theta\phi}^{(\Theta,l)} = \epsilon e_j(r) \cos^j \theta, \quad (62)$$

$$g_{t\theta}^{(\Theta,l)} = \epsilon b_j(r) \cos^j \theta, \quad g_{r\phi}^{(\Theta,l)} = \epsilon d_j(r) \cos^j \theta. \quad (63)$$

$$(64)$$

where $f(r) = \left(1 - \frac{2Mr^2}{r^3 + 2Ml^2}\right)$, is the lapse function of the Hayward black hole and the small deformed parameter is equivalent to the NC parameter ($\epsilon = \Theta^2$). Consequently, by following Ref. [10, 186], the deformed coefficients of the metric are derived as

$$A_0 = -\frac{1}{4(2l^2M + r^3)^4(2l^2M + r^2(r - 2M))} \left(M(32l^8M^4 - 16l^6M^3r^2(8M + 35r) + \right. \quad (65)$$

$$\left. 48l^4M^2r^5(17M + r) + 2l^2Mr^8(80r - 201M) + r^{11}(11M - 4r) \right) \quad (66)$$

$$B_0 = \frac{M(-16l^6M^3 + 48l^4M^2r^3 + 24l^2Mr^5(r - 2M) + r^8(3M - 2r))}{4(2l^2M + r^3)^3(2l^2M + r^2(r - 2M))}, \quad (67)$$

$$C_0 = \frac{1}{16r^2(2l^2M + r^3)^3(2l^2M + r^2(r - 2M))} \left(16l^8M^4 + 16l^6M^3r^2(2r - 25M) + \right. \quad (68)$$

$$\left. 4l^4M^2r^4(112M^2 + 99Mr + 6r^2) + 4l^2Mr^7(-161M^2 + 66Mr + 2r^2) + \right. \quad (69)$$

$$\left. r^{10}(34M^2 - 17Mr + r^2) \right), \quad (70)$$

$$D_0 = \frac{M(-32l^6M^3 + 4l^4M^2r^2(16M + 9r) + 8l^2Mr^5(3r - 7M) + r^8(M - r))}{4(2l^2M + r^3)^3(2l^2M + r^2(r - 2M))}, \quad (71)$$

$$A_j = B_j = C_j = 0 \quad \text{and} \quad D_j = \frac{1 + (-1)^j}{32r^2} \quad \text{for} \quad j > 0, \quad (72)$$

$$a_j(r) = b_j(r) = c_j(r) = d_j(r) = 0. \quad (73)$$

Now, we start by expressing the Klein–Gordon equation in curved spacetime as follow:

$$\frac{1}{\sqrt{-g}} \partial_\mu (\sqrt{-g} g^{\mu\nu} \partial_\nu \psi) = 0. \quad (74)$$

Next, we decompose the scalar field ψ in terms of the two Killing vectors ∂_t and ∂_ϕ that generate the symmetries of the spacetime. The wave function can be written as a sum over

angular and radial modes

$$\psi = \int_{-\infty}^{\infty} d\omega \sum_{m=-\infty}^{\infty} e^{im\varphi} D_{m,\omega}^2 \psi_{m,\omega}(r, \theta) e^{-i\omega t}, \quad (75)$$

where $D_{m,\omega}^2 \psi_{m,\omega}(r, \theta) = 0$ and m and ω are the azimuthal number and mode frequency, respectively. To account for non-commutative corrections up to first order in Θ^2 , we expand the operator $D_{m,\omega}^2 \psi_{m,\omega}$ as follows [10, 186]

$$D_{m,\omega}^2 = D_{(0)m,\omega}^2 + \Theta^2 D_{(1)m,\omega}^2. \quad (76)$$

Substituting the metric coefficients from Eqs. ((58) – (64)) into the Klein–Gordon equation, we obtain the following expressions for the operators

$$D_{(0)m,\omega}^2 = - \left(\omega^2 - \frac{m^2 f(r)}{r^2 \sin^2 \theta} \right) - \frac{f(r)}{r^2} \partial_r (r^2 f(r) \partial_r) - \cos \theta \partial_r (r^2 f(r) \partial_r) \quad (77)$$

$$- \frac{f(r)}{r^2 \sin^2 \theta} \partial_\theta (\sin \theta \partial_\theta), \quad (78)$$

$$D_{(1)m,\omega}^2 = \frac{m^2 f(r)}{r^2 \sin^2 \theta} (A_j - D_j) \cos \theta - \frac{f(r)}{r^2} (A_j - B_j) \cos \theta \partial_r (r^2 f(r) \partial_r) \quad (79)$$

$$- \frac{f(r)^2}{r^2} (A'_j - B'_j + C'_j + D'_j) \cos \theta \partial_r - \frac{f(r)}{r^2} (A_j - C_j) \cos \theta (\cot \theta \partial_\theta + \partial_\theta^2) \quad (80)$$

$$- \frac{f(r)}{2r^2} (A_j + B_j - C_j + D_j) \partial_\theta \cos \theta \partial_\theta - \frac{2i\omega f(r)}{r} a_j \cos \theta (r \partial_r + 1). \quad (81)$$

We also introduce the tortoise coordinate r^* , which is defined by

$$\frac{dr^*}{dr} = \frac{1}{f(r) \left(1 + \frac{1}{2} \Theta^2 b_{lm}^j (A_j - B_j) \right)}. \quad (82)$$

Expanding $\psi_{m,\omega}$ in terms of Legendre functions $P_{lm}(\cos \theta)$ and radial wave functions $R_{l,m}(r)$, we write the field as

$$\psi_{m,\omega} = \sum_{l'=|m|}^{\infty} P_{l'}^m(\cos \theta) R_{l',m}(r), \quad (83)$$

and the radial wave function satisfies the Schrödinger–like equation

$$\partial_{r^*}^2 \Psi_{lm} + \omega^2 \Psi_{lm} = V_{\text{eff}}(r) \Psi_{lm}, \quad (84)$$

and the effective potential V_{eff} is then given by

$$V_{\text{eff}} = V_{\text{H}} + \Theta^2 V_{\text{NC}}, \quad (85)$$

where V_H is the effective potential for the original black hole in the commutative scenario

$$V_H = f(r) \left(\frac{\ell(\ell+1)}{r^2} + \frac{1}{r} \frac{df(r)}{dr} \right), \quad (86)$$

and V_{NC} represents the non-commutative correction to the potential which can be obtained after performing the necessary algebraic manipulations

$$\begin{aligned} V_{\text{NC}} = & \frac{f(r)}{r} \frac{df(r)}{dr} b_{lm}^0 (A_0 - B_0) + \left[\frac{f(r)}{r^2} (a_{lm}^0 (A_0 - D_0) - c_{lm}^0 (A_0 - C_0)) \right. \\ & \left. - \frac{d_{lm}^0}{2} (A_0 + B_0 - C_0 + D_0) + \frac{1}{4r^2} \frac{d}{dr^*} \left(b_{lm}^0 r^2 \frac{d}{dr^*} (A_0 - B_0 + C_0 + D_0) \right) - \frac{b_{lm}^0}{4} \frac{d^2}{dr^{*2}} (A_0 - B_0) \right] \\ & - \frac{f(r)}{r^2} \sum_{j=1}^{\infty} \left(a_{lm}^j + \frac{1}{2} d_{lm}^j \right) D_j + \sum_{j=1}^{\infty} \frac{1}{4r^2} \frac{d}{dr^*} \left(b_{lm}^j r^2 \frac{d}{dr^*} \right) D_j. \end{aligned}$$

The coefficients $a_{lm}^j, b_{lm}^j, c_{lm}^j, d_{lm}^j$ are calculated based on the specific values of the non-commutative parameter Θ , the multipole number $\ell (m = \pm 1)$, as detailed in Ref. [10]. Notably, the effective potential, when extended to the non-commutative formalism, depends not only on the multipole ℓ but also on the azimuthal number m . In addition, these coefficients are the same for \pm of each azimuthal number m . For example, the explicit form of V_{eff} for $\ell = 1 (m = \pm 1)$ is given by (where $\tilde{\mathcal{A}}(r) \equiv \tilde{A}(r)$)

$$\begin{aligned} V_{\text{eff}} = & \frac{1}{4096r^4 \tilde{A}(r)} \left\{ 8192r^2 \tilde{A}(r)^3 \left(r \tilde{A}(r) \tilde{A}'(r) + 1 \right) + \Theta^2 \xi \tilde{A}(r)^2 + \Theta^2 \left[-8\Theta^2 r^4 \tilde{\xi} \tilde{A}(r) \tilde{A}'(r)^6 \right. \right. \\ & \left. \left. - 16\Theta^4 r^5 \tilde{A}'(r)^9 + 4r \tilde{\xi} \tilde{A}(r)^2 \tilde{A}'(r) - 2\Theta^4 r^3 \tilde{A}(r)^9 \tilde{A}^{(3)}(r) \tilde{A}^{(4)}(r) \Theta^2 + r \chi \tilde{A}(r)^8 \right. \right. \\ & \left. \left. \tilde{\Xi} \tilde{A}(r)^5 + 2r \tilde{\chi} \tilde{A}(r)^4 + 2r^2 \tilde{\chi} \tilde{A}(r)^3 \tilde{A}'(r) + \tilde{\Xi} \tilde{A}(r)^7 + \Xi r \tilde{A}(r)^6 \right] \right\}, \quad (87) \end{aligned}$$

where

$$\begin{aligned} \xi = & - \left(\Theta^2 r \tilde{A}(r)^2 \tilde{A}^{(3)}(r) + 2\Theta^2 r \tilde{A}'(r)^3 + \tilde{A}(r) \left[\Theta^2 \tilde{A}'(r) (5r \tilde{A}''(r) + 2\tilde{A}'(r)) + 8 \right] \right) \\ & \times \left(\Theta^2 r^2 \tilde{A}(r)^3 \tilde{A}^{(4)}(r) + 2\Theta^2 r^2 \tilde{A}'(r)^4 + 4r \tilde{A}(r) \tilde{A}'(r) \left[\Theta^2 \tilde{A}'(r) (4r \tilde{A}''(r) + \tilde{A}'(r)) + 4 \right] \right. \\ & \left. + \tilde{A}(r)^2 \left[\Theta^2 (5r^2 \tilde{A}''(r)^2 - 2\tilde{A}'(r)^2 + 4r \tilde{A}'(r) (2r \tilde{A}^{(3)}(r) + \tilde{A}''(r))) - 8 \right] \right) - 192 \tilde{A}(r), \quad (88) \end{aligned}$$

$$\tilde{\xi} = \Theta^2 \tilde{A}'(r) \left(-5r \tilde{A}''(r) + 8r^2 \tilde{A}'(r)^3 - 2\tilde{A}'(r) \right) + 8, \quad (89)$$

$$\begin{aligned}
\bar{\xi} = & r^2 \tilde{A}'(r)^2 \left[\Theta^2 \tilde{A}'(r) \left(96 r \tilde{A}''(r) + 3 \Theta^2 r^2 \tilde{A}'(r)^5 \right. \right. \\
& + 4 (5 \Theta^2 - 32 r^2) \tilde{A}'(r)^3 + 32 \Theta^2 r^3 \tilde{A}'(r)^4 \tilde{A}''(r) \\
& + \tilde{A}'(r) \left(58 \Theta^2 r^2 \tilde{A}''(r)^2 + 64 \right) + 6 \Theta^2 r \tilde{A}'(r)^2 \left(r \tilde{A}^{(3)}(r) + 15 \tilde{A}''(r) \right) \\
& \left. \left. + 1024 \right] + 384, \tag{90}
\end{aligned}$$

$$\begin{aligned}
\chi = & \tilde{A}^{(3)}(r) \left[\Theta^2 \left(4 \tilde{A}'(r)^2 + r^2 \left(75 r^2 \tilde{A}^{(3)}(r)^2 - 10 \tilde{A}''(r)^2 + 21 r \tilde{A}^{(3)}(r) \tilde{A}''(r) \right) \right. \right. \\
& \left. \left. - r \tilde{A}'(r) \left(37 r \tilde{A}^{(3)}(r) + 8 \tilde{A}''(r) \right) \right) + 16 \right] \\
& + r \tilde{A}^{(4)}(r) \left[\Theta^2 \left(-4 \tilde{A}'(r)^2 + r^3 \tilde{A}^{(3)}(r) \left(40 r \tilde{A}^{(3)}(r) + 19 \tilde{A}''(r) \right) \right. \right. \\
& \left. \left. - r \tilde{A}'(r) \left(17 r \tilde{A}^{(3)}(r) + 10 \tilde{A}''(r) \right) \right) - 16 \right], \tag{91}
\end{aligned}$$

$$\begin{aligned}
\tilde{\chi} = & 5248 r \tilde{A}''(r) + 154 \Theta^4 r^2 \tilde{A}'(r)^7 \\
& + 16 \tilde{A}'(r) \left(9 \Theta^2 r^2 \tilde{A}''(r)^2 - 16 \right) \\
& + 8 \tilde{A}'(r)^5 \left(229 \Theta^4 r^4 \tilde{A}''(r)^2 + 3 \Theta^4 + 57 \Theta^2 r^2 \right) \\
& + \Theta^4 r^3 \tilde{A}'(r)^6 \left(256 r \tilde{A}^{(3)}(r) + 1655 \tilde{A}''(r) \right) \\
& + 4 \Theta^2 r \tilde{A}'(r)^2 \left(8 r \tilde{A}^{(3)}(r) + 5 \Theta^2 r^2 \tilde{A}''(r)^3 + 148 \tilde{A}''(r) \right) \\
& + 2 \tilde{A}'(r)^3 \left(5 \Theta^4 r^2 \tilde{A}''(r) \left(2 r \tilde{A}^{(3)}(r) + 25 \tilde{A}''(r) \right) + 80 \Theta^2 + 768 r^2 \right) \\
& + 4 \Theta^2 r \tilde{A}'(r)^4 \left((49 \Theta^2 + 416 r^2) \tilde{A}''(r) + \Theta^2 r \left(r \tilde{A}^{(4)}(r) + 13 \tilde{A}^{(3)}(r) \right) \right), \tag{92}
\end{aligned}$$

$$\begin{aligned}
\bar{\chi} = & 6 \Theta^4 r^2 \tilde{A}'(r)^7 \\
& - 16 r \left[-56 r \tilde{A}^{(3)}(r) + 5 \Theta^2 r^2 \tilde{A}''(r)^3 + 32 \tilde{A}''(r) \right] \\
& + 8 \Theta^2 r^2 \tilde{A}'(r)^5 \left[\Theta^2 r^2 \tilde{A}''(r) (276 r \tilde{A}^{(3)}(r) + 935 \tilde{A}''(r)) + 80 \right] \\
& - 2 \tilde{A}'(r) \left[\Theta^2 r^2 \tilde{A}''(r) (112 r \tilde{A}^{(3)}(r) + 25 \Theta^2 r^2 \tilde{A}''(r)^3 + 32 \tilde{A}''(r)) + 1120 \right] \\
& + \Theta^4 r^3 \tilde{A}'(r)^6 \left[2247 \tilde{A}''(r) + r (48 r \tilde{A}^{(4)}(r) + 929 \tilde{A}^{(3)}(r)) \right] \\
& + 2 r^2 \tilde{A}'(r)^3 \left[2 \Theta^4 r^2 \tilde{A}^{(3)}(r)^2 + (37 \Theta^4 + 5120 \Theta^2 r^2) \tilde{A}''(r)^2 \right. \\
& \quad \left. + \Theta^4 r (3 r \tilde{A}^{(4)}(r) + 38 \tilde{A}^{(3)}(r)) \tilde{A}''(r) + 1888 \right] \\
& + 4 \Theta^2 r \tilde{A}'(r)^4 \left[1130 \Theta^2 r^4 \tilde{A}''(r)^3 + 9 (\Theta^2 + 292 r^2) \tilde{A}''(r) \right. \\
& \quad \left. + r (2 \Theta^2 r \tilde{A}^{(4)}(r) + \tilde{A}^{(3)}(r) (11 \Theta^2 + 576 r^2)) \right] \\
& + 4 r \tilde{A}'(r)^2 \left[-15 \Theta^4 r^2 \tilde{A}''(r)^3 + 12 (3 \Theta^2 + 224 r^2) \tilde{A}''(r) \right. \\
& \quad \left. + 4 \Theta^2 r (r \tilde{A}^{(4)}(r) + 7 \tilde{A}^{(3)}(r)) - 23 \Theta^4 r^3 \tilde{A}^{(3)}(r) \tilde{A}''(r)^2 \right], \tag{93}
\end{aligned}$$

$$\begin{aligned}
\Xi = & 128 r \tilde{A}''(r) - 24 \Theta^4 \tilde{A}'(r)^5 \\
& + 4 r^2 \left[384 r \tilde{A}^{(4)}(r) + 944 \tilde{A}^{(3)}(r) + \Theta^2 (-r) \left(\Theta^2 r \tilde{A}^{(3)}(r)^3 - 190 \tilde{A}''(r)^3 \right. \right. \\
& \quad \left. \left. - 576 r \tilde{A}^{(3)}(r) \tilde{A}''(r)^2 + \Theta^2 \tilde{A}^{(3)}(r) (r \tilde{A}^{(4)}(r) + \tilde{A}^{(3)}(r)) \tilde{A}''(r) \right) \right] \\
& + \Theta^2 \tilde{A}'(r)^3 \left[\Theta^2 r^2 \left(-833 \tilde{A}''(r)^2 + 4 r^2 \tilde{A}^{(3)}(r) (32 r \tilde{A}^{(4)}(r) + 325 \tilde{A}^{(3)}(r)) \right. \right. \\
& \quad \left. \left. + r (741 r \tilde{A}^{(4)}(r) + 2422 \tilde{A}^{(3)}(r)) \tilde{A}''(r) \right) - 224 \right] \\
& + \tilde{A}'(r) \left[\Theta^2 r^2 \left(475 \Theta^2 r^2 \tilde{A}''(r)^4 + 848 \tilde{A}''(r)^2 + 4 \tilde{A}^{(3)}(r) \left(\Theta^2 r \tilde{A}^{(4)}(r) \right. \right. \right. \\
& \quad \left. \left. + \tilde{A}^{(3)}(r) (\Theta^2 + 832 r^2) \right) + 1760 \Theta^2 r^3 \tilde{A}^{(3)}(r) \tilde{A}''(r)^3 \right. \\
& \quad \left. + 16 r \left(152 r \tilde{A}^{(4)}(r) + 751 \tilde{A}^{(3)}(r) \right) \tilde{A}''(r) \right) - 512 \right] \\
& + 2 \Theta^2 r \tilde{A}'(r)^2 \left[335 \Theta^2 r^2 \tilde{A}''(r)^3 + 4 r (115 r \tilde{A}^{(4)}(r) + 89 \tilde{A}^{(3)}(r)) \right. \\
& \quad \left. + 12 \left(114 \Theta^2 r^4 \tilde{A}^{(3)}(r)^2 - 79 \right) \tilde{A}''(r) + 2 \Theta^2 r^3 \left(230 r \tilde{A}^{(4)}(r) \right. \right. \\
& \quad \left. \left. + 1849 \tilde{A}^{(3)}(r) \right) \tilde{A}''(r)^2 \right] \\
& + 2 \Theta^4 r \tilde{A}'(r)^4 \left[r \left(50 r \tilde{A}^{(4)}(r) - 89 \tilde{A}^{(3)}(r) \right) - 249 \tilde{A}''(r) \right], \tag{94}
\end{aligned}$$

$$\begin{aligned}
\tilde{\Xi} = & \Theta^2 \left[8 \Theta^2 \tilde{A}'(r)^4 + r^2 \left(16 r^2 \tilde{A}^{(3)}(r) (32 r \tilde{A}^{(4)}(r) + 67 \tilde{A}^{(3)}(r)) \right. \right. \\
& + 8 \left(23 \Theta^2 r^4 \tilde{A}^{(3)}(r)^2 - 10 \right) \tilde{A}''(r)^2 + 95 \Theta^2 r^3 \tilde{A}^{(3)}(r) \tilde{A}''(r)^3 + 8 r \left(19 r \tilde{A}^{(4)}(r) + 23 \tilde{A}^{(3)}(r) \right) \tilde{A}''(r) \left. \right) \\
& + \tilde{A}'(r)^2 \left[\Theta^2 r^2 \left(-60 \tilde{A}''(r)^2 + 3 r^2 \tilde{A}^{(3)}(r) (49 r \tilde{A}^{(4)}(r) + 51 \tilde{A}^{(3)}(r)) \right. \right. \\
& \quad \left. \left. - r (47 r \tilde{A}^{(4)}(r) + 344 \tilde{A}^{(3)}(r)) \tilde{A}''(r) \right) + 64 \right] \\
& + r \tilde{A}'(r) \left[-50 \Theta^2 r^2 \tilde{A}''(r)^3 + 8 r \left(-17 r \tilde{A}^{(4)}(r) + 32 \Theta^2 r^4 \tilde{A}^{(3)}(r)^3 - 45 \tilde{A}^{(3)}(r) \right) \right. \\
& \quad + \left(3 \Theta^2 r^4 \tilde{A}^{(3)}(r) (128 r \tilde{A}^{(4)}(r) + 429 \tilde{A}^{(3)}(r)) + 16 \right) \tilde{A}''(r) \\
& \quad \left. + \Theta^2 r^3 (95 r \tilde{A}^{(4)}(r) + 201 \tilde{A}^{(3)}(r)) \tilde{A}''(r)^2 \right] \\
& - 2 \Theta^2 r \tilde{A}'(r)^3 \left[r (19 r \tilde{A}^{(4)}(r) + 45 \tilde{A}^{(3)}(r)) - 2 \tilde{A}''(r) \right] \left. \right] + 128,
\end{aligned} \tag{95}$$

and

$$\begin{aligned}
\bar{\Xi} = & r^2 \left[-252 \Theta^4 \tilde{A}'(r)^6 - 4 r \left(16 \Theta^2 r \tilde{A}^{(3)}(r)^2 - 1664 r \tilde{A}''(r)^2 \right. \right. \\
& \quad \left. \left. + 5 \Theta^4 r^2 \tilde{A}^{(3)}(r) \tilde{A}''(r)^3 + 8 \Theta^2 (r \tilde{A}^{(4)}(r) + \tilde{A}^{(3)}(r)) \tilde{A}''(r) \right) \right. \\
& + \Theta^2 \tilde{A}'(r)^4 \left[\Theta^2 r^2 \left(784 r^2 \tilde{A}^{(3)}(r)^2 + 7833 \tilde{A}''(r)^2 \right. \right. \\
& \quad \left. \left. + 2 r (304 r \tilde{A}^{(4)}(r) + 4671 \tilde{A}^{(3)}(r)) \tilde{A}''(r) \right) - 1520 \right] \\
& + 4 \tilde{A}'(r)^2 \left[\Theta^2 r \left(1050 \Theta^2 r^3 \tilde{A}''(r)^4 + 8302 r \tilde{A}''(r)^2 \right. \right. \\
& \quad + \Theta^2 r \tilde{A}^{(3)}(r) (r \tilde{A}^{(4)}(r) + 5 \tilde{A}^{(3)}(r)) \\
& \quad \left. \left. + (3 \Theta^2 r \tilde{A}^{(4)}(r) + 4 \tilde{A}^{(3)}(r) (3 \Theta^2 + 1216 r^2)) \tilde{A}''(r) \right) - 512 \right] \tag{96} \\
& + 4 \tilde{A}'(r) \left[8 \Theta^2 r \tilde{A}^{(4)}(r) + 8 \tilde{A}^{(3)}(r) (\Theta^2 + 384 r^2) \right. \\
& \quad + 2720 \Theta^2 r^3 \tilde{A}''(r)^3 + 5 r \left(944 - 3 \Theta^4 r^2 \tilde{A}^{(3)}(r)^2 \right) \tilde{A}''(r) \\
& \quad \left. + \Theta^4 (-r^2) \left(5 r \tilde{A}^{(4)}(r) + 9 \tilde{A}^{(3)}(r) \right) \tilde{A}''(r)^2 \right] \\
& + 2 \Theta^2 \tilde{A}'(r)^3 \left[4 r \tilde{A}^{(4)}(r) (\Theta^2 + 96 r^2) + 4 \tilde{A}^{(3)}(r) (\Theta^2 + 1130 r^2) \right. \\
& \quad \left. + 7105 \Theta^2 r^3 \tilde{A}''(r)^3 + 3900 r \tilde{A}''(r) + 4560 \Theta^2 r^4 \tilde{A}^{(3)}(r) \tilde{A}''(r)^2 \right] \\
& + 2 \Theta^4 r \tilde{A}'(r)^5 \left[65 \tilde{A}''(r) + r (115 r \tilde{A}^{(4)}(r) + 699 \tilde{A}^{(3)}(r)) \right] \left. \right] - 128.
\end{aligned}$$

In Fig. 12, the effective potentials for Schwarzschild and Hayward black holes are shown. Visibly, the Hayward spacetime, in the non-commutative framework has a higher effective

potential than the Schwarzschild case. To explore the effect of Hayward parameter value l on the effective potential, we illustrate the effective potential, for specific values of mass M , ℓ , and m in Fig.13, left panel displays the effective potential for varying values of Θ when $\ell = 1$ and $m = \pm 1$, while panels middle and right panels correspond to $\ell = 2$ with $m = \pm 1$ and ± 2 , respectively.

Although the influence of the NC parameter on the system is subtle on the potential, as Θ increases, the peak value of the potential also rises, suggesting that the effective potential forms a stronger barrier against the propagation of the field.

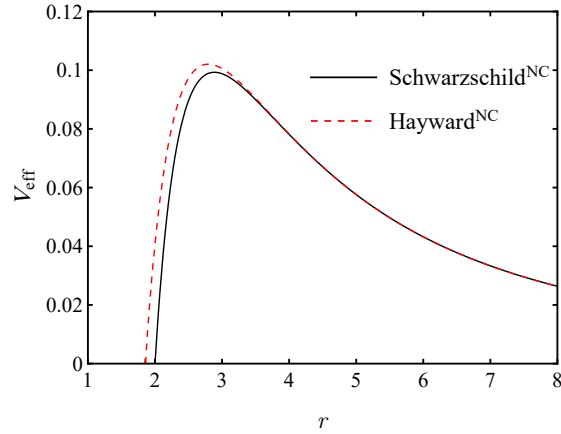


FIG. 12: Effective potential for scalar field with $M = 1$, $\ell = 1(m = \pm 1)$ for both Schwarzschild case and Hayward spacetime with $l = 0.1$ in non-commutative framework with parameter $\Theta = 0.5$

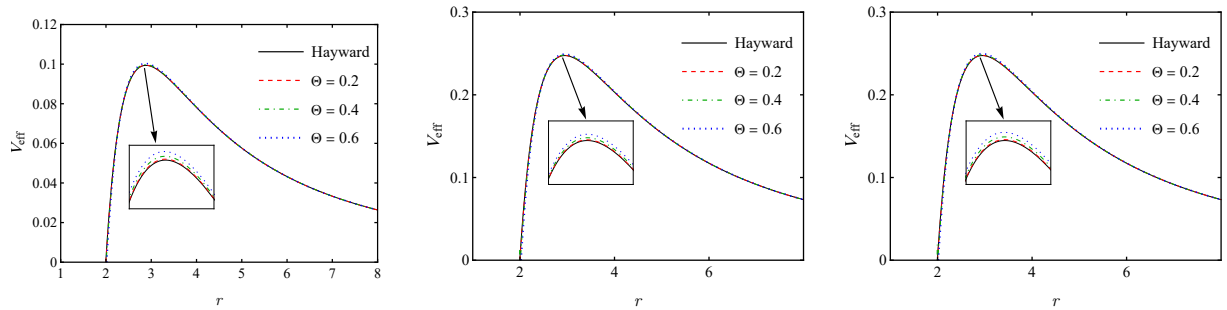


FIG. 13: Effective potential for scalar field with $M = 1$, $l = 0.1$ in left panel (a) for $\ell = 1(m = \pm 1)$, in middle panel (b) for $\ell = 2 (m = \pm 1)$ and in the right panel (c) for $\ell = 2 (m = \pm 2)$ concerning different values of Θ .

VI. QUASINORMAL MODES

Black holes respond to perturbations through damped oscillations known as quasinormal modes (QNMs), which are characterized by complex frequencies. The real component determines the oscillation rate, while the imaginary part governs the damping behavior. These modes reflect how disturbances behave near the event horizon and reveal properties of the surrounding geometry. Within the setting of non-commutative geometry, QNMs provide a way to examine how the non-commutative parameter affects scalar field (for instance) behavior and its interaction with the effective potential.

To extract the QNM frequencies, one must solve the wave equation under boundary conditions that restrict solutions to purely ingoing waves at the event horizon and outgoing waves at infinity. Given the intricate nature of the equation, exact solutions are rarely achievable. The importance of QNMs in describing the temporal and spatial features of perturbations has led to a variety of approximation methods, both analytical and numerical [159, 187–190]. In what follows, the WKB method is applied to assess how the non-commutative parameter alters the quasinormal spectrum.

The WKB approximation is used to determine QNMs through the following relation

$$\frac{i(\omega_n^2 - V_0)}{\sqrt{-2V_0''}} + \sum_{j=2}^3 \Omega_j = n + \frac{1}{2}, \quad (97)$$

where V_0 represents the effective potential at its maximum, and V_0'' is its second derivative with respect to r^* . The terms Ω_j account for the WKB corrections [149].

Applying the above-mentioned method, QNMs are explored and presented in Tab. II. The results show that the real and imaginary parts of QNMs delicately depend on Θ and ℓ , therefore for better analysis, a normalized deviation is defined to quantify the difference between the QNMs of the non-commutative black hole and the standard Hayward black hole as

$$\delta = \frac{\omega^{\text{NC}}}{\omega^{\text{H}}} - 1. \quad (98)$$

The above deviation has been investigated for both real and imaginary terms of QNMs. The results are summarized in Fig. 14-18 .

The analysis considers two sets of multipole numbers, $\ell = 1, 2$, along with their associated monopoles, satisfying $n \leq \ell$, for $M = 1$. Notably, when $\Theta = 0$, the solution reduces to the

TABLE II: Quasinormal modes of Hayward black hole in non-commutative framework, calculated by WKB method, for $M = 1$.

		$\Theta = 0.000$	$\Theta = 0.025$	$\Theta = 0.050$	$\Theta = 0.075$	$\Theta = 0.100$	
$l = 1,$	$n = 0$	0.29133-0.09782 <i>i</i>	0.29133-0.09782 <i>i</i>	0.29134-0.09784 <i>i</i>	0.29136-0.09786 <i>i</i>	0.29139-0.09789 <i>i</i>	
	$m = \pm 1$	$n = 1$	0.26246-0.30686 <i>i</i>	0.26247-0.30687 <i>i</i>	0.26249-0.30690 <i>i</i>	0.26253-0.30696 <i>i</i>	0.26259-0.30703 <i>i</i>
$l = 2$	$n = 0$	0.48357-0.09665 <i>i</i>	0.48358-0.09665 <i>i</i>	0.48359-0.09667 <i>i</i>	0.48361-0.09669 <i>i</i>	0.48363-0.09672 <i>i</i>	
	$m = \pm 2$	$n = 1$	0.46362-0.29531 <i>i</i>	0.46363-0.29533 <i>i</i>	0.46365-0.29537 <i>i</i>	0.46368-0.29544 <i>i</i>	0.46373-0.29553 <i>i</i>
		$n = 2$	0.43217-0.50257 <i>i</i>	0.43218-0.50259 <i>i</i>	0.43222-0.50266 <i>i</i>	0.43228-0.50276 <i>i</i>	0.43236-0.50291 <i>i</i>
$l = 2$	$n = 0$	0.48357-0.09665 <i>i</i>	0.48358-0.09665 <i>i</i>	0.48359-0.09666 <i>i</i>	0.48361-0.09668 <i>i</i>	0.48364-0.09671 <i>i</i>	
	$m = \pm 1$	$n = 1$	0.46362-0.29531 <i>i</i>	0.46363-0.29533 <i>i</i>	0.46365-0.29536 <i>i</i>	0.46368-0.29541 <i>i</i>	0.46372-0.29549 <i>i</i>
		$n = 2$	0.43217-0.50257 <i>i</i>	0.43218-0.50259 <i>i</i>	0.43221-0.50264 <i>i</i>	0.43226-0.50273 <i>i</i>	0.43233-0.50285 <i>i</i>

standard Hayward black hole, as expected.

The results show that δ in both real and absolute imaginary values increases with Θ .

For instance, the deviation in the real part of the QNMs for $\ell = 1$, $m = \pm 1$ and $n = 0$ (Fig. 14) shows a gradual increase with Θ , implying a higher propagation frequency. Moreover, the deviation in the real part is more pronounced for lower values of l . Although the absolute value of the imaginary component of the frequency exhibits a similar trend, suggesting that larger values of Θ correspond to shorter damping timescales for the black hole. These behaviors are consistent across all modes in Fig. 15–16 and the behavior of both real and imaginary terms, are similar for $\ell = 1(m = \pm 1)$, $\ell = 2(m = \pm 2)$ and $\ell = 2(m = \pm 1)$.

Furthermore, the deviation for various related monopoles for $n \leq \ell$, are represented in Fig.17–18, respectively. Both real and imaginary parts of the QNMs's, have similar behaviour as their corresponding multipole number ℓ . The real part, as a propagation frequency, goes higher with NC parameter, but the effect is more pronounced for the overtones with higher numbers. The imaginary part, governing the damping rate, also increases with Θ , however, it is more significant for the lower overtone. This suggests that the damping rate is more sensitive to non-commutative effects for the fundamental mode.

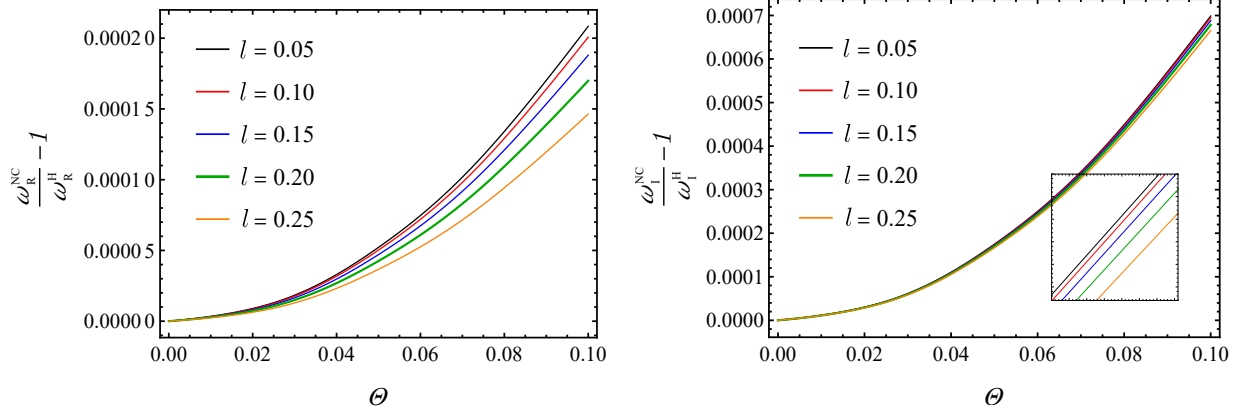


FIG. 14: Real term of QNMs obtained by WKB method for $M = 1$ and $l = 0.1$ with respect to variation of Θ when $\ell = 1$ and from left to right with overtones $n = 0$ and 1 , respectively.

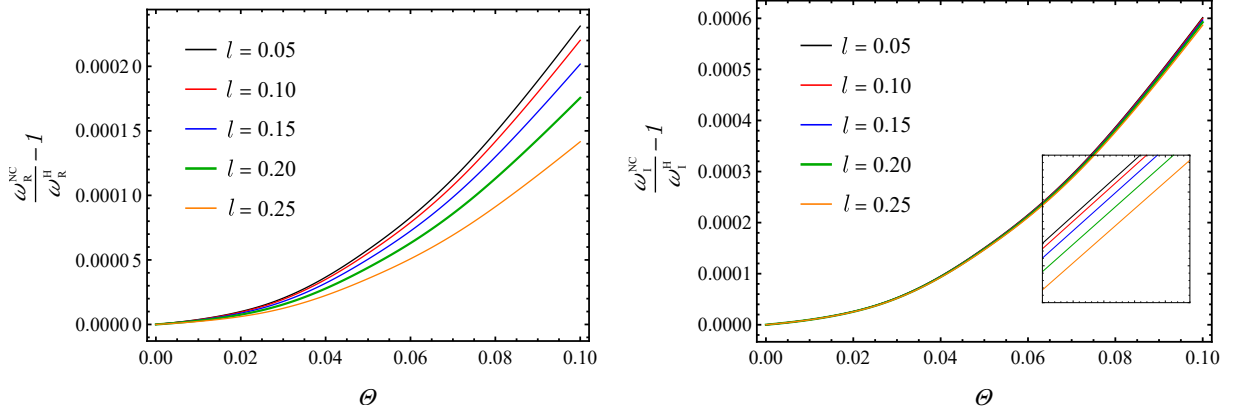


FIG. 15: Imaginary term of QNMs obtained by WKB method for $M = 1$ and $l = 0.1$ with respect to variation of Θ when $\ell = 1$ and from left to right with overtones $n = 0$ and 1 , respectively.

VII. TIME-DOMAIN SOLUTION

Examining scalar perturbations within the time domain is fundamental to understanding the role of the quasinormal spectrum in time-dependent scattering processes. Given the complexity of the effective potential, a precise numerical approach is necessary to properly capture its behavior. To address this, the characteristic integration method developed by Gundlach et al. [191] is applied, providing a reliable tool for studying quasinormal modes in dynamical scattering and their implications for black hole physics.

The approach outlined in Refs. [191–197] employs light-cone coordinates, defined as

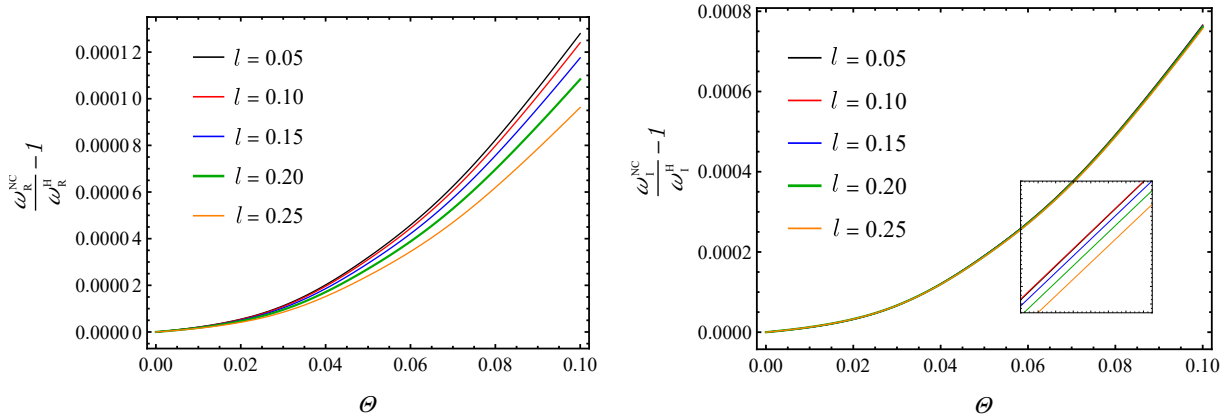


FIG. 16: QNMs obtained by WKB method for $M = 1$ and $l = 0.1$ with respect to variation of Θ when $\ell = 2$ and from left to right with overtones $n = 0, 1$ and 2 , respectively.

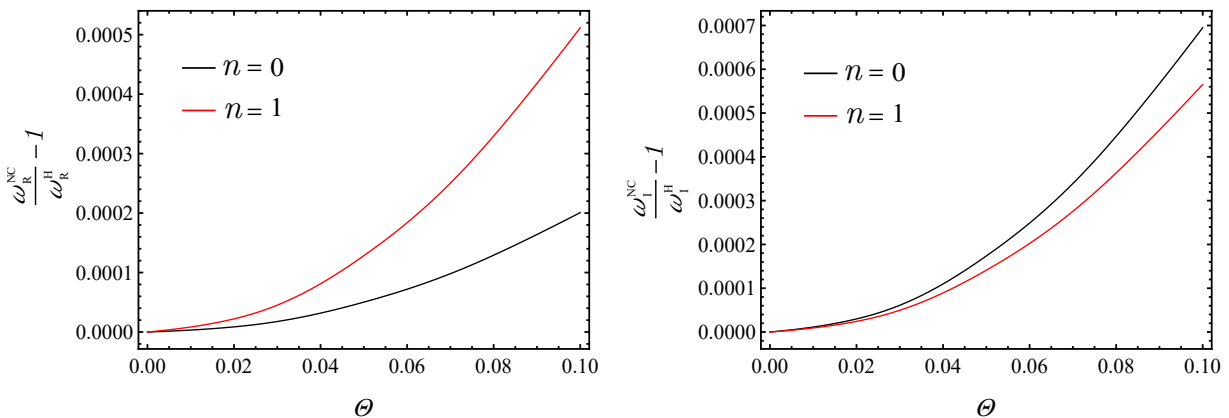


FIG. 17: QNMs obtained by WKB method for $M = 1$ and $l = 0.1$ with respect to variation of Θ when $\ell = 2$ and from left to right with overtones $n = 0, 1$ and 2 , respectively.

$u = t - r^*$ and $v = t + r^*$. Utilizing these coordinates streamlines the wave equation, facilitating a more effective analysis. Within this formulation, the wave equation can be reformulated as

$$\left(4 \frac{\partial^2}{\partial u \partial v} + V(u, v)\right) \tilde{\psi}(u, v) = 0. \quad (99)$$

An effective numerical strategy for solving the equation involves a discretization scheme that combines the finite-difference method with other computational techniques to improve accuracy and stability

$$\tilde{\psi}(N) = -\tilde{\psi}(S) + \tilde{\psi}(W) + \tilde{\psi}(E) - \frac{h^2}{8} V(S) [\tilde{\psi}(W) + \tilde{\psi}(E)] + \mathcal{O}(h^4). \quad (100)$$

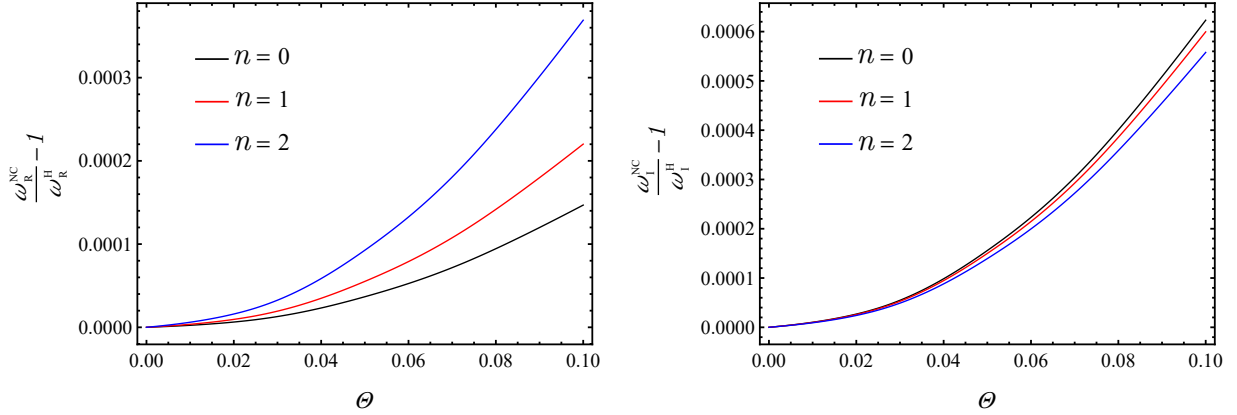


FIG. 18: QNMs obtained by WKB method for $M = 1$ and $l = 0.1$ with respect to variation of Θ when $\ell = 2$ and from left to right with overtones $n = 0, 1$ and 2 , respectively.

The coordinate points are designated as $S = (u, v)$, $W = (u + h, v)$, $E = (u, v + h)$, and $N = (u + h, v + h)$, where h represents the grid spacing parameter. The null surfaces defined by $u = u_0$ and $v = v_0$ play a fundamental role in establishing reference points for initializing the system. In this study, the initial conditions along the null surface $u = u_0$ are described by a Gaussian profile centered at $v = v_c$ with a width parameter σ

$$\tilde{\psi}(u = u_0, v) = Ae^{-(v-v_0)^2/2\sigma^2}, \quad \tilde{\psi}(u, v_0) = \tilde{\psi}_0. \quad (101)$$

The initial condition is defined as $\tilde{\psi}(u, v_0) = \tilde{\psi}_0$ at $v = v_0$, with $\tilde{\psi}_0$ set to zero for convenience, as this does not affect generality. The integration process advances along surfaces of constant u while incrementing v , following the specified null data. To simplify the analysis, a scalar test field is considered with $M = 1$. The initial configuration adopts a Gaussian profile centered at $v_0 = 0$, characterized by a width of $\sigma = 1$ and centered at $\tilde{\psi}_0 = 0$. The computational region spans $u \in [0, 1000]$ and $v \in [0, 1000]$, with the grid factors $h = 0.1$.

In Figs. 19 (for $\ell = 1$ and $m = \pm 1$) and 22 (for $\ell = 2$ and $m = \pm 1$), the function $\tilde{\psi}$ is plotted over time t for different values of Θ , namely 0.1, 0.2, and 0.99, while keeping $l = 0.1$ fixed. These plots reveal that as time progresses, the waveform tends to stabilize at more attainable values. Additionally, Figs. 20 (for $\ell = 1$ and $m = \pm 1$) and 23 (for $\ell = 2$ and $m = \pm 1$) illustrate the \ln absolute values of $\tilde{\psi}$ as a function of time. The straight-line segments in these plots indicate exponential decay, reflecting the typical profile of a quasinormal mode, where oscillations diminish exponentially over time. Finally, Figs. 21

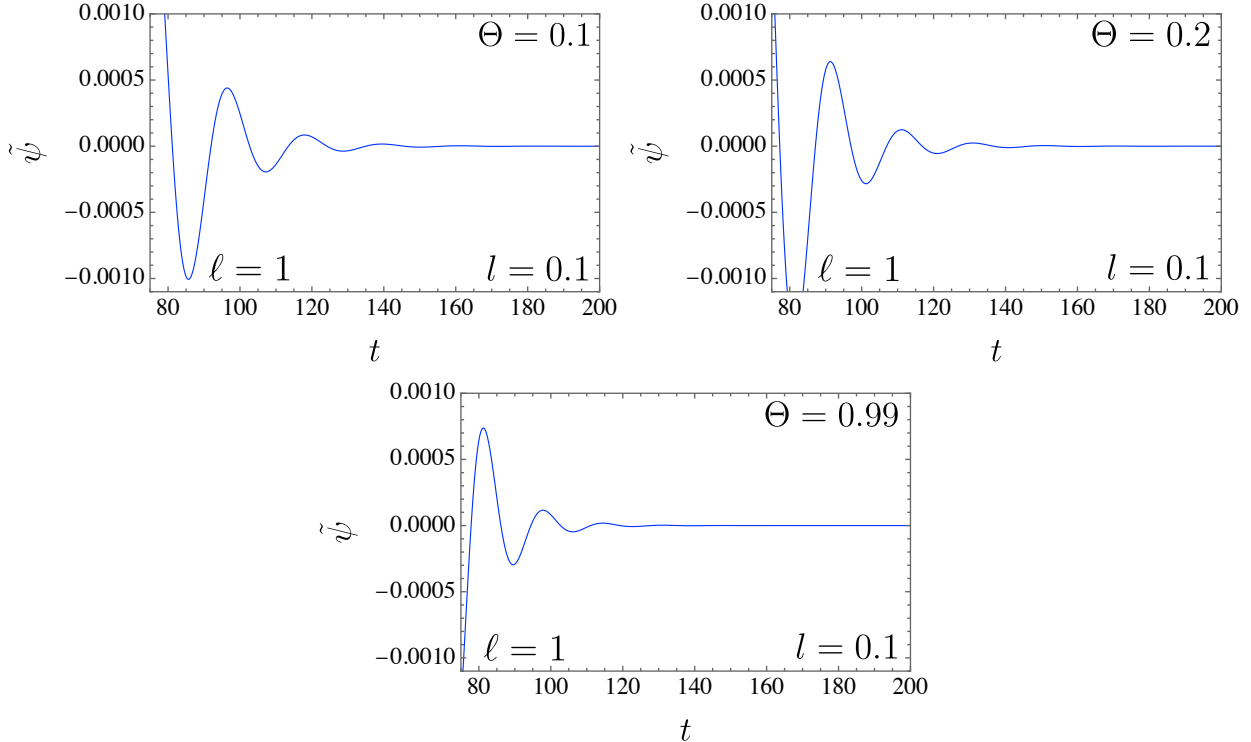


FIG. 19: The function $\tilde{\psi}$ (for $\ell = 1$ and $m = \pm 1$) is depicted as a function of time t for different values of Θ , while keeping $l = 0.1$ fixed.

(for $\ell = 1$ and $m = \pm 1$) and 24 (for $\ell = 2$ and $m = \pm 1$) present a log–log plot of the \ln absolute value of $\tilde{\psi}$ against time. Overall, the inclusion of the non–commutative parameter in the black hole model results in a more strongly damped configuration for gravitational waves. Such a conclusion is corroborated in the quasinormal section as well (see Tab. II).

VIII. NULL GEODESICS

This part of the study is dedicated to examining the geodesic structure. As discussed earlier, determining the Christoffel symbols plays a crucial role in this analysis. Therefore, we begin by expressing

$$\frac{d^2 x^\mu}{d\tau^2} + \Gamma^\mu_{\alpha\beta} \frac{dx^\alpha}{d\tau} \frac{dx^\beta}{d\tau} = 0. \quad (102)$$

In this context, τ represents a general affine parameter. This formulation leads to a system of four coupled differential equations, each describing motion along a specific coordinate direction. Due to their considerable length, spanning approximately 20 pages, their explicit expressions are omitted in this paper. However, Fig. 25 provides a visualization of the

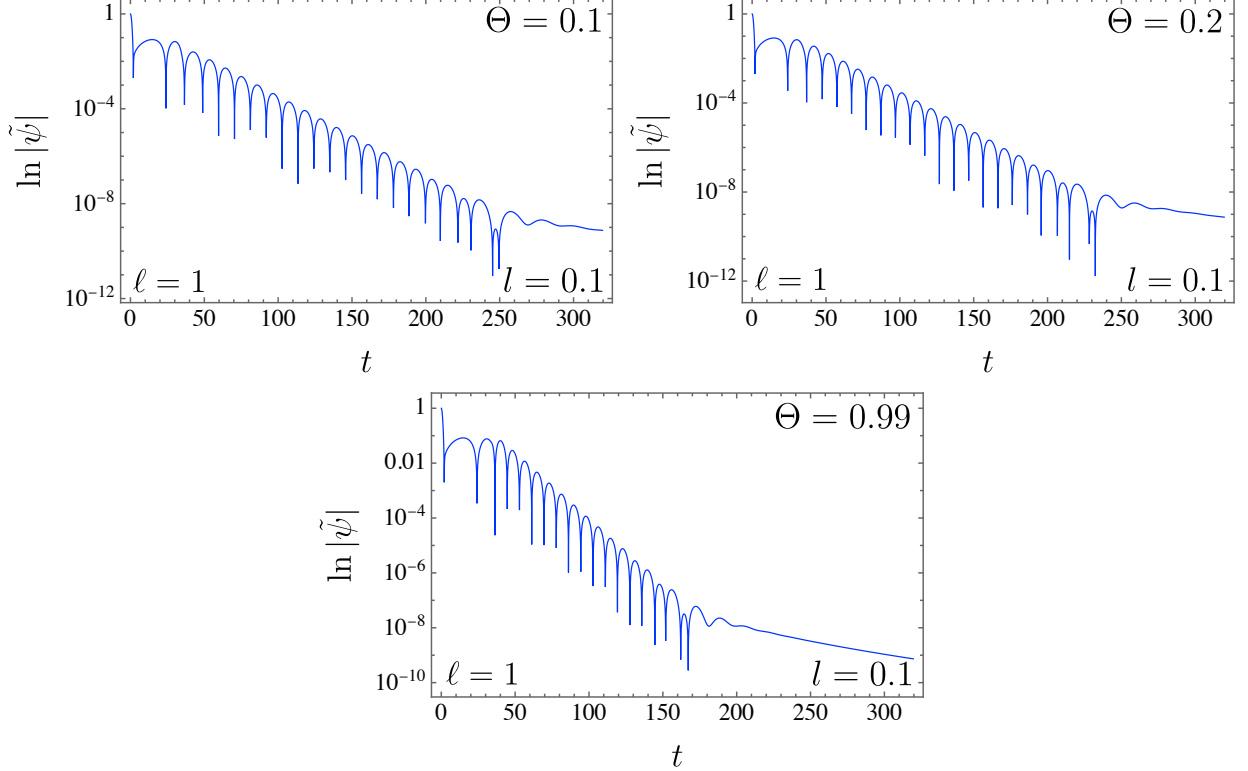


FIG. 20: The absolute value of $\ln|\tilde{\psi}|$ (for $\ell = 1$ and $m = \pm 1$) is depicted as a function of time t for different values of Θ , while keeping $l = 0.1$ fixed.

light trajectory for various values of the parameter Θ . The chosen values range from 0.01 to 0.99 in increments, but for clarity and visual presentation, only six representative cases are displayed in the figure labels. This result implies that the gravitational lensing impact weakens slightly with a stronger non-commutativity effect in Hayward black hole, allowing light rays to escape more easily.

A. Photonic radius and shadows

A key area of research in black hole physics is the study of the shadows cast [11, 198–200]. Interest in these phenomena has increased significantly, especially after the groundbreaking observation of the *SgrA** and *M87** black holes shadow by the Event Horizon Telescope (EHT) [201–203]. To investigate the photonic and the shadow radius, we begin with a general diagonal metric given by

$$g_{\mu\nu}^{(\Theta,l)} dx^\mu dx^\nu = g_{tt}^{(\Theta,l)} dt^2 + g_{rr}^{(\Theta,l)} dr^2 + g_{\theta\theta}^{(\Theta,l)} d\theta^2 + g_{\varphi\varphi}^{(\Theta,l)} d\varphi^2. \quad (103)$$

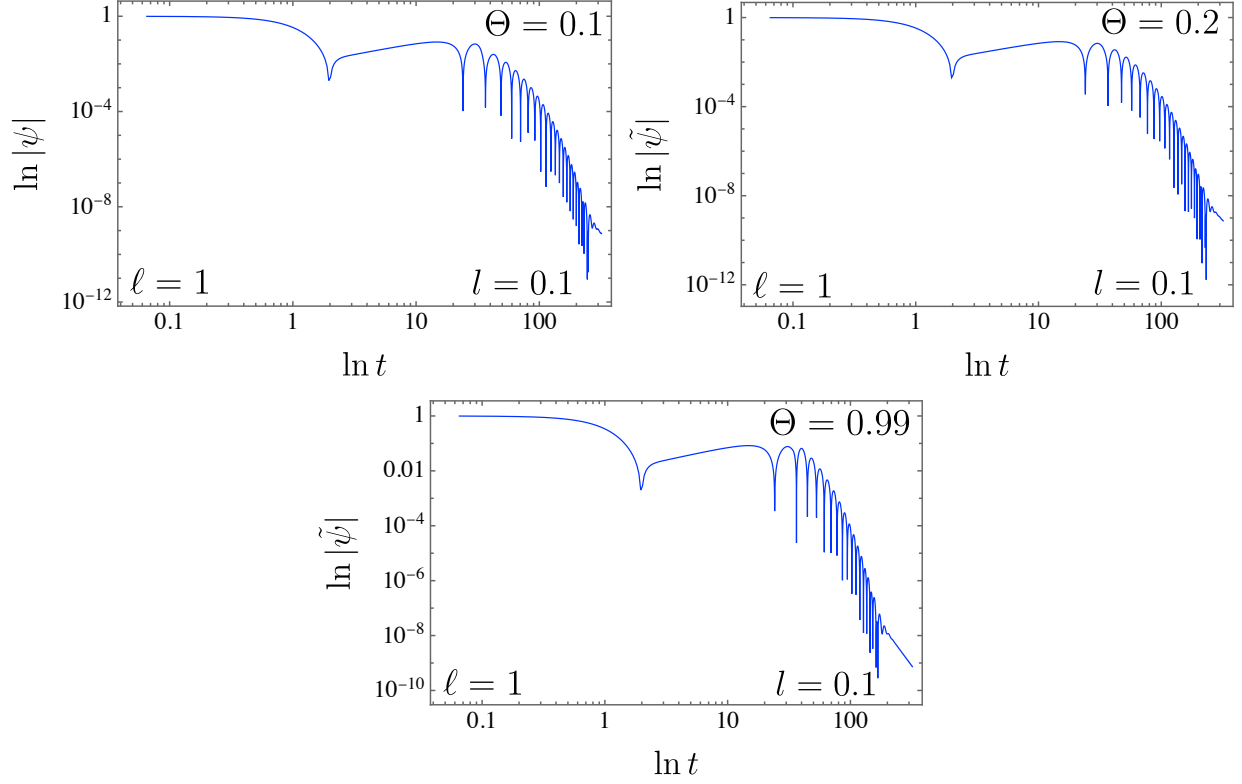


FIG. 21: The absolute value of $\ln |\tilde{\psi}|$ (for $\ell = 1$ and $m = \pm 1$) is depicted as a function of $\ln t$ for different values of Θ , while keeping $l = 0.1$ fixed.

Using this metric, the corresponding Lagrangian is given by

$$\mathcal{L} = \frac{1}{2} \left[g_{tt}^{(\Theta, l)} \dot{t}^2 + g_{rr}^{(\Theta, l)} \dot{r}^2 + g_{\theta\theta}^{(\Theta, l)} \dot{\theta}^2 + g_{\varphi\varphi}^{(\Theta, l)} \dot{\varphi}^2 \right]. \quad (104)$$

For simplicity, we assume that geodesics lie in the equatorial plane ($\theta = \frac{\pi}{2}$). Also, we consider two conserved quantities, the energy E and angular momentum L as

$$E = g_{tt}^{(\Theta, l)} \dot{t} \quad \text{and} \quad L = g_{\varphi\varphi}^{(\Theta, l)} \dot{\varphi}. \quad (105)$$

which are related to the impact parameter as $b = \frac{L}{E}$. Since light follows null geodesics as $\mathcal{L} = 0$, the following condition must hold

$$g_{tt}^{(\Theta, l)} \dot{t}^2 + g_{rr}^{(\Theta, l)} \dot{r}^2 + g_{\varphi\varphi}^{(\Theta, l)} \dot{\varphi}^2 = 0. \quad (106)$$

Substituting Eq. (105) into Eq. (106), the radial equation governing the motion of photons in the equatorial plane can be expressed as

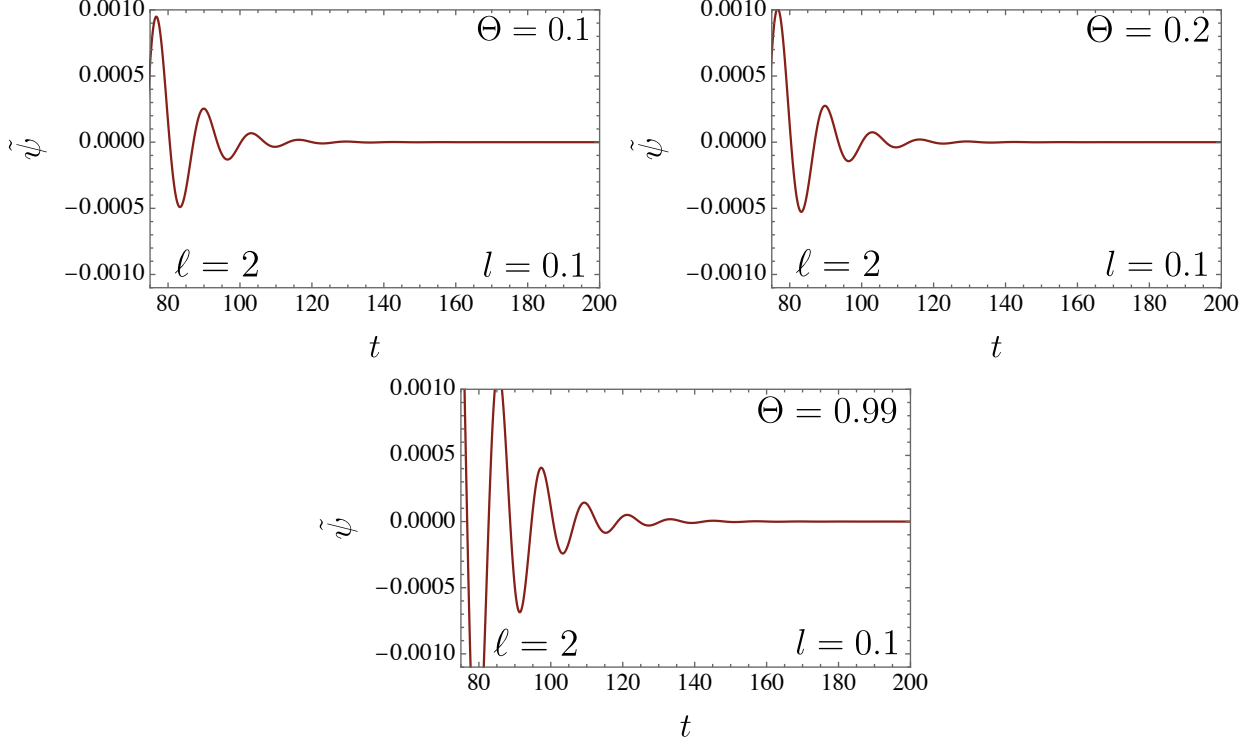


FIG. 22: The function $\tilde{\psi}$ (for $\ell = 2$ and $m = \pm 1$) is depicted as a function of time t for different values of Θ , while keeping $l = 0.1$ fixed.

$$\frac{\dot{r}^2}{\dot{\varphi}^2} = \frac{g_{tt}^{(\Theta,l)}}{g_{rr}^{(\Theta,l)}} \left(\frac{g_{\varphi\varphi}^{(\Theta,l)}}{g_{tt}^{(\Theta,l)}} \frac{E^2}{L^2} - 1 \right). \quad (107)$$

By defining the right-hand side of Eq. (107) as the effective potential \tilde{V}_{eff} , the equation governing the trajectory simplifies to

$$\left(\frac{dr}{d\varphi} \right)^2 + \tilde{V}_{eff} = 0. \quad (108)$$

The conditions for photic orbits are determined by solving

$$\frac{d\tilde{V}_{eff}}{dr} = 0. \quad (109)$$

Solving these equations allows us to determine the radius of the photon sphere r_{ph} . Tab. III systematically examines the photon sphere radius r_{ph} for a black hole with mass $M = 1$, evaluated across different values of the NC and the Hayward parameters. Two distinct patterns emerge from the data. First, when l is held constant, an increase in non-commutativity impact correlates with a decrease in r_{ph} . Second, for a fixed Θ , raising

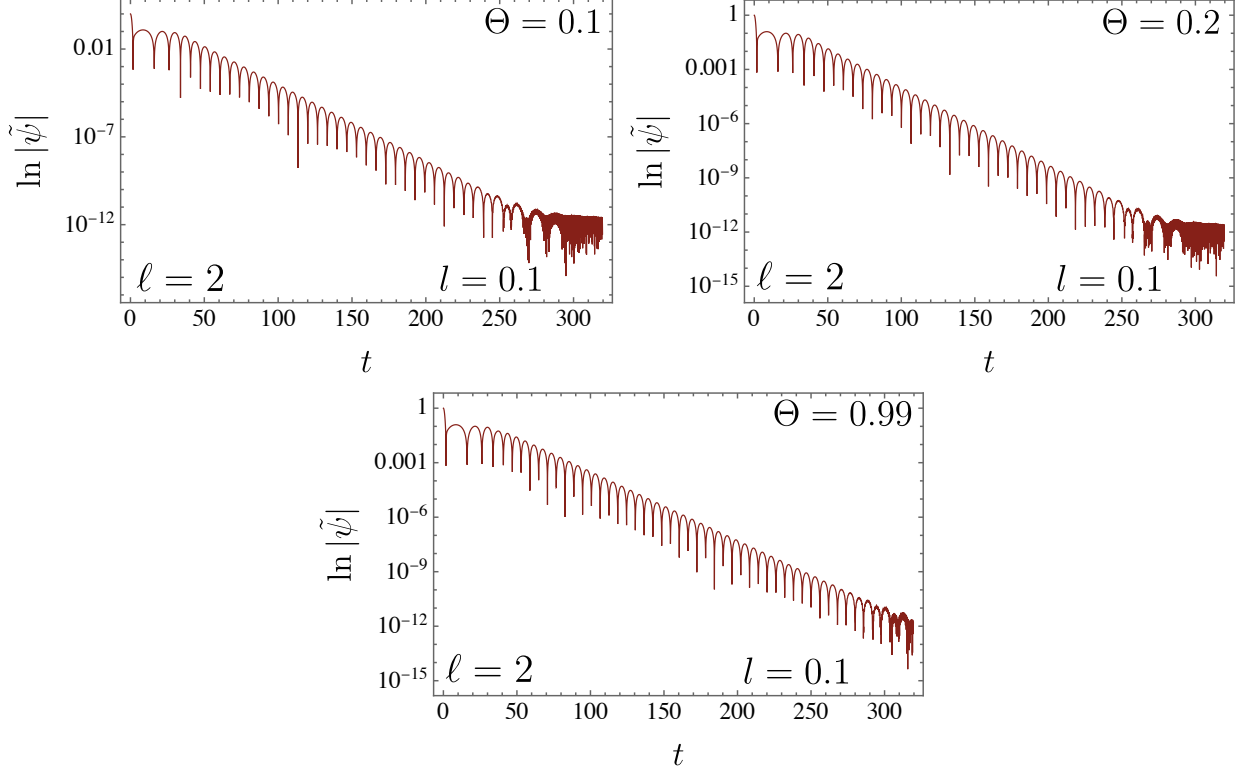


FIG. 23: The absolute value of $\ln |\tilde{\psi}|$ (for $\ell = 2$ and $m = \pm 1$) is depicted as a function of time t for different values of Θ , while keeping $l = 0.1$ fixed.

TABLE III: Photonic radius of a Hayward black hole with $M = 1$ and $l = 0.02$ to 0.10 in non-commutativity framework with variation of Θ values.

	$l = 0.02$	$l = 0.04$	$l = 0.06$	$l = 0.08$	$l = 0.10$
$\Theta = 0.0$	2.99982	2.99929	2.99840	2.99715	2.99554
$\Theta = 0.2$	2.99927	2.99874	2.99786	2.99662	2.99503
$\Theta = 0.4$	2.99761	2.99709	2.99624	2.99503	2.99348
$\Theta = 0.6$	2.99484	2.99435	2.99353	2.99238	2.99091
$\Theta = 0.8$	2.99095	2.99050	2.98973	2.98867	2.98729
$\Theta = 1.0$	2.98595	2.98553	2.98484	2.98386	2.98261

the Hayward parameter l similarly results in a reduction of photonic radius. These trends highlight the significant influence of both Θ and l on the spacetime structure, directly impacting the photon sphere's dimensions. The observed reduction in r_{ph} with increasing Θ and l emphasizes the interconnected role of these parameters in the shadow cast radius.

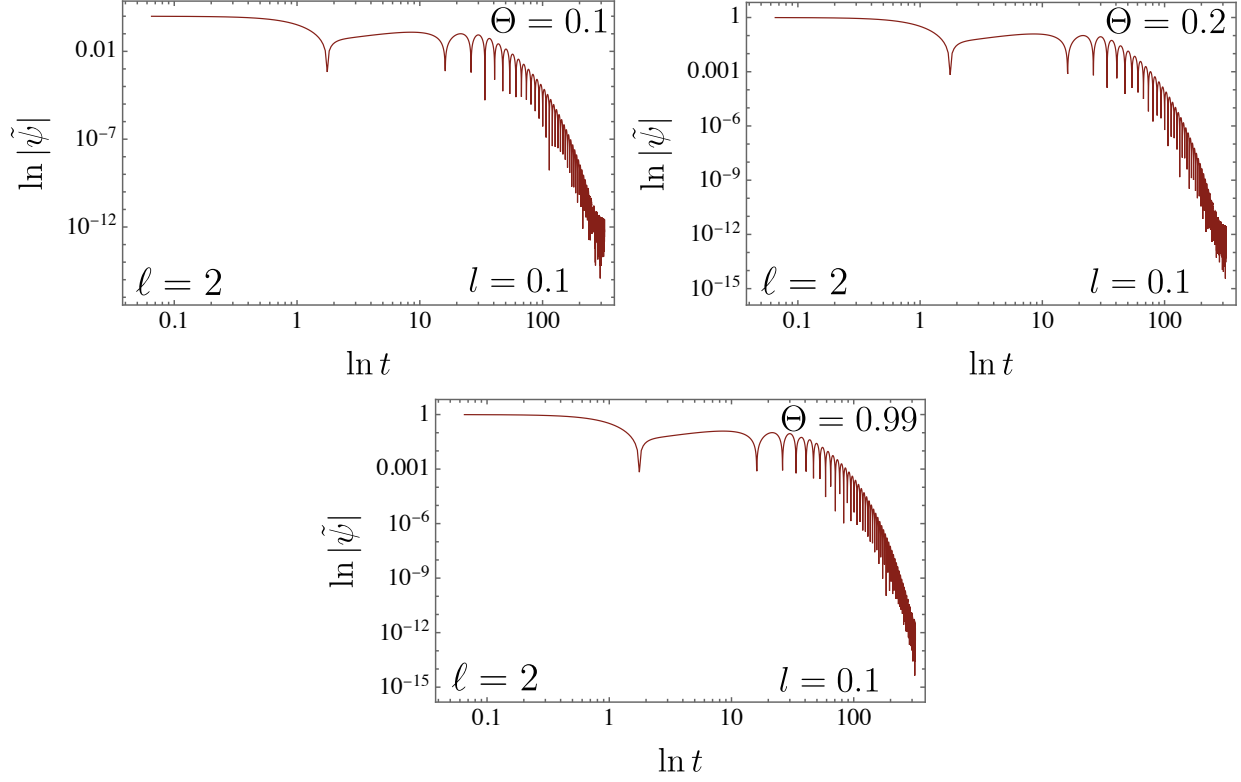


FIG. 24: The absolute value of $\ln |\tilde{\psi}|$ (for $\ell = 2$ and $m = \pm 1$) is depicted as a function of $\ln t$ for different values of Θ , while keeping $l = 0.1$ fixed.

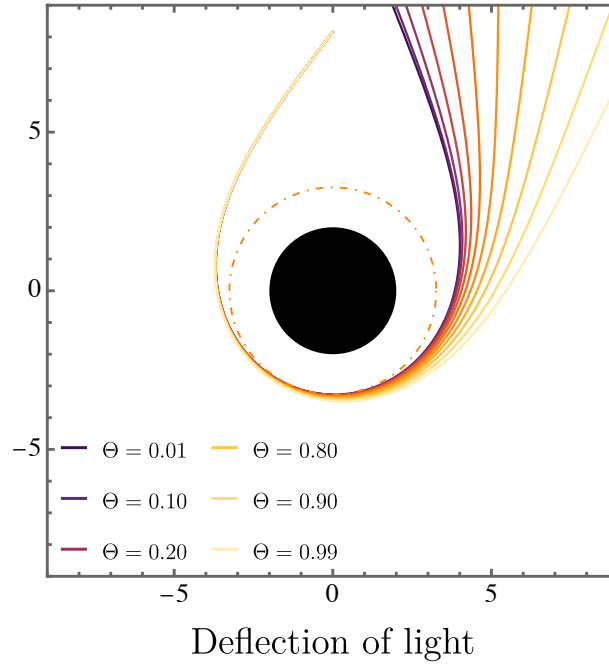


FIG. 25: The deflection of light as the non-commutative parameter Θ increases.

Following the methodologies outlined in Refs. [204–206], the expression for the black hole shadow in a spherically symmetric spacetime read the following equation

$$R_{sh} = \sqrt{\frac{g_{\varphi\varphi}^{(\Theta,l)}(r_{ph})}{g_{tt}^{(\Theta,l)}(r_{ph})}} = \sqrt{\frac{r_{ph}^2(2l^2M + r_{ph}^3)}{2l^2M - 2Mr_{ph}^2 + r_{ph}^3}} - \frac{\Theta^2}{8(2l^2M + r_{ph}^3)^4(2l^2M - 2Mr_{ph}^2 + r_{ph}^3)} \left(M \sqrt{\frac{r_{ph}^2(2l^2M + r_{ph}^3)}{2l^2M - 2Mr_{ph}^2 + r_{ph}^3}} (32l^8M^4 + 520l^6M^3r_{ph}^3 - 768l^4M^3r_{ph}^5 - 132l^4M^2r_{ph}^6 + 456l^2M^2r_{ph}^8 - 182l^2Mr_{ph}^9 - 12Mr_{ph}^{11} + 5r_{ph}^{12}) \right). \quad (110)$$

For better visualization, we display an analysis of the shadows of our black hole for a range of Θ and l values in Fig. 26.

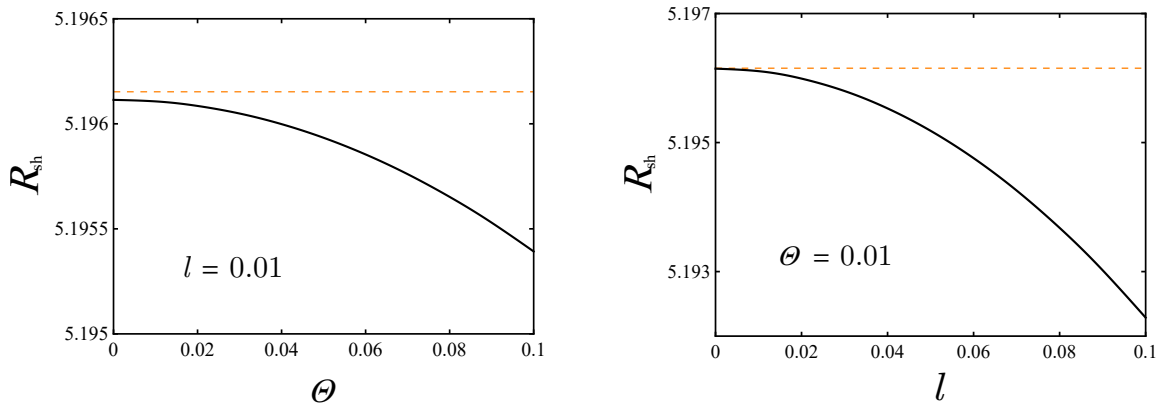


FIG. 26: The left panel shows the shadow radius concerning the Hayward parameter, for $M = 1$, $\Theta = 0.01$. The right panel represents the shadow radius with respect to the NC parameter when $M = 1$ and $l = 0.01$

In the left panel, the plot shows how the shadow radius changes as a function of the Hayward parameter l while keeping the black hole mass fixed at $M = 1$ and setting the NC parameter to $\Theta = 0.01$. The shadow radius decreases as l increases.

The right panel illustrates the variation of the shadow radius concerning the NC parameter while keeping $M = 1$ and fixing the Hayward parameter at $l = 0.01$. The shadow radius decreases as Θ increases. Since Θ represents a fundamental length scale in non-commutative geometry, this result implies that quantum gravitational effects at small scales could cause a more compact black hole shadow than the classical scenario. The decreasing shadow size

could indicate that non-commutativity weakens the overall gravitational lensing effect or alters the effective energy distribution in the black hole spacetime.

If these effects are significant, high-resolution black hole imaging might be able to distinguish non-commutative or regular black holes from classical ones by analyzing their shadow sizes. In the following section, we will explore the constraints on non-commutativity concerning the EHT observations.

B. Lensing observables by EHT

By analyzing the Event Horizon Telescope (EHT) observations of the black hole shadows associated with $SgrA^*$ and $M87^*$ [207–210], we explore potential constraints on the non-commutative parameter Θ within the framework of a Hayward black hole in non-commutative geometry. The angular diameter of the shadow, denoted as θ_{sh} , serves as a critical observable for exploring the modified theories in quantum gravity [211]. Through a comparison of theoretical shadow diameter predictions with the empirical data provided by the EHT, we evaluate whether the observational results impose any limitations on Θ .

For a distant observer situated at a distance D_O from the black hole, the angular diameter θ_{sh} of the black hole shadow is measured as follows [212]

$$\theta_{\text{sh}} = \frac{2b_c}{D_O}, \quad (111)$$

where b_c represents the critical impact parameter.

For the $SgrA^*$ scenario, we adopt the mass and distance values reported by the EHT collaboration: $M = 4 \times 10^6 M_\odot$ and $D_O = 8.15 \text{ kpc}$. The observed angular diameter of the shadow was found to lie within the range $\theta_{\text{sh}} = 48.7 \pm 7 \mu\text{as}$ [209, 210]. In the case of $M87^*$, we assume the mass and distance values as : $M = (6.5 \pm 0.7) \times 10^9 M_\odot$ and $D_O = 16.8 \text{ Mpc}$. The angular diameter of the $M87^*$ black hole shadow was determined to be $\theta_{\text{sh}} = 42 \pm 3 \mu\text{as}$ [207, 208].

Fig. 27 analyzes the black hole angular shadow behavior for $SgrA^*$ and $M87^*$, respectively, within the non-commutative geometry framework. Both plots show the angular shadow diameter as a function of the non-commutative parameter Θ for different values of l/M . In both plots, the angular shadow diameter decreases monotonically with increasing Θ . The shadow radius is slightly sensitive to l/M . For smaller l/M values, the angular shadow

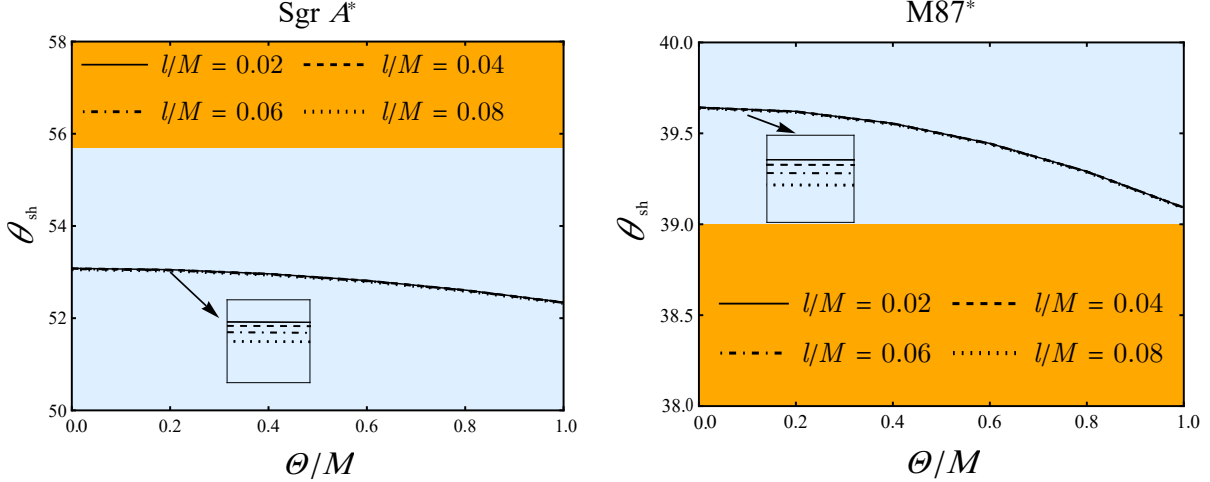


FIG. 27: Angular diameter $\theta_{sh}(\mu as)$ based on M and D_O of $SgrA^*$ and $M87^*$ in relation to NC parameter Θ . The regions of angular shadow that are permitted and excluded based on EHT observations are shown by the orange and blue areas.

diameter is larger, while for larger l/M , it decreases. By considering the Hayward black hole in the non-commutativity framework, the calculated angular diameters fall within the observed range $\theta_{sh} \in (41.5, 55.7)\mu as$ and $\theta_{sh} \in (39, 45)\mu as$ for $SgrA^*$ and $M87^*$, respectively.

IX. GRAVITATIONAL LENSING

This section examines the Gaussian curvature $\mathcal{K}(r, l, \Theta)$, which serves as a key factor in evaluating the stability of the photon sphere. Using this curvature, the deflection angle in gravitational lensing is derived through the Gauss-Bonnet theorem, following the method outlined in Ref. [213]. As demonstrated, the photon spheres analyzed here are inherently unstable, as indicated by $\mathcal{K}(r, l, \Theta) < 0$. Additionally, increasing Θ leads to more pronounced deflection angles, $\hat{\alpha}(b, l, \Theta)$.

A. Stability of the photon sphere

The stability of photon spheres in the vicinity of black holes is largely governed by the geometric and topological characteristics of optical spacetime, where conjugate points play a significant role. When photon trajectories experience perturbations, their response depends on whether the photon sphere is stable or unstable. In the case of instability, slight deviations

lead photons to either be absorbed by the black hole or escape to infinity. Conversely, stable photon spheres enable photons to remain in bounded orbits nearby [214, 215].

The presence or absence of conjugate points within the spacetime manifold plays a crucial role in this behavior. Photon spheres classified as stable contain conjugate points, whereas unstable ones lack them. The Cartan–Hadamard theorem establishes a connection between Gaussian curvature, $\mathcal{K}(r)$, and these points, providing a method for assessing the stability of critical orbits [216]. Following this approach, the null geodesics, which satisfy the condition $ds^2 = 0$, can be expressed as [217, 218]:

$$dt^2 = \gamma_{ij} dx^i dx^j = -\frac{g_{rr}^{(\Theta,l)}(r)}{g_{tt}^{(\Theta,l)}(r)} dr^2 - \frac{\bar{g}_{\varphi\varphi}^{(\Theta,l)}(r)}{g_{tt}^{(\Theta,l)}(r)} d\varphi^2, \quad (112)$$

where i and j range from 1 to 3, γ_{ij} represents the optical metric, and $\bar{g}_{\varphi\varphi}^{(\Theta,l)}(r) \equiv g_{\varphi\varphi}^{(\Theta,l)}(r, \theta = \pi/2)$. Additionally, the Gaussian curvature is given by [216]

$$\mathcal{K}(r, l, \Theta) = \frac{R}{2} = \frac{g_{tt}^{(\Theta,l)}(r)}{\sqrt{g_{rr}^{(\Theta,l)}(r)} \bar{g}_{\varphi\varphi}^{(\Theta,l)}(r)} \frac{\partial}{\partial r} \left[\frac{g_{tt}^{(\Theta,l)}(r)}{2\sqrt{g_{rr}^{(\Theta,l)}(r)} \bar{g}_{\varphi\varphi}^{(\Theta,l)}(r)} \frac{\partial}{\partial r} \left(\frac{\bar{g}_{\varphi\varphi}^{(\Theta,l)}(r)}{g_{tt}^{(\Theta,l)}(r)} \right) \right], \quad (113)$$

where R represents the Ricci scalar in two dimensions. For sufficiently small values of l and Θ , its explicit expression is

$$\begin{aligned} \mathcal{K}(r, l, \Theta) = & \frac{M(3M - 2r)}{r^4} + \frac{8l^2 M^2 (5r - 9M)}{r^7} \\ & + \Theta^2 \left\{ \frac{l^2 M^2 (-23568M^4 + 44220M^3 r - 30775M^2 r^2 + 9379M r^3 - 1050r^4)}{r^{10}(r - 2M)^2} \right. \\ & \left. + \frac{312M^4 - 420M^3 r + 181M^2 r^2 - 24M r^3}{8Mr^7 - 4r^8} \right\}. \end{aligned} \quad (114)$$

As explored in Refs. [214–216], the stability of photon spheres is determined by the sign of $\mathcal{K}(r, l, \Theta)$. A negative curvature, $\mathcal{K}(r, l, \Theta) < 0$, indicates instability, while a positive curvature, $\mathcal{K}(r, l, \Theta) > 0$, corresponds to stability. To illustrate this behavior, Fig. 28 displays the Gaussian curvature $\mathcal{K}(r, l, \Theta)$ as a function of r , highlighting distinct regions associated with stable and unstable photon spheres. The analysis is carried out using the parameter values $M = 0.85$, $l = 0.001$, and $\Theta = 0.01$.

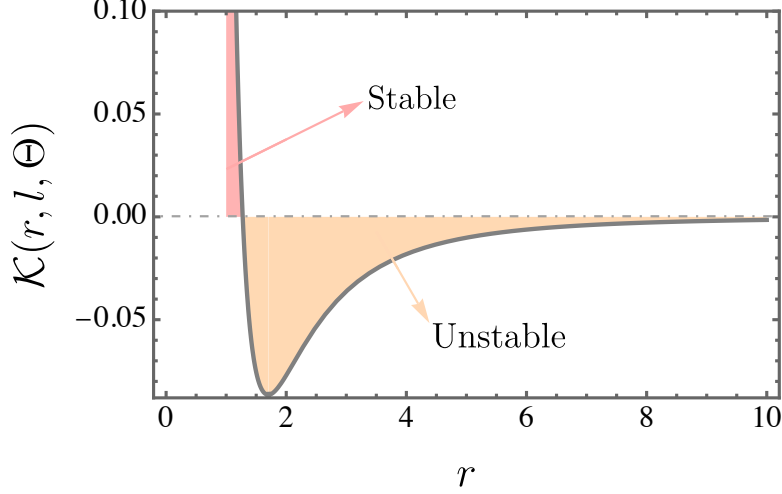


FIG. 28: The Gaussian curvature $\mathcal{K}(r, l, \Theta)$ is presented, with the stable and unstable regions distinctly highlighted. Here, it is considered $M = 0.85$, $l = 0.001$, and $\Theta = 0.01$.

B. The weak deflection limit in the Gauss–Bonnet framework

Building on the Gaussian curvature derived in Eq. (114), the next step is to evaluate the deflection angle in the weak-field limit using the Gauss–Bonnet theorem [213]. To achieve this, the surface area on the equatorial plane is determined and expressed as

$$dS = \sqrt{\gamma} dr d\varphi = \sqrt{\frac{g_{rr}^{(\Theta, l)} g_{\varphi\varphi}^{(\Theta, l)}}{g_{tt}^{(\Theta, l)} g_{tt}^{(\Theta, l)}}} dr d\varphi, \quad (115)$$

allowing the deflection angle to be determined through the following expression:

$$\begin{aligned} \hat{\alpha}(b, l, \Theta) &= - \int \int_D \mathcal{K} dS = - \int_0^\pi \int_{\frac{b}{\sin \varphi}}^\infty \mathcal{K} dS \\ &\simeq \frac{4M}{b} - \frac{15\pi l^2 M^2}{4b^4} + \frac{3\pi M^2}{4b^2} - \frac{8\Theta^2 M}{3b^3} + \frac{875\pi l^2 \Theta^2 M^2}{16b^6} + \frac{75\pi \Theta^2 M^2}{64b^4}. \end{aligned} \quad (116)$$

Fig. 29 illustrates the behavior of the deflection angle $\hat{\alpha}(b, l, \Theta)$. For a given impact parameter, such as $b = 0.2$, an increase in Θ leads to a larger magnitude of $\hat{\alpha}(b, l, \Theta)$. A similar trend is observed when the parameter l is increased, resulting in a greater deflection angle.

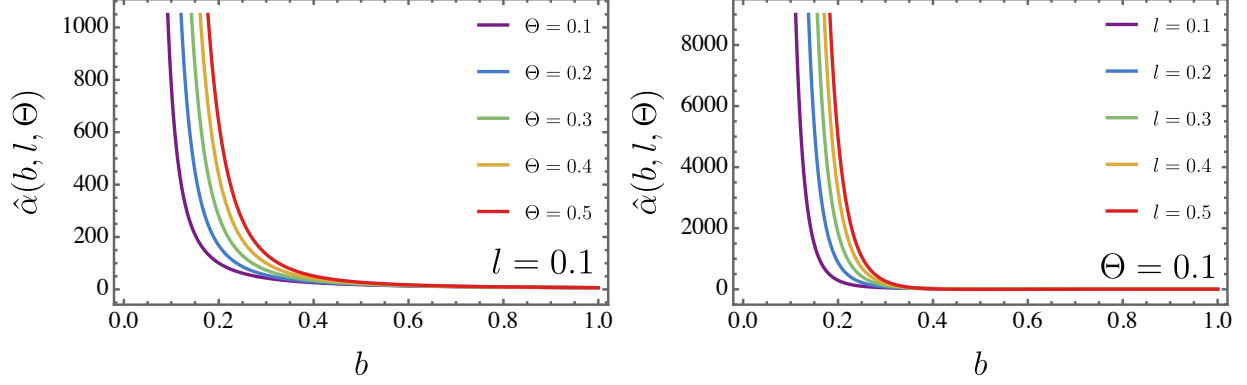


FIG. 29: The deflection angle $\hat{\alpha}(b, l, \Theta)$ is plotted as a function of the impact parameter b for different values of Θ , while maintaining l fixed.

X. ESTIMATION OF BOUNDS BASED ON THE SOLAR SYSTEM TESTS

We revisit the results from Sec. VIII A, now considering a Lagrangian of the form $L(x, \dot{x}) = -\eta/2$, where $\eta = 0$ corresponds to massless particles, while $\eta = 1$ describes massive particles parametrized by the proper time λ . The Lagrangian for motion in the equatorial plane is given by

$$A(r)\dot{t}^2 - B(r)\dot{r}^2 - D(r)\dot{\varphi}^2 = \eta, \quad (117)$$

where we refer to $A(r) \doteq -g_{tt}^{(\Theta, l)}$, $B(r) \doteq g_{rr}^{(\Theta, l)}$, $D(r) \doteq g_{\varphi\varphi}^{(\Theta, l)}$. The above expression, together with the conserved quantities (105), lead to

$$\left[\frac{d}{d\varphi} \left(\frac{1}{r} \right) \right]^2 = r^{-4} D^2(r) \left[\frac{E^2}{A(r)B(r)L^2} - \frac{1}{B(r)L^2} \left(\eta + \frac{L^2}{D(r)} \right) \right]. \quad (118)$$

Defining a new variable as $u = L^2/(Mr)$ and differentiating Eq. (118) with respect to φ ,

we obtain the leading contributions in Θ and l expressed as:

$$\begin{aligned}
\frac{d^2u}{d\varphi^2} &= \eta - u + \frac{3M^2u^2}{L^2} \tag{119} \\
\Theta^2 &\left(l^2 \left(-\frac{3M^{10}u^8(4M^2(137E^2 - 61\eta) + 19L^2)}{L^{10}(L^2 - 2M^2u)^3} - \frac{157M^8(7E^2 - \eta)u^6}{L^6(L^2 - 2M^2u)^3} \right. \right. \\
&+ \frac{6M^6(28E^2 - 3\eta)u^5}{L^4(L^2 - 2M^2u)^3} + \frac{M^2u^7(102L^6M^8(23E^2 - 5\eta) + 8L^8M^6)}{L^{14}(L^2 - 2M^2u)^3} \\
&+ \left. \frac{72M^{16}u^{11}}{L^{14}(L^2 - 2M^2u)^3} - \frac{172M^{14}u^{10}}{L^{12}(L^2 - 2M^2u)^3} + \frac{2M^{12}u^9(75L^2 - 196\eta M^2)}{L^{12}(L^2 - 2M^2u)^3} \right) \\
&- \frac{3E^2L^2M^2u^2}{2(L^2 - 2M^2u)^3} + \frac{M^4(20E^2 + \eta)u^3}{2(L^2 - 2M^2u)^3} - \frac{M^4u^4(4M^2(43E^2 + 6\eta) + 5L^2)}{8L^2(L^2 - 2M^2u)^3} \\
&+ \frac{3M^8(5E^2 + 2\eta)u^5}{L^4(L^2 - 2M^2u)^3} + \frac{21M^6u^5}{4L^2(L^2 - 2M^2u)^3} - \frac{12M^{12}u^8}{L^8(L^2 - 2M^2u)^3} \\
&- \left. \frac{4\eta M^{10}u^6}{L^6(L^2 - 2M^2u)^3} + \frac{23M^{10}u^7}{L^6(L^2 - 2M^2u)^3} - \frac{33M^8u^6}{2L^4(L^2 - 2M^2u)^3} \right) \\
&- \frac{4l^2M^4u^3(2\eta L^2 + 3M^2u^2)}{L^8}.
\end{aligned}$$

The first two terms on the right-hand side represent the Newtonian contribution. The nonlinear term proportional to M^2/L^2 , when expressed in SI units, takes the form $G^2M^2/(c^4L^2)$, which is significantly smaller than the Newtonian terms, introducing a relativistic correction. With this in mind, a perturbative approach is applied to constrain the parameters of the theory. This requires considering perturbations in three parameters: Θ , l , and up to sixth-order in M/L . Under these conditions, Eq. (119) simplifies considerably to

$$\begin{aligned}
u''(\varphi) &= \eta - u + \frac{3M^2u^2(-E^2\Theta^2 + 2L^2)}{2L^4} + \frac{M^4u^3(\Theta^2(\eta + 2E^2) - 16l^2\eta)}{2L^6} \\
&+ u^4 \left(\frac{5E^2\Theta^2M^6}{2L^8} - \frac{5\Theta^2M^4}{8L^6} \right) - \frac{3M^6u^5(8l^2L^2 - \Theta^2L^2)}{2L^{10}}. \tag{120}
\end{aligned}$$

This equation reveals several noteworthy qualitative aspects. First, the non-commutative contribution Θ is coupled to the test particle's energy, a feature widely explored in quantum gravity phenomenology, further reinforced by this model [219, 220]. Second, the Hayward contribution only appears in terms proportional to M^4 , making it less significant than the leading non-commutative correction, which scales with M^2 . Moreover, for massless particles ($\eta = 0$), corrections from the Hayward parameter would only emerge at order M^6/L^{10} , rendering this case less favorable for observational constraints.

A. Perihelion precession of Mercury

A fundamental test of General Relativity involves accurately predicting Mercury's perihelion precession, quantified by angular shifts per century. To examine this, Mercury is treated as a test particle moving in the static spacetime generated by the Sun. Based on the previous discussion, we focus on the massive case with $\eta = 1$. The first correction to GR in Eq. (120), proportional to M^2 , is of the order $E^2 M^2 u^2 \Theta^2 / L^4$. However, for Mercury, this term is significantly smaller than the next-order correction, $M^4 \Theta^2 u^3 / L^6$. This suppression arises because the energy E is relatively small at the large distances considered in this context, as gravitational energy decreases with distance. Consequently, the Θ and l corrections proportional to u^2 , u^4 , and u^5 are negligible and can be disregarded.

By introducing the redefinition $m = M/L$ and denoting ϵ^2 as a general factor multiplying u^3 , the equation takes the form

$$u''(\varphi) = 1 - u + 3m^2 u^2 + \epsilon^2 u^3. \quad (121)$$

The parameter m is treated as a perturbative quantity, introducing the first correction to GR, while the parameter ϵ accounts for modifications arising from non-commutative effects or the Hayward term. Based on this, the solution is expanded in terms of these parameters as $u = u_0 + m^2 u_m + \epsilon^2 u_\epsilon$, where u_0 corresponds to the Newtonian expression given by

$$u_0 = 1 + e \cos(\varphi). \quad (122)$$

Substituting this perturbative expansion into Eq. (121), the resulting expression takes the form

$$m^2 (3(e \cos(\varphi) + 1)^2 - u_m'' - u_m) + \epsilon^2 ((e \cos(\varphi) + 1)^3 - u_\epsilon'' - u_\epsilon) = 0, \quad (123)$$

where terms of order $m^2 \epsilon^2$ have been neglected. The term proportional to m^2 corresponds to the General Relativity correction, given by

$$u_m = 3m^2 \left[\left(1 + \frac{e^2}{2} \right) - \frac{e^2}{6} \cos(2\varphi) + e\varphi \sin(\varphi) \right]. \quad (124)$$

The first term within the square brackets remains constant, while the second term oscillates around zero. Since neither contribute to the perihelion shift, they are omitted from the final expression. The remaining term, being proportional to φ , accumulates over multiple orbits, leading to a measurable effect.

The term proportional to ϵ^2 in Eq. (123) vanishes, introducing new corrections. Its solution contains several trigonometric terms that oscillate around zero, but only one contributes proportionally to φ , given by $\frac{3}{8}e(4+e^2)\varphi\sin(\varphi)$. Incorporating the Newtonian, GR, and new contributions and reinstating the original model parameters, we obtain a useful expression for $u(\varphi)$

$$u(\varphi) = 1 + e \cos(\varphi) + \frac{3M^2}{L^2} \left(1 + \epsilon^2 \frac{(4+e^2)L^2}{8M^2} \right) e\varphi \sin(\varphi). \quad (125)$$

This expression can be further simplified by noting that the terms proportional to $\varphi \sin(\varphi)$ contribute minimally. This observation enables us to combine the last two terms using trigonometric identities, leading to

$$u(\varphi) \approx 1 + e \cos \left[\left(1 - \frac{3M^2}{L^2} \left(1 + \epsilon^2 \frac{(4+e^2)L^2}{8M^2} \right) \right) \varphi \right] \doteq 1 + e \cos \left[\left(1 - \frac{3\widetilde{M}^2}{L^2} \right) \varphi \right]. \quad (126)$$

This can be interpreted as a redefinition of the mass term, expressed as $\widetilde{M}^2 = M^2 [1 + \epsilon^2(4+e^2)L^2/(8M^2)]$, modifying the standard GR result. From this relation, the perihelion shift induced by the new term is given by:

$$\Delta\Phi = 6\pi \frac{\widetilde{M}^2}{L^2} = 6\pi \frac{M^2}{L^2} \left(1 + \epsilon^2 \frac{(4+e^2)L^2}{8M^2} \right). \quad (127)$$

This leads to a dimensionless correction to the General Relativity result, given by $\delta_{\text{Perih}} = \epsilon^2(4+e^2)L^2/(8M^2)$. Since Mercury's orbital period is approximately 88 days, the number of orbits per century is estimated as $100 \times 365.25/88 \approx 415$. By multiplying this by $\Delta\Phi$, the precession per century is obtained. General Relativity predicts a perihelion shift of $\Delta\Phi_{\text{GR}} = 42.9814''/\text{century}$, while the observed value is $\Delta\Phi_{\text{Exp}} = (42.9794 \pm 0.0030)''/\text{century}$ [221, 222]. Using this, experimental constraints can be placed on the parameters Θ and l .

The angular momentum is related to the eccentricity e and the semi-major axis a by $L^2 = Ma(1-e^2)$, while the energy per unit mass is given by $E = -M/(2a)$ [223]. Using natural units, the values for the Sun's mass, Mercury's semi-major axis, and its eccentricity are $M = M_{\odot} = 9.138 \times 10^{37}$, $a = 3.583 \times 10^{45}$, and $e = 0.2056$. This results in an angular momentum of $L = 5.600 \times 10^{41}$, justifying the perturbative treatment due to the presence of terms of the form M^2/L^2 . Additionally, the energy term is approximately $E^2 = 1.627 \times 10^{-16}$, making energy-dependent contributions negligible.

Setting $l = 0$ allows us to constrain Θ , yielding $-1.508 \times 10^{18} \text{ m}^2 \leq \Theta^2 \leq 3.017 \times 10^{17} \text{ m}^2$. Conversely, by taking $\Theta = 0$, the bound on l is found to be $-1.886 \times 10^{16} \text{ m}^2 \leq l^2 \leq$

$8.645 \times 10^{16} \text{ m}^2$. Negative values for the squared parameters are considered for the sake of generality.

B. Deflection of light

When a light ray grazes the surface of a massive object, it gets deflected before reaching the detector. This parallax affects the apparent location of a light emitter in the sky. The deflection of light is carried out by the analysis of null geodesics, which consists in taking $\eta = 0$ in (120). Now, we redefine the function u as simply $1/r$. This gives the following expression

$$u''(\varphi) = -u + \frac{3M(-E^2\Theta^2 + 2L^2)}{2L^2}u^2 + \frac{E^2\Theta^2M^2}{L^2}u^3 - \frac{5M(-4E^2M^2 + L^2)}{8L^2}\Theta^2u^4 - \frac{3M^2(8l^2L^2 - \Theta^2L^2)}{2L^2}u^5. \quad (128)$$

In this case, the factor L/E is the impact parameter b . In order to constrain Θ , it is sufficient to consider the dominant contribution, given by the second term in the right hand side of (128). This way, just as in the previous section, we have a redefinition of the mass parameter as

$$u''(\varphi) + u = 3\widetilde{M}u^2, \quad (129)$$

where $\widetilde{M}^2 = M^2(1 - E^2\Theta^2/(2L^2))$. The Newtonian case consists in taking the left hand side of the above equation as zero. This gives a Newtonian solution [222]

$$u_0 = b^{-1} \sin(\varphi), \quad (130)$$

where b is the impact parameter and the incident angle is $\varphi_0 = 0$, and this solution describes a straight line. Inserting this solution into (129), we have the perturbed solution given by

$$u(\varphi) = \frac{1}{b} \sin(\varphi) + \frac{\widetilde{M}}{b^2} [1 + \cos^2(\varphi)]. \quad (131)$$

The incident and outgoing light ray asymptotically obeys $u \rightarrow 0$ (when $r \rightarrow \infty$). Therefore, by solving the equation $u = 0$, we find the incident and exit angles φ_{in} and φ_{ex} . Considering a perturbation in \widetilde{M}/b (which as we will see is a small quantity), we find $\varphi_{\text{in}} = -2\widetilde{M}/b$ and $\varphi_{\text{ex}} = \pi + 2\widetilde{M}/b$. In these expressions, E and L presented in \widetilde{M} are the energy and

angular momentum of the light ray, which as we discussed in section VIII A, are related to the impact parameter as $b = L/E$. The angle of deflection therefore is $\delta = -2\varphi_{u \rightarrow 0}$

$$\delta_{\Theta} = \frac{4\widetilde{M}}{b} = 4\frac{M}{b} \left(1 - \frac{\Theta^2}{2b^2}\right). \quad (132)$$

For light that grazes the surface of the sun, we have $b \approx R_{\odot} = 4.305 \times 10^{43}$. Besides that, the mass of the sun is $M = M_{\odot} = 9.138 \times 10^{37}$. The dimensionless correction due to the non-commutativity parameter is $1 + \Theta^2/(2b^2)$. Notice that this correction does not depend on the mass of the star directly, but on its impact parameter. Therefore, for a light ray that grazes the surface of a star, it depends only on its radius. This universal behavior is a prediction of this kind of non-commutativity model.

The deflections predicted by GR is $\delta_{\text{GR}} = 4M/b = 1.7516687''$. And the observational value is $\delta_{\text{Exp}} = \frac{1}{2}(1 + \gamma)1.7516687''$, where $\gamma = 0.99992 \pm 0.00012$ [224]. This gives the $-1.936 \times 10^{13} \text{ m}^2 \leq \Theta^2 \leq 9.680 \times 10^{13} \text{ m}^2$. The analysis of the Hayward case requires that we set $\Theta = 0$ in Eq.(128). In this case, the radial equation reads

$$u''(\varphi) = -u + 3Mu^2 - 12M^2l^2u^5. \quad (133)$$

Now we proceed by redefining the quantity $Ml = \alpha$. Using the same technique of the previous subsection, we approximate the solution as $u(\varphi) \approx u_0 + Mu_M + \alpha^2 u_{\alpha}^2$. By substituting this approximation in Eq.(133), we find

$$M \left(\frac{3 \sin^2(\varphi)}{b^2} - u_M - u''_M \right) - \alpha^2 \left(\frac{12 \sin^2(\varphi)}{b^5} + u_{\alpha} + u''_{\alpha} \right) = 0, \quad (134)$$

where we again discarded terms proportional to $\alpha^2 M$. The solution for u_M gives the GR correction $u_M = \frac{M}{b^2} (1 + \cos^2(\varphi))$. The other solution is¹

$$u_{\alpha} = \frac{60\varphi \cos(\varphi) - (47 + 14 \cos(2\varphi) - \cos(4\varphi)) \sin(\varphi)}{b^5}. \quad (135)$$

For small angles φ and considering that in infinity, $u \rightarrow 0$, we find the deflection angle $\delta_l = -2\varphi_{u \rightarrow 0}$ as

$$\delta_l = \frac{4M}{b} \left(1 - \frac{15M^2}{4b^4} l^2\right), \quad (136)$$

which gives the dimensionless correction $15M^2l^2/(4b^4)$. Using the experimental result above, we find $-5.729 \times 10^{23} \text{ m}^2 \leq l^2 \leq 2.863 \times 10^{24} \text{ m}^2$.

¹ We set the initial conditions such that the solution must depend on the impact parameter.

The ratio M^2/b^4 is much smaller than $1/b^2$. In fact, they are 10^{12} orders of magnitude apart. Therefore the Hayward correction is much fainter than the non-commutative one. Also in this case, we considered positive and negative bounds on the quadratic parameters, for the sake of generality.

C. Time delay of light

This measurable effect, known as the Shapiro delay [225], refers to the additional time taken by radar signals to travel from Earth to planets in the solar system and return, accounting for the curvature of spacetime caused by the Sun. To determine this delay, we analyze the null geodesic equation (118). By utilizing the null curve condition alongside the expressions for energy and angular momentum given in (105), the radial coordinate can be expressed as a function of time

$$\left(\frac{dr}{dt}\right)^2 = \frac{A(r)D(r) - \frac{L^2}{E^2}A^2(r)}{B(r)D(r)}. \quad (137)$$

The angular momentum and energy can be rewritten in terms of the closest approach distance b of the light ray to the Sun [226], which is determined by imposing the condition $\dot{r} = 0$. This yields the relation $L^2/E^2 = D(r_{\min})/A(r_{\min})$. Consequently, the time of flight can be expressed as a function of the radial coordinate as follows

$$dt = \pm \frac{1}{A(r)} \frac{1}{\sqrt{\frac{1}{A(r)B(r)} - \frac{D(r_{\min})/A(r_{\min})}{B(r)D(r)}}}. \quad (138)$$

Next, we examine the Hayward and non-commutative cases separately, beginning with the non-commutative scenario by setting $l = 0$. Since our focus is on deviations from the flat spacetime case, we retain only the leading-order corrections in M and Θ^2 . Under this approximation, integrating Eq. (138) yields

$$t = \sqrt{r^2 - r_{\min}^2} + M \left(\sqrt{\frac{r - r_{\min}}{r + r_{\min}}} + 2 \ln \left(\frac{r + \sqrt{r^2 - r_{\min}^2}}{r_{\min}} \right) \right) - \Theta^2 \sqrt{\frac{r - r_{\min}}{r + r_{\min}}} \left(\frac{2M}{r_{\min}^2} + \frac{11M}{8r_{\min}r} \right). \quad (139)$$

For the regime where $r_{\min} \ll r$, the leading contributions from General Relativity and non-commutative corrections are

$$t(r) = r + M + 2M \ln \left(\frac{2r}{r_{\min}} \right) - \frac{2M}{r_{\min}^2} \Theta^2. \quad (140)$$

The travel time from the emitter to the Sun is denoted as $t(r_E)$, while the time from the Sun to the receiver is $t(r_R)$, where $t(r)$ is determined by Eq. (140). Here, r_E and r_R represent the radial coordinates of the emitter and receiver, respectively. The total round-trip time, from emission to reflection at the receiver and back to the emitter, is given by $T = 2t(r_E) + 2t(r_R)$. In this scenario, this results in

$$T_\Theta = 2(r_E + r_R) + 4M \left[1 + \ln \left(\frac{4r_R r_E}{r_{\min}^2} \right) - \frac{\Theta^2}{r_{\min}^2} \right] = T_{\text{flat}} + \delta T. \quad (141)$$

The Shapiro delay is defined as the difference between the time required for the signal to travel in the presence of relativistic corrections, which depend on the mass M , and the corresponding travel time in flat spacetime, given by $T_{\text{flat}} = 2(r_E + r_R)$. In the parametrized post-Newtonian (PPN) framework, this time delay is expressed as

$$\delta T = 4M \left(1 + \frac{1 + \gamma}{2} \ln \left(\frac{4r_R r_E}{r_{\min}^2} \right) \right). \quad (142)$$

Using data from the Cassini probe measurements [227, 228], the most precise constraint on γ is found to be $|\gamma - 1| < 2.3 \times 10^{-5}$. The mean Earth-Sun distance, expressed in natural units, is one astronomical unit (AU), given by $r_E = 1 \text{ AU} = 2.457 \times 10^{45}$. At the time of measurement, the Cassini probe was located at a distance of $r_R = 8.46 \text{ AU}$ from the Sun, while the closest approach of the light signal to the Sun was $r_{\min} = 1.6R_\odot$, where the solar radius is $R_\odot = 4.305 \times 10^{43}$. These values allow us to impose a constraint on Θ , yielding $-1.562 \times 10^{19} \text{ m}^2 \leq \Theta^2 \leq 1.562 \times 10^{19} \text{ m}^2$.

For the Hayward scenario, we set $\Theta = 0$. The dominant contributions obtained from integrating Eq. (138) are

$$\begin{aligned} t = & \sqrt{r^2 - r_{\min}^2} + M \left(\sqrt{\frac{r - r_{\min}}{r + r_{\min}}} + 2 \ln \left(\frac{r + \sqrt{r^2 - r_{\min}^2}}{r_{\min}} \right) \right) \\ & - M^2 \left(\frac{(4r + 5r_{\min})}{2r_{\min}(r + r_{\min})^2} \sqrt{r^2 - r_{\min}^2} - \frac{15 \arctan \left(\frac{r - \sqrt{r^2 - r_{\min}^2}}{r_{\min}} \right)}{r_{\min}} \right) \\ & + l^2 M^2 \left(\frac{10 \arctan \left(\frac{r - \sqrt{r^2 - r_{\min}^2}}{r_{\min}} \right)}{r_{\min}^3} - \frac{3\sqrt{r^2 - r_{\min}^2}}{r_{\min}^2 r^2} \right). \end{aligned} \quad (143)$$

For $b \ll r$, the dominant terms are the following

$$t = r + M + 2M \ln \left(\frac{2r}{r_{\min}} \right) - \frac{2M^2}{r_{\min}} - \frac{3M^2 l^2}{r_{\min}^2 r}. \quad (144)$$

The Shapiro time due to the Hayward contribution is then

$$T_l = 2(r_E + r_R) + 4M \left[1 + \ln \left(\frac{4r_R r_E}{r_{\min}^2} \right) - \frac{3M^2 l^2}{2r_{\min}^2} \left(\frac{1}{r_E} + \frac{1}{r_R} \right) \right]. \quad (145)$$

This effect is weaker compared to the contributions from non-commutative corrections. Using Cassini tracking data once again, the constraints on the Hayward parameter are found to be $-9.437 \times 10^{26} \text{ m}^2 \leq l^2 \leq 1.562 \times 10^{19} \text{ m}^2$, where the solar mass M was used in the calculations. Considering the bounds derived for both Θ and l , negative values for the squared parameters were included for the sake of generality. A summary of all constraints obtained in this section is presented in Tab. IV. Finally, it is important to mention that, although we consider the positive quantity Θ^2 , the negative branch of the bound corresponds to the formal replacement $\Theta^2 \rightarrow -\Theta^2$, which is included here for the sake of generality.

TABLE IV: Bounds for Θ^2 and l^2 derived from Solar System tests.

Solar System Test	Constraints (m ²)
Mercury precession	$-1.508 \times 10^{18} \leq \Theta^2 \leq 3.017 \times 10^{17}$
	$-1.886 \times 10^{16} \leq l^2 \leq 8.645 \times 10^{16}$
Light deflection	$-1.936 \times 10^{13} \leq \Theta^2 \leq 9.680 \times 10^{13}$
	$-5.729 \times 10^{23} \leq l^2 \leq 2.863 \times 10^{24}$
Shapiro time delay	$-1.562 \times 10^{19} \leq \Theta^2 \leq 1.562 \times 10^{19}$
	$-9.437 \times 10^{26} \leq l^2 \leq 1.562 \times 10^{19}$

XI. CONCLUSION

A black hole solution incorporating non-commutative corrections into a Hayward-like metric was proposed in this work. This solution was derived using the non-commutative gauge theory framework, following the approach outlined in Ref. [32].

The analysis began with an investigation of the metric's fundamental properties, including the structure of the event horizon r_h and the Kretschmann scalar \mathcal{K} . The results showed that increasing Θ reduced the event horizon's magnitude. In contrast to the Hayward solution, the modified black hole studied here showed a regular behavior (under the following condition: $\theta \in \mathbb{R} \setminus \{\frac{\pi}{2} + n\pi \mid n \in \mathbb{Z}\}$), as revealed by the analysis of the Kretschmann scalar.

Thermodynamic aspects were then explored by evaluating the Hawking temperature, entropy, and heat capacity. The temperature profile suggested the presence of a remnant mass at the limit $T^{(\Theta,l)} \rightarrow 0$. For a fixed l , increasing Θ raised $T^{(\Theta,l)}$, while the entropy $S^{(\Theta,l)}$ decreased. The heat capacity featured regions of both positive and negative values, indicating transitions between thermodynamic stability and instability.

The emission of quantum radiation was also examined, with a focus on Hawking radiation. The particle creation densities for fermionic, n_ψ , and bosonic, n , modes were determined, allowing a comparison of emission rates. The results indicated that bosons were more abundantly emitted than fermions for a given frequency ω .

A perturbative evaluation of the effective potential allowed us to study the quasinormal modes and the time domain solution in response to scalar perturbations. In essence, it was demonstrated that, by increasing Θ and l , it led to more damped oscillations.

Through the calculation of null geodesics, we could address the photon sphere and black hole shadows. Comparisons with Event Horizon Telescope (EHT) observations enabled constraints on the shadow radii. The stability of critical orbits was assessed via the Gaussian curvature, followed by a gravitational lensing analysis using the Gauss–Bonnet theorem. The deflection angle $\hat{\alpha}(\Theta, l)$ was found to increase with both Θ and l for a fixed impact parameter b , while the critical orbit remained unstable.

Lastly, constraints on the parameters Θ and l were established based on observational tests in the solar system, including Mercury’s perihelion precession, light deflection, and the Shapiro time delay.

As a further perspective, it is worth investigating the absorption cross section and grey-body factors of the black hole analyzed in this manuscript, following the methodology adopted in [229–231]. Moreover, inspired by a recently proposed technique [34], we plan to examine other configurations — such as Bardeen– and Frolov–like black holes (and others) — within the framework of non–commutative gauge theory, along with their corresponding gravitational signatures. These and other ideas are now under development.

Acknowledgments

A. A. Araújo Filho is supported by Conselho Nacional de Desenvolvimento Científico e Tecnológico (CNPq) and Fundação de Apoio à Pesquisa do Estado da Paraíba (FAPESQ),

project No. 150891/2023-7. I. P. L. was partially supported by the National Council for Scientific and Technological Development - CNPq grant 312547/2023-4. I. P. L. would like to acknowledge the contribution of the COST Action BridgeQG (CA23130), supported by COST (European Cooperation in Science and Technology). The authors would like to thank C. Molina for his assistance with the calculations in the time-domain section.

- [1] Charles W Misner, Kip S Thorne, and John Archibald Wheeler. *Gravitation*. Macmillan, 1973.
- [2] Robert M Wald. *General relativity*. University of Chicago press, 2010.
- [3] Nathan Seiberg and Edward Witten. String theory and noncommutative geometry. *Journal of High Energy Physics*, 1999(09):032, 1999.
- [4] Richard J Szabo. Symmetry, gravity and noncommutativity. *Classical and Quantum Gravity*, 23(22):R199, 2006.
- [5] Richard J Szabo. Quantum field theory on noncommutative spaces. *Physics Reports*, 378(4):207–299, 2003.
- [6] Alysson Fábio Ferrari, Horacio Oscar Girotti, Marcelo Gomes, A Yu Petrov, AA Ribeiro, and AJ Da Silva. On the finiteness of noncommutative supersymmetric qed3 in the covariant superfield formulation. *Physics Letters B*, 577(1-2):83–92, 2003.
- [7] Alysson Fábio Ferrari, Horacio Oscar Girotti, Marcelo Gomes, A Yu Petrov, AA Ribeiro, Victor O Rivelles, and AJ Da Silva. Superfield covariant analysis of the divergence structure of noncommutative supersymmetric qed 4. *Physical Review D*, 69(2):025008, 2004.
- [8] Alysson Fábio Ferrari, Horacio Oscar Girotti, Marcelo Gomes, A Yu Petrov, AA Ribeiro, Victor O Rivelles, and AJ da Silva. Towards a consistent noncommutative supersymmetric yang-mills theory: Superfield covariant analysis. *Physical Review D*, 70(8):085012, 2004.
- [9] Ali H Chamseddine. Deforming einstein’s gravity. *Physics Letters B*, 504(1-2):33–37, 2001.
- [10] Y Zhao, Yifu Cai, S Das, G Lambiase, EN Saridakis, and EC Vagenas. Quasinormal modes in noncommutative schwarzschild black holes. *arXiv preprint arXiv:2301.09147*, 2023.
- [11] M. A Anacleto, F. A Brito, J. A. V Campos, and E Passos. Absorption, scattering and shadow by a noncommutative black hole with global monopole. *The European Physical Journal C*, 83(4):298, 2023.

- [12] M. A. Anacleto, F. A. Brito, J. A. V. Campos, and E. Passos. Absorption and scattering of a noncommutative black hole. *Phys. Lett. B*, 803:135334, 2020.
- [13] Narges Heidari, Hassan Hassanabadi, A. A Araújo Filho, and John Kriz. Exploring non-commutativity as a perturbation in the schwarzschild black hole: quasinormal modes, scattering, and shadows. *The European Physical Journal C*, 84(6):566, 2024.
- [14] Masud Chaichian, Anca Tureanu, and G Zet. Corrections to schwarzschild solution in non-commutative gauge theory of gravity. *Physics Letters B*, 660(5):573–578, 2008.
- [15] Robert B Mann and Piero Nicolini. Cosmological production of noncommutative black holes. *Physical Review D*, 84(6):064014, 2011.
- [16] J. A. V Campos, MA Anacleto, F. A Brito, and E Passos. Quasinormal modes and shadow of noncommutative black hole. *Scientific Reports*, 12(1):8516, 2022.
- [17] Marcos A Anacleto, JAV Campos, Francisco A Brito, and E Passos. Quasinormal modes and shadow of a schwarzschild black hole with gup. *Annals of Physics*, 434:168662, 2021.
- [18] G Zet, V Manta, and S Babeti. Desitter gauge theory of gravitation. *International Journal of Modern Physics C*, 14(01):41–48, 2003.
- [19] Majid Karimabadi, S Aliasghar Alavi, and Davood Mahdavian Yekta. Non-commutative effects on gravitational measurements. *Classical and Quantum Gravity*, 37(8):085009, 2020.
- [20] JC Lopez-Dominguez, O Obregon, M Sabido, and C Ramirez. Towards noncommutative quantum black holes. *Physical Review D*, 74(8):084024, 2006.
- [21] Leonardo Modesto and Piero Nicolini. Charged rotating noncommutative black holes. *Physical Review D*, 82(10):104035, 2010.
- [22] Piero Nicolini. Noncommutative black holes, the final appeal to quantum gravity: a review. *International Journal of Modern Physics A*, 24(07):1229–1308, 2009.
- [23] N Heidari, H Hassanabadi, A. A Araújo Filho, J Kriz, S Zare, and P. J Porfírio. Gravitational signatures of a non-commutative stable black hole. *Physics of the Dark Universe*, page 101382, 2023.
- [24] A. A Araújo Filho, S Zare, P. J Porfírio, J Kříž, and H Hassanabadi. Thermodynamics and evaporation of a modified schwarzschild black hole in a non-commutative gauge theory. *Physics Letters B*, 838:137744, 2023.
- [25] Yun Soo Myung, Yong-Wan Kim, and Young-Jai Park. Thermodynamics and evaporation of the noncommutative black hole. *Journal of High Energy Physics*, 2007(02):012, 2007.

- [26] Kourosch Nozari and Behnaz Fazlpour. Thermodynamics of noncommutative schwarzschild black hole. *Modern Physics Letters A*, 22(38):2917–2930, 2007.
- [27] Rabin Banerjee, Bibhas Ranjan Majhi, and Saurav Samanta. Noncommutative black hole thermodynamics. *Physical Review D*, 77(12):124035, 2008.
- [28] Kourosch Nozari and Behnaz Fazlpour. Reissner-nordstr\”{o} m black hole thermodynamics in noncommutative spaces. *arXiv preprint gr-qc/0608077*, 2006.
- [29] M Sharif and Wajiha Javed. Thermodynamics of a bardeen black hole in noncommutative space. *Canadian Journal of Physics*, 89(10):1027–1033, 2011.
- [30] A. A Araújo Filho, J Furtado, JAAS Reis, and J.E.G Silva. Thermodynamical properties of an ideal gas in a traversable wormhole. *Class. Quant. Grav.*, 40(24):245001, 2023.
- [31] J Furtado, H Hassanabadi, JAAS Reis, et al. Thermal analysis of photon-like particles in rainbow gravity. *arXiv preprint arXiv:2305.08587*, 2023.
- [32] Masud Chaichian, Anca Tureanu, and G Zet. Corrections to schwarzschild solution in non-commutative gauge theory of gravity. *Physics Letters B*, 660(5):573–578, 2008.
- [33] Piero Nicolini, Anais Smailagic, and Euro Spallucci. Noncommutative geometry inspired schwarzschild black hole. *Physics Letters B*, 632(4):547–551, 2006.
- [34] Tajron Jurić, A. Naveena Kumara, and Filip Požar. Constructing noncommutative black holes. 3 2025.
- [35] Abdellah Touati and Slimane Zaim. Quantum tunneling from Schwarzschild black hole in non-commutative gauge theory of gravity. *Phys. Lett. B*, 848:138335, 2024.
- [36] Benjamin P Abbott, Richard Abbott, TD Abbott, F Acernese, K Ackley, C Adams, T Adams, P Addresso, Rana X Adhikari, Vaishali B Adya, et al. Gw170814: a three-detector observation of gravitational waves from a binary black hole coalescence. *Phys. Rev. Lett.*, 119(14):141101, 2017.
- [37] Benjamin P Abbott, R Abbott, TD Abbott, MR Abernathy, Fausto Acernese, K Ackley, C Adams, T Adams, Paolo Addresso, RX Adhikari, et al. Gw151226: observation of gravitational waves from a 22-solar-mass binary black hole coalescence. *Phys. Rev. Lett.*, 116(24):241103, 2016.
- [38] B Abbott, S Jawahar, N Lockerbie, and K Tokmakov. Ligo scientific collaboration and virgo collaboration (2016) directly comparing gw150914 with numerical solutions of einstein’s equations for binary black hole coalescence. *Phys. Rev. D*, 94:064035, 2016.

- [39] Suvodip Mukherjee, Benjamin D Wandelt, and Joseph Silk. Probing the theory of gravity with gravitational lensing of gravitational waves and galaxy surveys. *Monthly Notices of the Royal Astronomical Society*, 494(2):1956–1970, 2020.
- [40] O Contigiani. Lensing efficiency for gravitational wave mergers. *Monthly Notices of the Royal Astronomical Society*, 492(3):3359–3363, 2020.
- [41] Charles Galton Darwin. The gravity field of a particle. *Proceedings of the Royal Society of London. Series A. Mathematical and Physical Sciences*, 249(1257):180–194, 1959.
- [42] Robert d’Escourt Atkinson. On light tracks near a very massive star. *Astronomical Journal*, Vol. 70, p. 517, 70:517, 1965.
- [43] Event Horizon Telescope Collaboration et al. First m87 event horizon telescope results. iv. imaging the central supermassive black hole. *arXiv preprint arXiv:1906.11241*, 2019.
- [44] Event Horizon Telescope Collaboration et al. First m87 event horizon telescope results. iv. imaging the central supermassive black hole. *arXiv preprint arXiv:1906.11241*, 2019.
- [45] Frank Eisenhauer, Reinhard Genzel, Tal Alexander, R Abuter, T Paumard, T Ott, A Gilbert, S Gillessen, Matthew Horrobin, Sascha Trippe, et al. Sinfoni in the galactic center: young stars and infrared flares in the central light-month. *The Astrophysical Journal*, 628(1):246, 2005.
- [46] David Ball, Chi-Kwan Chan, Pierre Christian, Buell T Jannuzi, Junhan Kim, Daniel P Marrone, Lia Medeiros, Feryal Ozel, Dimitrios Psaltis, Mel Rose, et al. First m87 event horizon telescope results. vi. the shadow and mass of the central black hole. 2019.
- [47] Kazunori Akiyama, Antxon Alberdi, Walter Alef, Keiichi Asada, Rebecca Azulay, Anne-Kathrin Baczko, David Ball, Mislav Baloković, John Barrett, Dan Bintley, et al. First m87 event horizon telescope results. v. physical origin of the asymmetric ring. *The Astrophysical Journal Letters*, 875(1):L5, 2019.
- [48] Kazunori Akiyama, Antxon Alberdi, Walter Alef, Keiichi Asada, Rebecca Azulay, Anne-Kathrin Baczko, David Ball, Mislav Baloković, John Barrett, Dan Bintley, et al. First m87 event horizon telescope results. ii. array and instrumentation. *The Astrophysical Journal Letters*, 875(1):L2, 2019.
- [49] Kazunori Akiyama, Antxon Alberdi, Walter Alef, Keiichi Asada, Rebecca Azulay, Anne-Kathrin Baczko, David Ball, Mislav Baloković, John Barrett, Dan Bintley, et al. First m87 event horizon telescope results. v. physical origin of the asymmetric ring. *The Astrophysical*

- Journal Letters*, 875(1):L5, 2019.
- [50] Volker Perlick. Theoretical gravitational lensing—beyond the weak-field small-angle approximation. In *The Eleventh Marcel Grossmann Meeting: On Recent Developments in Theoretical and Experimental General Relativity, Gravitation and Relativistic Field Theories (In 3 Volumes)*, pages 680–699. World Scientific, 2008.
- [51] Kumar Shwetketu Virbhadra and George FR Ellis. Schwarzschild black hole lensing. *Phys. Rev. D*, 62(8):084003, 2000.
- [52] Simonetta Frittelli, Thomas P Kling, and Ezra T Newman. Spacetime perspective of schwarzschild lensing. *Phys. Rev. D*, 61(6):064021, 2000.
- [53] Valerio Bozza, Salvatore Capozziello, Gerardo Iovane, and Gaetano Scarpetta. Strong field limit of black hole gravitational lensing. *General Relativity and Gravitation*, 33:1535–1548, 2001.
- [54] Valerio Bozza. Gravitational lensing in the strong field limit. *Phys. Rev. D*, 66(10):103001, 2002.
- [55] Naoki Tsukamoto. Deflection angle in the strong deflection limit in a general asymptotically flat, static, spherically symmetric spacetime. *Phys. Rev. D*, 95(6):064035, 2017.
- [56] R Benton Metcalf, MASSIMO Meneghetti, Camille Avestruz, Fabio Bellagamba, Clécio R Bom, Emmanuel Bertin, Rémi Cabanac, F Courbin, Andrew Davies, Etienne Decencière, et al. The strong gravitational lens finding challenge. *Astronomy & Astrophysics*, 625:A119, 2019.
- [57] Orhan Donmez. Bondi-Hoyle-Lyttleton accretion around the rotating hairy Horndeski black hole. *JCAP*, 09:006, 2024.
- [58] Fahrettin Koyuncu and Orhan Dönmez. Numerical simulation of the disk dynamics around the black hole: Bondi Hoyle accretion. *Mod. Phys. Lett. A*, 29:1450115, 2014.
- [59] KS Virbhadra, D Narasimha, and SM Chitre. Role of the scalar field in gravitational lensing. *arXiv preprint astro-ph/9801174*, 1998.
- [60] Orhan Donmez. Proposing a physical mechanism to explain various observed sources of QPOs by simulating the dynamics of accretion disks around the black holes. *Eur. Phys. J. C*, 84(5):524, 2024.
- [61] Kumar Shwetketu Virbhadra and George FR Ellis. Schwarzschild black hole lensing. *Physical Review D*, 62(8):084003, 2000.

- [62] Orhan Donmez. Perturbing the Stable Accretion Disk in Kerr and 4D Einstein–Gauss–Bonnet Gravities: Comprehensive Analysis of Instabilities and Dynamics. *Res. Astron. Astrophys.*, 24(8):085001, 2024.
- [63] Ali Övgün, İzzet Sakallı, and Joel Saavedra. Shadow cast and Deflection angle of Kerr–Newman–Kasuya spacetime. *JCAP*, 10:041, 2018.
- [64] Gennady S Bisnovatyi-Kogan and Oleg Yu Tsupko. Gravitational lensing in presence of plasma: strong lens systems, black hole lensing and shadow. *Universe*, 3(3):57, 2017.
- [65] Jose María Ezquiaga, Daniel E Holz, Wayne Hu, Macarena Lagos, and Robert M Wald. Phase effects from strong gravitational lensing of gravitational waves. *Physical Review D*, 103(6):064047, 2021.
- [66] Mert Okyay and Ali Övgün. Nonlinear electrodynamics effects on the black hole shadow, deflection angle, quasinormal modes and greybody factors. *JCAP*, 01(01):009, 2022.
- [67] Ali Övgün. Light deflection by Damour–Solodukhin wormholes and Gauss–Bonnet theorem. *Phys. Rev. D*, 98(4):044033, 2018.
- [68] Zonghai Li and Ali Övgün. Finite-distance gravitational deflection of massive particles by a Kerr-like black hole in the bumblebee gravity model. *Phys. Rev. D*, 101(2):024040, 2020.
- [69] Pedro VP Cunha and Carlos AR Herdeiro. Shadows and strong gravitational lensing: a brief review. *General Relativity and Gravitation*, 50:1–27, 2018.
- [70] Reggie C. Pantig and Ali Övgün. Testing dynamical torsion effects on the charged black hole’s shadow, deflection angle and greybody with M87* and Sgr. A* from EHT. *Annals Phys.*, 448:169197, 2023.
- [71] Masamune Oguri. Strong gravitational lensing of explosive transients. *Reports on Progress in Physics*, 82(12):126901, 2019.
- [72] Xiao-Mei Kuang and Ali Övgün. Strong gravitational lensing and shadow constraint from M87* of slowly rotating Kerr-like black hole. *Annals Phys.*, 447:169147, 2022.
- [73] Reggie C. Pantig, Leonardo Mastrototaro, Gaetano Lambiase, and Ali Övgün. Shadow, lensing, quasinormal modes, greybody bounds and neutrino propagation by dyonic ModMax black holes. *Eur. Phys. J. C*, 82(12):1155, 2022.
- [74] Margherita Grespan and Marek Biesiada. Strong gravitational lensing of gravitational waves: A review. *Universe*, 9(5):200, 2023.
- [75] Kumar S Virbhadra and George FR Ellis. Gravitational lensing by naked singularities.

- Physical Review D*, 65(10):103004, 2002.
- [76] Tien Hsieh, Da-Shin Lee, and Chi-Yong Lin. Gravitational time delay effects by kerr and kerr-newman black holes in strong field limits. *Physical Review D*, 104(10):104013, 2021.
- [77] Tien Hsieh, Da-Shin Lee, and Chi-Yong Lin. Strong gravitational lensing by kerr and kerr-newman black holes. *Physical Review D*, 103(10):104063, 2021.
- [78] Amir B Aazami, Charles R Keeton, and AO Petters. Lensing by kerr black holes. ii: Analytical study of quasi-equatorial lensing observables. *J. Math. Phys.*, 52(10), 2011.
- [79] Valerio Bozza, Fabiana De Luca, Gaetano Scarpetta, and M Sereno. Analytic kerr black hole lensing for equatorial observers in the strong deflection limit. *Phys. Rev. D*, 72(8):083003, 2005.
- [80] Valerio Bozza and Gaetano Scarpetta. Strong deflection limit of black hole gravitational lensing with arbitrary source distances. *Phys. Rev. D*, 76(8):083008, 2007.
- [81] Valerio Bozza. Quasiequatorial gravitational lensing by spinning black holes in the strong field limit. *Physical Review D*, 67(10):103006, 2003.
- [82] Samuel E Vazquez and Ernesto P Esteban. Strong field gravitational lensing by a kerr black hole. *arXiv preprint gr-qc/0308023*, 2003.
- [83] Valerio Bozza, Fabiana De Luca, and Gaetano Scarpetta. Kerr black hole lensing for generic observers in the strong deflection limit. *Phys. Rev. D*, 74(6):063001, 2006.
- [84] Kimet Jusufi and Ali Övgün. Gravitational lensing by rotating wormholes. *Physical Review D*, 97(2):024042, 2018.
- [85] Gary W Gibbons and Martin Vyska. The application of weierstrass elliptic functions to schwarzschild null geodesics. *Class. Quant. Grav.*, 29(6):065016, 2012.
- [86] Naoki Tsukamoto, Tomohiro Harada, and Kohji Yajima. Can we distinguish between black holes and wormholes by their einstein-ring systems? *Phys. Rev. D*, 86(10):104062, 2012.
- [87] Ali Övgün, Kimet Jusufi, and İzzet Sakallı. Exact traversable wormhole solution in bumblebee gravity. *Physical Review D*, 99(2):024042, 2019.
- [88] Rajibul Shaikh, Pritam Banerjee, Suvankar Paul, and Tapobrata Sarkar. Strong gravitational lensing by wormholes. *JCAP*, 2019(07):028, 2019.
- [89] Naoki Tsukamoto. Retrolensing by a wormhole at deflection angles π and 3π . *Phys. Rev. D*, 95(8):084021, 2017.
- [90] Naoki Tsukamoto. Strong deflection limit analysis and gravitational lensing of an ellis worm-

- hole. *Phys. Rev. D*, 94(12):124001, 2016.
- [91] Sumanta Chakraborty and Soumitra SenGupta. Strong gravitational lensing—a probe for extra dimensions and kalb-ramond field. *Journal of Cosmology and Astroparticle Physics*, 2017(07):045, 2017.
- [92] Rajibul Shaikh and Sayan Kar. Gravitational lensing by scalar-tensor wormholes and the energy conditions. *Phys. Rev. D*, 96(4):044037, 2017.
- [93] A. A Araújo Filho, J. R Nascimento, A. Yu Petrov, P. J Porfirio, et al. Gravitational lensing by a lorentz-violating black hole. *arXiv preprint arXiv:2404.04176*, 2024.
- [94] Ernesto F Eiroa and Diego F Torres. Strong field limit analysis of gravitational retrolensing. *Phys. Rev. D*, 69(6):063004, 2004.
- [95] Naoki Tsukamoto. Gravitational lensing by using the 0th order of affine perturbation series of the deflection angle of a ray near a photon sphere. *The European Physical Journal C*, 83(4):284, 2023.
- [96] Naoki Tsukamoto, Yungui Gong, et al. Retrolensing by a charged black hole. *Phys. Rev. D*, 95(6):064034, 2017.
- [97] Jing Zhang, Yi Xie, et al. Strong deflection gravitational lensing by the marginally unstable photon spheres of a wormhole. *Physical Review D*, 109(4):043032, 2024.
- [98] Ernesto F Eiroa, Gustavo E Romero, and Diego F Torres. Reissner-nordström black hole lensing. *Physical Review D*, 66(2):024010, 2002.
- [99] KS Virbhadra. Distortions of images of schwarzschild lensing. *Physical Review D*, 106(6):064038, 2022.
- [100] KS Virbhadra. Conservation of distortion of gravitationally lensed images. *Physical Review D*, 109(12):124004, 2024.
- [101] Stephen W Hawking. Black holes and thermodynamics. *Physical Review D*, 13(2):191, 1976.
- [102] Stephen W Hawking. Black hole explosions? *Nature*, 248(5443):30–31, 1974.
- [103] Stephen W Hawking. Particle creation by black holes. *Communications in mathematical physics*, 43(3):199–220, 1975.
- [104] Gary W Gibbons and Stephen W Hawking. Cosmological event horizons, thermodynamics, and particle creation. *Physical Review D*, 15(10):2738, 1977.
- [105] Ali Övgün and Kimet Jusufi. Massive vector particles tunneling from noncommutative charged black holes and their GUP-corrected thermodynamics. *Eur. Phys. J. Plus*,

- 131(5):177, 2016.
- [106] Xiao-Mei Kuang, Bo Liu, and Ali Övgün. Nonlinear electrostatics AdS black hole and related phenomena in the extended thermodynamics. *Eur. Phys. J. C*, 78(10):840, 2018.
- [107] A. Övgün and İ. Sakallı. Hawking Radiation via Gauss-Bonnet Theorem. *Annals Phys.*, 413:168071, 2020.
- [108] Xiao-Mei Kuang, Joel Saavedra, and Ali Övgün. The Effect of the Gauss-Bonnet term to Hawking Radiation from arbitrary dimensional Black Brane. *Eur. Phys. J. C*, 77(9):613, 2017.
- [109] Ali Övgün, İzzet Sakallı, Joel Saavedra, and Carlos Leiva. Shadow cast of noncommutative black holes in Rastall gravity. *Mod. Phys. Lett. A*, 35(20):2050163, 2020.
- [110] Abdul Jawad and Amna Khawer. Thermodynamic consequences of well-known regular black holes under modified first law. *The European Physical Journal C*, 78:1–10, 2018.
- [111] A. A Araújo Filho. Analysis of a regular black hole in verlinde’s gravity. *Classical and Quantum Gravity*, 41(1):015003, 2023.
- [112] Devin Hansen, David Kubizňák, and Robert B Mann. Universality of p- v criticality in horizon thermodynamics. *Journal of High Energy Physics*, 2017(1):1–24, 2017.
- [113] P Sedaghatnia, H Hassanabadi, P. J Porfírio, W. S Chung, et al. Thermodynamical properties of a deformed schwarzschild black hole via dunkl generalization. *arXiv preprint arXiv:2302.11460*, 2023.
- [114] A. A Araújo Filho, Kimet Jusufi, B Cuadros-Melgar, and Genly Leon. Dark matter signatures of black holes with yukawa potential. *Physics of the Dark Universe*, page 101500, 2024.
- [115] Devin Hansen, David Kubizňák, and Robert B Mann. Criticality and surface tension in rotating horizon thermodynamics. *Classical and Quantum Gravity*, 33(16):165005, 2016.
- [116] B Harms and Y Leblanc. Statistical mechanics of black holes. *Physical Review D*, 46(6):2334, 1992.
- [117] Cenalo Vaz. Canonical quantization and the statistical entropy of the schwarzschild black hole. *Physical Review D*, 61(6):064017, 2000.
- [118] A. A Araújo Filho. Implications of a simpson–visser solution in verlinde’s framework. *The European Physical Journal C*, 84(1):1–22, 2024.
- [119] Deyou Chen, Jun Tao, et al. The modified first laws of thermodynamics of anti-de sitter and de sitter space–times. *Nuclear Physics B*, 918:115–128, 2017.

- [120] Per Kraus and Frank Wilczek. Self-interaction correction to black hole radiance. *Nuclear Physics B*, 433(2):403–420, 1995.
- [121] Maulik Parikh. A secret tunnel through the horizon. *International Journal of Modern Physics D*, 13(10):2351–2354, 2004.
- [122] Maulik K Parikh. Energy conservation and hawking radiation. *arXiv preprint hep-th/0402166*, 2004.
- [123] Maulik K Parikh and Frank Wilczek. Hawking radiation as tunneling. *Physical review letters*, 85(24):5042, 2000.
- [124] Jingyi Zhang and Zheng Zhao. New coordinates for kerr–newman black hole radiation. *Physics Letters B*, 618(1-4):14–22, 2005.
- [125] David Senjaya. The bocharova–bronnikov–melnikov–bekenstein black hole’s exact quasi-bound states and hawking radiation. *The European Physical Journal C*, 84(6):607, 2024.
- [126] MA Anacleto, FA Brito, and E Passos. Quantum-corrected self-dual black hole entropy in tunneling formalism with gup. *Physics Letters B*, 749:181–186, 2015.
- [127] Xavier Calmet, Stephen DH Hsu, and Marco Sebastianutti. Quantum gravitational corrections to particle creation by black holes. *Physics Letters B*, 841:137820, 2023.
- [128] Cecilia Giavoni and Marc Schneider. Quantum effects across dynamical horizons. *Classical and Quantum Gravity*, 37(21):215020, 2020.
- [129] Stephen W Hawking. Particle creation by black holes. In *Euclidean quantum gravity*, pages 167–188. World Scientific, 1975.
- [130] George Johnson and John March-Russell. Hawking radiation of extended objects. *Journal of High Energy Physics*, 2020(4):1–16, 2020.
- [131] Stefan Hollands and Robert M Wald. Quantum fields in curved spacetime. *Physics Reports*, 574:1–35, 2015.
- [132] CAS Silva and FA Brito. Quantum tunneling radiation from self-dual black holes. *Physics Letters B*, 725(4-5):456–462, 2013.
- [133] FS Mirekhtiary, A Abbasi, K Hosseini, and F Tulucu. Tunneling of rotational black string with nonlinear electromagnetic fields. *Physica Scripta*, 99(3):035005, 2024.
- [134] AJM Medved. Radiation via tunneling from a de sitter cosmological horizon. *Physical Review D*, 66(12):124009, 2002.
- [135] Luciano Vanzo, Giovanni Acquaviva, and Roberto Di Criscienzo. Tunnelling methods

- and hawking's radiation: achievements and prospects. *Classical and Quantum Gravity*, 28(18):183001, 2011.
- [136] Francesco Del Porro, Stefano Liberati, and Marc Schneider. Tunneling method for hawking quanta in analogue gravity. *arXiv preprint arXiv:2406.14603*, 2024.
- [137] Abdellah Touati and Zaim Slimane. Quantum tunneling from schwarzschild black hole in non-commutative gauge theory of gravity. *Physics Letters B*, 848:138335, 2024.
- [138] P Mitra. Hawking temperature from tunnelling formalism. *Physics Letters B*, 648(2-3):240–242, 2007.
- [139] EPJ van den Heuvel. Compact stars and the evolution of binary systems. In *Fluid Flows To Black Holes: A Tribute to S Chandrasekhar on His Birth Centenary*, pages 55–73. World Scientific, 2011.
- [140] WA Dziembowski and Philip R Goode. Effects of differential rotation on stellar oscillations—a second-order theory. *The Astrophysical Journal*, 394:670–687, 1992.
- [141] Frans Pretorius. Evolution of binary black-hole spacetimes. *Physical review letters*, 95(12):121101, 2005.
- [142] Wasaburo Unno, Yoji Osaki, Hiroyasu Ando, and Hiormoto Shibahashi. Nonradial oscillations of stars. *Tokyo: University of Tokyo Press*, 1979.
- [143] Hans Kjeldsen and Timothy R Bedding. Amplitudes of stellar oscillations: the implications for asteroseismology. *arXiv preprint astro-ph/9403015*, 1994.
- [144] Jarrod R Hurley, Christopher A Tout, and Onno R Pols. Evolution of binary stars and the effect of tides on binary populations. *Monthly Notices of the Royal Astronomical Society*, 329(4):897–928, 2002.
- [145] Kadri Yakut and Peter P Eggleton. Evolution of close binary systems. *The Astrophysical Journal*, 629(2):1055, 2005.
- [146] B. Hamil and B. C. Lütfüoğlu. Noncommutative Schwarzschild black hole surrounded by quintessence: Thermodynamics, Shadows and Quasinormal modes. *Phys. Dark Univ.*, 44:101484, 2024.
- [147] Jose Luis Blázquez-Salcedo, Xiao Yan Chew, and Jutta Kunz. Scalar and axial quasinormal modes of massive static phantom wormholes. *Physical Review D*, 98(4):044035, 2018.
- [148] R Oliveira, DM Dantas, Victor Santos, and CAS Almeida. Quasinormal modes of bumblebee wormhole. *Classical and Quantum Gravity*, 36(10):105013, 2019.

- [149] RA Konoplya and Alexander Zhidenko. Quasinormal modes of black holes: From astrophysics to string theory. *Reviews of Modern Physics*, 83(3):793, 2011.
- [150] A. A. Araújo Filho, N. Heidari, J. A. A. S. Reis, and H. Hassanabadi. The impact of an antisymmetric tensor on charged black holes: evaporation process, geodesics, deflection angle, scattering effects and quasinormal modes. *Class. Quant. Grav.*, 42(6):065026, 2025.
- [151] Poulami Dutta Roy, S Aneesh, and Sayan Kar. Revisiting a family of wormholes: geometry, matter, scalar quasinormal modes and echoes. *The European Physical Journal C*, 80(9):1–17, 2020.
- [152] Emanuele Berti, Vitor Cardoso, Mark Ho-Yeuk Cheung, Francesco Di Filippo, Francisco Duque, Paul Martens, and Shinji Mukohyama. Stability of the fundamental quasinormal mode in time-domain observations against small perturbations. *Phys. Rev. D*, 106(8):084011, 2022.
- [153] Gary T Horowitz and Veronika E Hubeny. Quasinormal modes of ads black holes and the approach to thermal equilibrium. *Physical Review D*, 62(2):024027, 2000.
- [154] Lionel London, Deirdre Shoemaker, and James Healy. Modeling ringdown: Beyond the fundamental quasinormal modes. *Physical Review D*, 90(12):124032, 2014.
- [155] Antonino Flachi and José PS Lemos. Quasinormal modes of regular black holes. *Physical Review D*, 87(2):024034, 2013.
- [156] Kostas D Kokkotas and Bernd G Schmidt. Quasi-normal modes of stars and black holes. *Living Reviews in Relativity*, 2(1):1–72, 1999.
- [157] Ángel Rincón and Victor Santos. Greybody factor and quasinormal modes of regular black holes. *The European Physical Journal C*, 80(10):1–7, 2020.
- [158] Hans-Peter Nollert. Quasinormal modes: the characteristicsound’of black holes and neutron stars. *Classical and Quantum Gravity*, 16(12):R159, 1999.
- [159] Valeria Ferrari and Bahram Mashhoon. New approach to the quasinormal modes of a black hole. *Physical Review D*, 30(2):295, 1984.
- [160] Adailton Azevedo Araújo Filho, Kimet Jusufi, Bertha Cuadros-Melgar, Genly Leon, Abdul Jawad, and C. E Pellicer. Charged black holes with yukawa potential. *Physics of the Dark Universe*, 46:101711, 2024.
- [161] Victor Santos, R. V Maluf, and C. A. S Almeida. Quasinormal frequencies of self-dual black holes. *Physical Review D*, 93(8):084047, 2016.

- [162] Ali Övgün, Izzet Sakallı, and Joel Saavedra. Quasinormal modes of a schwarzschild black hole immersed in an electromagnetic universe. *Chinese Physics C*, 42(10):105102, 2018.
- [163] Michele Maggiore. Physical interpretation of the spectrum of black hole quasinormal modes. *Physical Review Letters*, 100(14):141301, 2008.
- [164] Emanuele Berti, Vitor Cardoso, and Andrei O Starinets. Quasinormal modes of black holes and black branes. *Classical and Quantum Gravity*, 26(16):163001, 2009.
- [165] Friedrich W Hehl, Paul Von der Heyde, G David Kerlick, and James M Nester. General relativity with spin and torsion: Foundations and prospects. *Reviews of Modern Physics*, 48(3):393, 1976.
- [166] Ali H Chamseddine. Deforming einstein’s gravity. *Physics Letters B*, 504(1-2):33–37, 2001.
- [167] Branislav Jurco, Stefan Schraml, Peter Schupp, and Julius Wess. Enveloping algebra-valued gauge transformations for non-abelian gauge groups on non-commutative spaces. *The European Physical Journal C-Particles and Fields*, 17(3):521–526, 2000.
- [168] A. A. Araújo Filho. Implications of a Simpson–Visser solution in Verlinde’s framework. *Eur. Phys. J. C*, 84(1):73, 2024.
- [169] A. A. Araújo Filho. Analysis of a regular black hole in Verlinde’s gravity. *Class. Quant. Grav.*, 41(1):015003, 2024.
- [170] Marco Angheben, Mario Nadalini, Luciano Vanzo, and Sergio Zerbini. Hawking radiation as tunneling for extremal and rotating black holes. *Journal of High Energy Physics*, 2005(05):014, 2005.
- [171] Ryan Kerner and Robert B Mann. Tunnelling, temperature, and taub-nut black holes. *Physical Review D*, 73(10):104010, 2006.
- [172] Ryan Kerner and Robert B Mann. Fermions tunnelling from black holes. *Classical and Quantum Gravity*, 25(9):095014, 2008.
- [173] Ryan Kerner and Robert B Mann. Fermions tunnelling from black holes. *Classical and Quantum Gravity*, 25(9):095014, 2008.
- [174] Mudassar Rehman and K Saifullah. Charged fermions tunneling from accelerating and rotating black holes. *Journal of Cosmology and Astroparticle Physics*, 2011(03):001, 2011.
- [175] Hui-Ling Li, Shu-Zheng Yang, Teng-Jiao Zhou, and Rong Lin. Fermion tunneling from a vaidya black hole. *Europhysics Letters*, 84(2):20003, 2008.
- [176] Roberto Di Criscienzo and Luciano Vanzo. Fermion tunneling from dynamical horizons.

- Europhysics Letters*, 82(6):60001, 2008.
- [177] Alexandre Yale and Robert B Mann. Gravitinos tunneling from black holes. *Physics Letters B*, 673(2):168–172, 2009.
- [178] Ryan Kerner and Robert B Mann. Charged fermions tunnelling from kerr–newman black holes. *Physics letters B*, 665(4):277–283, 2008.
- [179] Alexandre Yale. Exact hawking radiation of scalars, fermions, and bosons using the tunneling method without back-reaction. *Physics Letters B*, 697(4):398–403, 2011.
- [180] Alexandre Yale. There are no quantum corrections to the hawking temperature via tunneling from a fixed background. *The European Physical Journal C*, 71:1–4, 2011.
- [181] Bhramar Chatterjee and P Mitra. Hawking temperature and higher order calculations. *Physics Letters B*, 675(2):240–242, 2009.
- [182] Andrea Barducci, Roberto Casalbuoni, and L Lusanna. Supersymmetries and the pseudo-classical relativistic electron. *Nuovo Cimento. A*, 35(3):377–399, 1976.
- [183] Guido Cognola, Luciano Vanzo, Sergio Zerbini, and R Soldati. On the lagrangian formulation of a charged spinning particle in an external electromagnetic field. *Physics Letters B*, 104(1):67–69, 1981.
- [184] Sunny Vagnozzi, Rittick Roy, Yu-Dai Tsai, Luca Visinelli, Misba Afrin, Alireza Allahyari, Parth Bambhaniya, Dipanjan Dey, Sushant G Ghosh, Pankaj S Joshi, et al. Horizon-scale tests of gravity theories and fundamental physics from the event horizon telescope image of sagittarius a. *Classical and Quantum Gravity*, 2022.
- [185] G Zet, V Manta, and S Babeti. Desitter gauge theory of gravitation. *International Journal of Modern Physics C*, 14(01):41–48, 2003.
- [186] Che-Yu Chen, Hsu-Wen Chiang, and Jie-Shiun Tsao. Eikonal quasinormal modes and photon orbits of deformed schwarzschild black holes. *Physical Review D*, 106(4):044068, 2022.
- [187] Edward W Leaver. Solutions to a generalized spheroidal wave equation: Teukolsky’s equations in general relativity, and the two-center problem in molecular quantum mechanics. *Journal of mathematical physics*, 27(5):1238–1265, 1986.
- [188] Hans-Joachim Blome and Bahram Mashhoon. Quasi-normal oscillations of a schwarzschild black hole. *Physics Letters A*, 100(5):231–234, 1984.
- [189] Vitor Cardoso and Jose PS Lemos. Quasinormal modes of schwarzschild–anti-de sitter black holes: Electromagnetic and gravitational perturbations. *Physical Review D*, 64(8):084017,

- 2001.
- [190] N Heidari and H Hassanabadi. Investigation of the quasinormal modes of a schwarzschild black hole by a new generalized approach. *Physics Letters B*, 839:137814, 2023.
 - [191] Carsten Gundlach, Richard H. Price, and Jorge Pullin. Late time behavior of stellar collapse and explosions: 1. Linearized perturbations. *Phys. Rev. D*, 49:883–889, 1994.
 - [192] Anshuman Baruah, Ali Övgün, and Atri Deshamukhya. Quasinormal modes and bounding greybody factors of GUP-corrected black holes in Kalb–Ramond gravity. *Annals Phys.*, 455:169393, 2023.
 - [193] S. V. Bolokhov. Late time decay of scalar and Dirac fields around an asymptotically de Sitter black hole in the Euler–Heisenberg electrodynamics. *Eur. Phys. J. C*, 84(6):634, 2024.
 - [194] Wen-Di Guo, Qin Tan, and Yu-Xiao Liu. Quasinormal modes and greybody factor of a Lorentz-violating black hole. *JCAP*, 07:008, 2024.
 - [195] Zhen-Hao Yang, Cheng Xu, Xiao-Mei Kuang, Bin Wang, and Rui-Hong Yue. Echoes of massless scalar field induced from hairy Schwarzschild black hole. *Phys. Lett. B*, 853:138688, 2024.
 - [196] Milena Skvortsova. Ringing of Extreme Regular Black Holes. *Grav. Cosmol.*, 30(3):279–288, 2024.
 - [197] Cai-Ying Shao, Cong Zhang, Wei Zhang, and Cheng-Gang Shao. Scalar fields around a loop quantum gravity black hole in de Sitter spacetime: Quasinormal modes, late-time tails and strong cosmic censorship. *Phys. Rev. D*, 109(6):064012, 2024.
 - [198] Xiao-Xiong Zeng, Guo-Ping Li, and Ke-Jian He. The shadows and observational appearance of a noncommutative black hole surrounded by various profiles of accretions. *Nuclear Physics B*, 974:115639, 2022.
 - [199] Bilel Hamil and BC Lütfüoğlu. Thermodynamics and shadows of quantum-corrected reissner–nordström black hole surrounded by quintessence. *Physics of the Dark Universe*, 42:101293, 2023.
 - [200] Zening Yan, Xiaoji Zhang, Maoyuan Wan, and Chen Wu. Shadows and quasinormal modes of a charged non-commutative black hole by different methods. *The European Physical Journal Plus*, 138(5):1–14, 2023.
 - [201] David Ball, Chi-kwan Chan, Pierre Christian, Buell T Jannuzi, Junhan Kim, Daniel P Marrone, Lia Medeiros, Feryal Ozel, Dimitrios Psaltis, Mel Rose, et al. First m87 event

- horizon telescope results. i. the shadow of the supermassive black hole. *The Astrophysical Journal Letters*, 2019.
- [202] Samuel E Gralla. Can the eht m87 results be used to test general relativity. *Physical Review D*, 103(2):024023, 2021.
- [203] Kazunori Akiyama, Antxon Alberdi, Walter Alef, Keiichi Asada, Rebecca Azulay, Anne-Kathrin Baczko, David Ball, Mislav Baloković, John Barrett, Dan Bintley, et al. First m87 event horizon telescope results. v. physical origin of the asymmetric ring. *The Astrophysical Journal Letters*, 875(1):L5, 2019.
- [204] Volker Perlick, Oleg Yu Tsupko, and Gennady S Bisnovatyi-Kogan. Influence of a plasma on the shadow of a spherically symmetric black hole. *Physical Review D*, 92(10):104031, 2015.
- [205] RA Konoplya. Shadow of a black hole surrounded by dark matter. *Physics Letters B*, 795:1–6, 2019.
- [206] Abdellah Touati and Slimane Zaim. Geodesic equation in non-commutative gauge theory of gravity. *Chinese Physics C*, 46(10):105101, 2022.
- [207] K Akiyama, A Alberdi, W Alef, K Asada, R Azulay, AK Baczko, D Ball, M Baloković, J Barrett, Event Horizon Telescope Collaboration, et al. First m87 event horizon telescope results. i. the shadow of the supermassive black hole. *The Astrophysical Journal Letters*, 875, 2019.
- [208] Kazunori Akiyama, Antxon Alberdi, Walter Alef, Keiichi Asada, Rebecca Azulay, Anne-Kathrin Baczko, David Ball, Mislav Baloković, John Barrett, Dan Bintley, et al. First m87 event horizon telescope results. vi. the shadow and mass of the central black hole. *The Astrophysical Journal Letters*, 875(1):L6, 2019.
- [209] Kazunori Akiyama, Antxon Alberdi, Walter Alef, Juan Carlos Algaba, Richard Anantua, Keiichi Asada, Rebecca Azulay, Uwe Bach, Anne-Kathrin Baczko, David Ball, et al. First sagittarius a* event horizon telescope results. iv. variability, morphology, and black hole mass. *The Astrophysical Journal Letters*, 930(2):L15, 2022.
- [210] Kazunori Akiyama, Antxon Alberdi, Walter Alef, Juan Carlos Algaba, Richard Anantua, Keiichi Asada, Rebecca Azulay, Uwe Bach, Anne-Kathrin Baczko, David Ball, et al. First sagittarius a* event horizon telescope results. vi. testing the black hole metric. *The Astrophysical Journal Letters*, 930(2):L17, 2022.
- [211] Misba Afrin, Sunny Vagnozzi, and Sushant G Ghosh. Tests of loop quantum gravity from

- the event horizon telescope results of sgr a. *The Astrophysical Journal*, 944(2):149, 2023.
- [212] Rahul Kumar and Sushant G Ghosh. Rotating black holes in 4d einstein-gauss-bonnet gravity and its shadow. *Journal of Cosmology and Astroparticle Physics*, 2020(07):053, 2020.
- [213] G. W. Gibbons and M. C. Werner. Applications of the Gauss-Bonnet theorem to gravitational lensing. *Class. Quant. Grav.*, 25:235009, 2008.
- [214] Chen-Kai Qiao. Curvatures, photon spheres, and black hole shadows. *Physical Review D*, 106(8):084060, 2022.
- [215] Chen-Kai Qiao and Ming Li. Geometric approach to circular photon orbits and black hole shadows. *Physical Review D*, 106(2):L021501, 2022.
- [216] Chen-Kai Qiao. The existence and distribution of photon spheres near spherically symmetric black holes—a geometric analysis. *arXiv preprint arXiv:2407.14035*, 2024.
- [217] A. A Araújo Filho, J. R Nascimento, A. Yu Petrov, P. J Porfírio, and Ali Övgün. Effects of non-commutative geometry on black hole properties. *Physics of the Dark Universe*, 46:101630, 2024.
- [218] N. Heidari, A. A. Araújo Filho, R. C. Pantig, and A. Övgün. Absorption, scattering, geodesics, shadows and lensing phenomena of black holes in effective quantum gravity. *Phys. Dark Univ.*, 47:101815, 2025.
- [219] A. Addazi et al. Quantum gravity phenomenology at the dawn of the multi-messenger era—A review. *Prog. Part. Nucl. Phys.*, 125:103948, 2022.
- [220] R. Alves Batista et al. White paper and roadmap for quantum gravity phenomenology in the multi-messenger era. *Class. Quant. Grav.*, 42(3):032001, 2025.
- [221] R. Casana, A. Cavalcante, F. P. Poulis, and E. B. Santos. Exact Schwarzschild-like solution in a bumblebee gravity model. *Phys. Rev. D*, 97(10):104001, 2018.
- [222] Ke Yang, Yue-Zhe Chen, Zheng-Qiao Duan, and Ju-Ying Zhao. Static and spherically symmetric black holes in gravity with a background Kalb-Ramond field. *Phys. Rev. D*, 108(12):124004, 2023.
- [223] Herbert Goldstein, Charles Poole, and John Safko. *Classical Mechanics*. Addison-Wesley, San Francisco, USA, 3rd edition, 2002.
- [224] SB Lambert and Chr Le Poncin-Lafitte. Improved determination of γ by vlbi. *Astronomy & Astrophysics*, 529:A70, 2011.
- [225] Irwin I. Shapiro. Fourth Test of General Relativity. *Phys. Rev. Lett.*, 13:789–791, 1964.

- [226] Rui-Bo Wang, Shi-Jie Ma, Jian-Bo Deng, and Xian-Ru Hu. Estimating the strength of Lorentzian distribution in non-commutative geometry by solar system tests. 11 2024.
- [227] B. Bertotti, L. Iess, and P. Tortora. A test of general relativity using radio links with the Cassini spacecraft. *Nature*, 425:374–376, 2003.
- [228] Clifford M. Will. The Confrontation between General Relativity and Experiment. *Living Rev. Rel.*, 17:4, 2014.
- [229] A. A Araújo Filho. Particle production induced by a lorentzian non-commutative spacetime. *arXiv preprint arXiv:2502.19366*, 2025.
- [230] A. A Araújo Filho. Particle creation and evaporation in kalb-ramond gravity. *arXiv e-prints*, pages arXiv–2411, 2024.
- [231] A. A Araújo Filho. How does non-metricity affect particle creation and evaporation in bumblebee gravity? *arXiv e-prints*, pages arXiv–2501, 2025.